A combined experimental and computational study of AuPd nanoparticles

by

Alina Bruma

A thesis submitted to
The University of Birmingham
for the degree of
DOCTOR OF PHILOSOPHY

Nanoscale Physics Research Laboratory

School of Physics and Astronomy

University of Birmingham

July 2013

UNIVERSITY OF
BIRMINGHAM

University of Birmingham Research Archive

e-theses repository

This unpublished thesis/dissertation is copyright of the author and/or third parties. The intellectual property rights of the author or third parties in respect of this work are as defined by The Copyright Designs and Patents Act 1988 or as modified by any successor legislation.

Any use made of information contained in this thesis/dissertation must be in accordance with that legislation and must be properly acknowledged. Further distribution or reproduction in any format is prohibited without the permission of the copyright holder.

Abstract

The research presented in this thesis is focused on the investigation of structural properties of bimetallic gold-palladium (AuPd) nanoparticles via hybrid theoretical and experimental microscopy study. The *first system* that has been studied theoretically is the 98-atom AuPd nanoclusters, an analysis purely theoretical that had the purpose of studying energetics and segregation effects of AuPd nanoparticles up to 100 atoms and to assess how typical is the Leary tetrahedron for this system. We have found that, after the optimization of the chemical ordering, although this motif is the most stable at the empirical level, it tends to lose its stability at the DFT calculations level, against other motifs such as FCC or Marks Decahedra. The *second system* that has been studied is the $Au_{24}Pd_1$ nanoclusters. For this case we have employed a hybrid theoretical and experimental approach. Theoretically, by performing a direct search at the DFT level using Basin Hopping Monte Carlo, we have been able to identify, as putative global minima, pyramidal cage structures, where the Pd dopant is located in the core, surrounded by a Au. The Löwdin populatin analysis has emphasized a degree of charge transfer from Pd to Au, which may explain the enhanced catalytic activity of this system with respect to the Au_{25} clusters. Experimentally, STEM has been employed for the morphological characterization of $Au_{24}Pd_1$ clusters supported on Multiwall Carbon Nanotubes, and, whenever possible, we have tried to link the morphological experimental analysis with the theoretical findings. Finally, for the *third system*, we have aimed to study the effect of annealing on the evaporated AuPd nanoparticles and identified that, not only $L1_2$ ordered crystallographic phases could be obtained, but also various morphologies of nanoparticles, ranging from mixed to layered and core-shell. This study aimed to bring an insight on the segregation and energetics effects of AuPd nanoparticles.

Acknowledgments

I would like to thank Professor Richard Palmer for giving me the opportunity to work in his laboratory. I would like to thank my supervisor, Dr Ziyou Li for her invaluable guidance and enthusiasm, as well as for the support and help given throughout my PhD. I would also like to thank Professor Roy Johnston for the guidance regarding the development of the theoretical and experimental sections in my thesis, as well as for his support, patience and encouragements. Acknowledgments also for the theoretical group in CNR-IPCF Pisa, Italy, especially to Professor Alessandro Fortunelli for giving me the opportunity to visit his laboratory and develop calculations using the supercomputer facilities in Pisa. Special thanks go to Dr Quanmin Guo for allowing me to use the evaporation system. Acknowledgments go to Dr Giovanni Barcaro and Fabio Negreiros (CNR-IPCF, Pisa, Italy) for their help, friendship and the valuable discussions and advices during my visit to Pisa. Acknowledgments also go to present and past members of the Johnston Group: Ramli Ismail, Paul West, Paul Jennings, Chris Heard, Ivailo Atanasov and Palmer Group: Ivi Xie, Lin Tang, Tianluo Pan.

I acknowledge support from Engineering and Science Research Council (EPSRC) and COST Action STSM MP0903-230712-021238. I would also like to acknowledge *cpu* time from different sources: University of Birmingham BlueBEAR supercomputer facitility, University of Warwick MidPlus Regional Centre of Excellence for Computational Science, Engineering and Mathematics and CINECA Supercomputer Centre (Bologna, Italy).

Finally, I would like to thank my family for always believing in me and for their constant love and support throughout the PhD years spent in Birmingham.

List of figures

1.1. Schematic representation (cross section) of various compositions that can be obtained for bimetallic nanoparticles: (a) core-shell; (b) Janus nanoparticles and phase separated bimetallic nanoparticles; (c) ordered alloy and random mixture alloy; (d) onion-like bimetallic nanoparticles. Taken from Ref. [10]........ 5

1.2. A schematic representation of the presence of homotops for $Ag_{11}Ni_{27}$ nanoclustes. For the same size and composition, the spatial arrangement of atoms is different. The nanoparticles on top and middle rows are two isomers for $Ag_{11}Ni_{27}$ whereas the nanoparticles on top and bottom rows are homotops of the same cluster. Taken from Ref. [28]........ 7

1.3. A magnetron sputtering gas aggregation cluster beam source. The setup consists in: (a) magnetron gun with a target; (b) adjustable nozzle; (c) electrostatic skimmers; (d) high voltage lens; (e) Einzel lens for controlling the kinetic energy of the cluster; (f) deflection plates for the spatial control of the cluster beam; (g)-(h) Einzel lenses. All the different chambers of the cluster beam are differentially pumped. Inset: Formation of ionized clusters in Ar plasma by gas condensation. Taken from Ref. [37]........ 10

1.4. The plot of the potential energy vs. the position (x) along the surface during the surface diffusion process. Adapted from Ref. [47]........ 13

1.5. (a) Volmer-Weber; (b) Stransky-Krastanov; (c) Frank-van-der-Merwe growth modes. After Ref. [47]........ 14

1.6. A Scanning Transmission Electron Microscope image of the evolution of Au-rich and Pd-rich nanoparticles on the surface of amorphous carbon (left) and the effect of nanoparticles sintering under the electron beam (right). The clear difference between Au and Pd is revealed by the Z-contrast, due to the difference in the atomic numbers of the two elements (Z_{Au}=79, Z_{Pd}=46). From Ref. [81]........ 24

1.7. HAADF-STEM analysis (left) and EELS mapping (centre), together with the proposed structural model (right) for the Au-decorated Pd_{147} nanoclusters used for the glucose oxidation process. Here, HAADF-STEM information and EELS mapping have been used for a better understanding of the structural arrangement of atoms in AuPd nanoclusters. Taken from Ref. [84]........ 25

1.8. (left) TEM image of three-layer AuPd nanoparticles produced via chemical synthesis methods; (right) EDX line profile of a three layer AuPd nanoparticle. Taken from Ref. [23]........ 26

2.1. A schematic representation of a potential energy surface (PES) of a cluster. In this schematic representation, the potential energy surface has two local minima (LM) and a global minimum (GM)........ 38

2.2. Schematic representation of a multiple-funnel PES with a monotonic sequence basin. From Ref. [11]........ 39

2.3. Schematic representation of the roulette wheel selection method employed in the BCGA. A fitness value, f_i, is assigned to each individual in the population. The probability of selecting the individual will be corresponding to its fitness value (i.e. to the width of each slot in the roulette wheel selection method). From Ref. [5]................ 41
2.4. Schematic representation of the BCGA crossover operator. Adapted after Ref. [8]................ 42
2.5. The mutation operator in BCGA. This operator introduces new genetic material in the newly generated cluster population. From Ref. [8]................ 42
2.6. Schematic representation of the BHMC algorithm. The BHMC starts from an initial cluster configuration and applies various operators on the atoms of the cluster (“exchange”, “shake”) in order to minimize the total energy of the cluster. Adapted after Ref. [21]. See text for the meaning of A, B, C, D, E and F................ 45
2.7. The high symmetry Leary Tetrahedron structure found for a composition of Pd_{52} Au_{46} for the 98-atom AuPd clusters................ 47
3.1. A schematic representation of the diagram of rays in a TEM. Adapted after Ref. [5]................ 61
3.2. Schematic illustration of a solid angle and aperture semi-angle, θ. Adapted after Ref. [5]................ 62
3.3. Image formation mechanism in a TEM. From Ref. [12]................ 66
3.4. Schematic diagram illustrating the phase shift introduced by the spherical aberration. From Ref. [5]................ 67
3.5. Schematic representation of Bright Field (a) and Dark Field (B) TEM. Adapted after Ref. [15]................ 71
3.6. Schematic representation of STEM showing the position of the detectors. In this thesis, both the HAADF and BF detectors have been used. Adapted after Ref. [16]................ 72
3.7. Schematic illustration of the formation of the BF STEM image. Due to the overlap of discs, the incident wave vectors, $\vec{k}_i$ and $\vec{k}_i + \vec{q}$ are scattered by the specimen and will interfere in the plane of the detector, forming a final vector, noted $\vec{k}_f$; the phase difference between the two incident plane vectors will depend on the probe position. Adapted after Ref. [18]................ 73
3.8. Diagram of the EDX detector................ 78
3.9. Schematic representation of the X-ray principle................ 78
4.1. Excess energy for 98-atom Pd_mAu_{98-m} clusters determined for the: DFTfit (blue curve), Exp-fit (red curve) and Average (green curve) Gupta potentials. 90
4.2. Structural motifs for selected Pd_mAu_{98-m} clusters using the DFT-fit Gupta potential................ 91
4.3. Structural motifs found for selected Pd_mAu_{98-m} clusters using the Exp-fit Gupta potential................ 93
4.4. Structural motifs found for selected Pd_mAu_{98-m} clusters using the Average Gupta potential................ 95
4.5. Step by step construction of the LT structure: a) 20-atom central tetrahedron with high proportion of (111) facets; b) 56-atom stellated tetrahedron built on the original 20-atom tetrahedron; c) the complete Leary tetrahedron structure. Adapted after Ref. [2]................ ..100

4.6. Plot of the LT excess energy as a function of Pd content for the high symmetry 98-atom AuPd clusters modelled by Gupta DFT-fit (blue dots), Exp-fit (red dots) and Average (green dots) potentials.................................... ..101

4.7. DFT relaxation for the ‘putative’ GM for the DFT-fit (blue line), Exp-fit (red line) and Average (green line) Gupta potentials. The compositional interval is $Pd_{46}Au_{52}$-$Pd_{52}Au_{46}$... ..102

4.8. Structures of AuPd clusters (generated as GM for the three Gupta potentials in the interval $Pd_{46}Au_{52}$-$Pd_{52}Au_{46}$ after DFT relaxation and before the optimization of the chemical ordering... ..103

4.9. Excess energy plot comparing LT (black line), M-Dh (green line), Ico (red line) and FCC-HCP (blue line) structural motifs in the compositional range $Pd_{46}Au_{52}$-$Pd_{52}Au_{46}$; (a)-(c) results of BHMC chemical ordering optimization for Gupta DFT-fit, Gupta Exp-fit and Gupta Average potentials..................... ..105

4.10. Excess energy of LT (black line), M-Dh (green line), Ico (red line) and FCCHCP (blue line) obtained with the Average potential. The plot represents the relaxation of these structural motifs at the DFT level, after the optimization of the chemical ordering... ..106

5.1. Estimated exponent α in the relationship $I \sim kZ^{\alpha}$ between annular dark field intensity I and atomic number Z as a function of the collection angle admitted by the detectors. (●) Without calibration analysis; (●) With calibration analysis. Names in the plot refer to the first authors of the corresponding references: Ferrer et al. [26], Kirvanek et al. [27], Wang et al. [33], Voyles et al. [35], Takeguchi et al. [36], Lakner et al. [37], Di Vece et al. [38], Allen et al. [39], Liu et al. [40]... ..115

5.2. Typical HAADF-STEM images of (a) evaporated Pd and (b) evaporated Au nanoparticles on amorphous thin film. In the vicinity of nanoclusters, encircled, single atoms can be observed... 116

5.3. HAADF-STEM integrated intensities for Au (a)-(f) and Pd (g)-(l) for various collection angles... 117

5.4. HAADF-STEM integrated intensities for monomers (a), dimers (b) and trimers (c) as a function of collection angle. Blue lines: Au; Red lines: Pd...... ..118

5.5. Variation of α exponent as a function of inner collection angle (mrad). ● Calculated monomers; ♦ Calculated dimers; ★ Calculated trimers; ● Comparative analysis: experimental data from Ref. [34] for 923-atom size selected Au and Pd clusters; ■ Comparative analysis: 923-atom size selected Au and Pd clusters experimental data from Ref. [33]. Solid line represents best fitting... ..119

5.6. Logarithmic fitting ($y = a * \ln(\theta) + b$) for calculated monomers, dimers and trimers. Value of the α exponent vs. inner acceptance angle: ♦ Calculated monomers; ● Calculated dimers; ★ Calculated trimers; ● Comparative analysis with size-selected clusters, adapted from Ref. [34]; (—) Best fitting for monomers – R^2=0.9079; (—) Best fitting for dimers - R^2=0.9017; (—) Best fitting for trimers – R^2=0.9079; (—) Best fitting for adapted data from Ref. [33], R^2=0.9817, where R is the fitting residual....................................... ..121

5.7. Linear fitting ($\alpha = a \cdot \theta + b$) for calculated monomers, dimers and trimers; Comparative analysis with data in [41]. Value of the α exponent as a function of the inner acceptance angle. (♦) Calculated monomers; (●) Calculated dimers; (★) Calculated trimers; (●) Comparative analysis with 923-atom size selected clusters adapted from Ref. [41]; (—) Best fitting monomers – R^2=0.9804; (—) Best fitting dimers - R^2=0.924; (—) Best fitting trimers – R^2=0.9187; (—) Best fitting for data adapted from Ref. [34], R^2=0.9504, where *R* is the fitting residual.......... ..122

5.8. (a) Dark Field and (b) bright field images of Au$_{24}$Pd$_1$ clusters supported on MWCNTs taken simultaneously. The electron dose is 3.32×10^3 electrons/Å^2. 124

5.9. (a)-(f) HAADF-STEM images of Au$_{24}$Pd$_1$ nanoparticles supported on MWCNTs.......... ..125

5.10. (a) HAADF-STEM image showing the Au$_{24}$Pd$_1$ clusters; (b) Histogram of the cluster size measured by averaging the long and short axes of the 2D projection.......... ..126

5.11. (a) Histogram of the HAADF-STEM intensity integrated over each Au$_{24}$Pd$_1$ cluster after background subtraction; (b) Histogram of the integrated intensity for Au atoms found in the vicinity of Au$_{24}$Pd$_1$ clusters; an example of the image shown in the inset, where a single atom is encircled; (c) Histogram of the integrated intensity for Au atoms (circled) found in the area between Au nanoparticles on amorphous carbon film prepared via thermal vapour deposition.......... ..127

5.12. A plot of the HAADF-STEM integrated intensity, from Figure 5.11 (a), as a function of the aspect ratio of each cluster measured by the long axis over the short axis.......... ..128

5.13. (a) Serial acquisition analysis for an electron dose of 3.32×10^3 electrons/Å^2; (b) Serial acquisition analysis for an electron dose of 1.66×10^3 electrons/Å^2. Also shown are the analyses of the variation of the relative HAADF-STEM integrated intensities as a function of image sequence number.......... ..129

5.14. GM cluster obtained using BHMC-DFT approach (a) and other high-energy isomers (b) – (f). The binding energies have also been included.......... ..133

5.15. Isomers obtained with the empirical Gupta potential (a) DFT-fit; (b) Exp-fit; (c) Average parameters. The binding energies have also been included.......... ..133

5.16. Löwdin charge analysis: (a) Au$_{25}$ clusters; (b) Au$_{24}$Pd$_1$ clusters.......... ..135

6.1. The AuPd phase diagram. Adapted from Ref. [16].......... ..157

6.2. Schematic representation of the Edwards 306 Turbo evaporation system used for the production of AuPd nanoparticles.......... ..159

6.3. (a) Low magnification HAADF-STEM images of as-deposited nanoparticles; (b) statistical size distribution – mean value of diameters: 1.70±0.34 nm; (c) High magnification HAADF-STEM image of an as-deposited nanoparticle; (d) Diffraction pattern of the nanoparticle marked with yellow frame in (c).......... ..160

6.4. (a) HAADF-STEM image of evaporated Au nanoparticles deposited on amorphous carbon substrate; (b) Lattice spacing analysis performed on the line profile in (a); (c) HAADF-STEM image of evaporated Pd nanoparticles deposited on amorphous carbon substrate; (d) Lattice spacing analysis performed on the line profile in (c).......... ..161

6.5. HAADF-STEM images of two evaporated mixed AuPd nanoparticles annealed for (a) 60 and (c) 120 minutes at 500 K; (b) Diffraction pattern of the nanoparticle marked with square frame in (a), revealing main and secondary spots, indication of superlattice formation; (d) Diffraction pattern of the nanoparticle marked with square frame in (c).. ..163

6.6. Schematic representation of the (a) $L1_2$ and ordered crystallographic phases in <100> orientation. Red circles: Palladium atoms; Grey circles: Au atoms; (b) General representation of the $L1_2$ ordered phase. Taken from Ref. [16]).... ..165

6.7. (a) HAADF-STEM image of a layered evaporated AuPd nanoparticle annealed at 500 K for 120 minutes; (b) Diffraction pattern of the nanoparticle marked with yellow square in (a); (c) HAADF-STEM image of a core-shell AuPd nanoparticle annealed at 500 K for 120 minutes; (d) Diffraction pattern of the nanoparticle marked with yellow square in (c). Yellow arrow pointers indicate the presence of PdO incompletely surrounding the nanoparticle......... ..167

6.8. (a) HAADF-STEM image of a layered evaporated AuPd nanoparticle annealed at 500 K for 180 minutes; (b) Diffraction pattern of the nanoparticle in (a); (c) HAADF-STEM image of a core-shell AuPd nanoparticle annealed at 500 K for 180 minutes; (d) Diffraction pattern of the nanoparticle marked with yellow square in (c). Yellow arrow pointers indicate the presence of PdO surrounding incompletely the nanoparticle.. ..168

6.9. (a) HAADF-STEM image of a mixed AuPd nanoparticle annealed for 120 minutes at 500 K; Yellow frame represents the ROI for which the diffraction pattern was considered; Blue frame represents the ROI where the EDX mapping was performed; (b) Diffraction pattern for the nanoparticle in (a); (c) Mapping of Pd, Au and O respectively.. ..170

6.10. (a) HAADF-STEM image for core-shell AuPd nanoparticle annealed for 120 minutes at 500 K; Yellow frame represents the ROI for which the diffraction pattern was taken; Blue frame represents the ROI where the EDX mapping was performed; the yellow arrow pointer indicates the presence of a diffused PdO layer on the corner of the nanoparticle; (b) Diffraction pattern for the nanoparticle in (a); (c) Mapping of Au, Pd and O respectively......................... ..171

6.11. Left: HAADF-STEM image of PdO layer interconnecting three nanoparticles. Right: a magnified image of the region marked by the red square, revealing the well-ordered structure of the PdO layer diffused on the carbon substrate following the annealing of AuPd NP for 120 minutes, in situ, at 500 K. Yellow line indicates the line profile used in Figure 6.12 (c) for the estimation of PdO layer thickness... ..173

6.12. (a) HAADF-STEM image of pure evaporated Pd nanoparticles deposited on amorphous carbon. Encircled, in the vicinity of nanoparticles, single atoms can be observed, which have been used for the calibration of the PdO layer thickness. (b) Line profile of a Pd atom marked with yellow line in (a); (c) Line profile of the PdO layer marked with a yellow line in Figure 6.11........... ..174

6.13. (a) HAADF-STEM image of evaporated Au nanoparticles deposited on amorphous carbon and annealed in situ for 120 minutes at 500 K; (b) HAADF-STEM image of evaporated Pd nanoparticles supported on amorphous carbon and annealed in situ for 120 minutes at 500 K................... ..175

6.14. (a) HAADF-STEM image of chemically synthesized AuCo nanoparticles deposited on the surface of lacey carbon films. After annealing for 12 hours at 500 K in oxygen atmosphere, a diffused, thin CoO film can be observed. Adapted from Ref. [38]... ..177

Table of contents

Abstract i

Acknowledgments ii

List of figures iii

List of abbreviations ix

1. Introduction

1.1. Overview……………………………………………………………..…1

1.2. Chemical ordering in bimetallic nanoalloys…………………………………4

1.3. Factors influencing segregation, mixing and ordering patterns in bimetallic nanoparticles……………………………………………………………………6

1.4. Methods of production for bimetallic nanoparticles……………………....…8

1.5. Summary-production methods……………………………………….....…20

1.6. Characterization of bimetallic nanoparticles……………………………..21

1.6.1. Application of (S)TEM and Energy Dispersive X-ray (EDX) spectroscopy techniques for the characterization of AuPd bimetallic systems…………………………………………………………….22

1.7. Research objectives…………………………………………………………27

1.8. Conclusions…………………………………………………………………29

2. Theoretical investigations of bimetallic nanoparticles: empirical potentials and DFT calculations.........…....………………………………………........36

2.1. Overview…………………………………………………………..…...36

2.2. Exploring Potential Energy Surfaces (PES)…………………………….…37

2.2.1. Global topology of the PES……………………………………….....38

2.2.2. Genetic Algorithms ………………………………………….......39

2.2.3. The Basin Hopping Monte Carlo (BHMC) algorithm………………44

2.2.4. Shell optimization routine……………………………………...46

2.2.5. Empirical potentials: the Gupta potential……………………………47

2.3. Density Functional Theory……………………………………....……49

2.4. Conclusions…………………………………………………....…55

3. Experimental characterization of nanoparticles: STEM...............................59

3.1. Overview……………………………………………………….……...59

3.2. The Instrument....………………………………………….………..59

3.2.1. The illumination system……………………………………………..61

3.2.2. High resolution TEM. Image formation……………………….………66

3.3. Types of contrast……….….……………………………………….………68

3.4. The High Angle Annular Dark Field (HAADF) Scanning Transmission Electron Microscope (STEM)...……………………………………………71

3.4.1. BF STEM...……………………………………………………72

3.4.2. HAADF-STEM…………………….……………………………74

3.4.3. Probe formation and lens aberrations………………………………..76

3.5. Energy Dispersive X-ray (EDX) Spectroscopy……………………………..77

3.6. Conclusions………………………………………………………………79

4. DFT studies of structure and energetics of 98-atom AuPd nanoparticles...………83

4.1. Overview…………………………………………………………………83

4.2. Introduction……………………………………………………………………83
4.3. Computational details…………………………………………………………86
  4.3.1. Genetic Algorithm parameters...……………………………………….86
  4.3.2. Basin Hopping Monte Carlo parameters...………………………….…..86
  4.3.3. DFT calculations parameters……………………………………….....87
  4.3.4. Gupta Pd-Au parameters.……………………………………………….87
4.4. Results and discussions.……………………………………………………..88
  4.4.1. Global optimization of 98-atom AuPd nanoclusters…………………89
  4.4.2. Determination of number of homonuclear and heteronuclear bonds……………………………………………………………………97
  4.4.3. Leary tetrahedron (LT) clusters…………………………………….....98
  4.4.4. DFT local relaxations………………………………………………….101
  4.4.5. Optimization of chemical ordering and DFT relaxations…………..104
4.5. Conclusions....…………………………………………………...………107
5. **Direct atomic imaging and density functional theory study of the $Au_{24}Pd_1$ cluster catalyst**……………………....…………………………………110
5.1. Overview.……………………………………………………………………..111
5.2. Z-contrast imaging of single atoms.....……………………………………..114
  5.2.1. Methodology………………………………..……………………115
5.3. HAADF-STEM characterization of bimetallic ligand-free $Au_{24}Pd_1$ nanoclusters supported on MWCNTs…………………………………...…123
5.4. Theoretical analysis of bimetallic $Au_{24}Pd_1$ clusters…………….………….130
  5.4.1. Computational details…………………………………...........……131

5.4.2. Results and discussions…………………………………….....…….132

5.5. Charge transfer……………………………………………………..134

5.6. Conclusions…………………………………...……………………136

6. Structures of bimetallic AuPd nanoparticles prepared by physical vapour deposition…...…………………………………………………...……..154

6.1. Overview………………………………………...………………154

6.2. Preparation of bimetallic AuPd nanoparticles via physical vapour deposition…………………………………………………………..157

6.3. As-deposited AuPd sample………………………...………….........….158

6.4. AuPd samples upon annealing..161

6.4.1. Formation of ordered $L1_2$ crystallographic phases upon annealing…………………………………………………………161

6.4.2. Segregation effects…………………………………………………165

6.4.3. Oxidation effects…………………………………………………172

6.4.4. Size dependency……………………………………….....……….177

6.5. Conclusions……………………………...……………………………180

7. Conclusions and future work……………………...……………...….……184

8. Appendix 1……………………………………………………….....…...188

Abbreviations

BF – Bright Field

BHMC – Basin Hopping Monte Carlo

BCGA – Birmingham Cluster Genetic Algorithm

CBED – Convergent Beam Electron Diffraction

DFT – Density Functional Theory

DF – Dark Field

EP – Empirical Potential

FEG – Field Emission Gun

GA – Genetic Algorithm

HAADF – High Angle Annular Dark Field

IGC – Inert Gas Aggregation

MD – Molecular Dynamics

PES – Potential Energy Surface

RF – Radio Frequency

STEM – Scanning Transmission Electron Microscope

TEM – Transmission Electron Microscope

ToF – Time of Flight

Chapter I

1.1. Overview

Typically, nanoparticles can be defined as an agglomeration of atoms and molecules, in the range of 1-100 nm. They can constitute of one or more species of atoms (or molecules) and can exhibit a wide range of size dependent properties.

Within the aforementioned size range, nanoparticles bridge the gap between small molecules and bulk materials [1] in terms of energy states. Nanoparticle properties are different from those of bulk materials as a consequence of the high surface-to-volume ratio; by having a large proportion of constituent atoms on the surface, they are excellent candidates in the domain of catalysis. Size shrinkage has been found to be the reason behind many novel physical and chemical properties, which result in a wide range of applications with economical benefits; this has motivated increased international research efforts in this field.

Bimetallic nanoparticles have received considerable attention in recent years [2] for their unique properties, which are significantly different from their monometallic counterparts, ranging from nanocatalysis [3-6] to optics [7-8] and medicine [9]. These properties are a consequence of a good control of the size distribution, composition and degree of chemical ordering [10]. Due to the wide range of commercial applications (e.g. in automotive and power generation industries), a better understanding of heterometallic interactions within nanoparticles is necessary. In domains such as nanocatalysis, the need for multimetallic catalytic systems has emerged due to several factors including reducing the price of the active catalyst and an increase in activity and/or chemical selectivity. As an example, in fuel cell design [11, 12] a reduction of the amount of platinum (Pt) in the cells has been attempted by alloying the Pt with a less expensive metal. This has resulted in an enhanced catalytic activity at the electrodes [13, 14] and resistance to poisoning [15]. In order to take advantage of the bimetallic alloying within the nanoparticles, a better understanding of the structural, chemical and electronic modifications induced by the addition of a secondary metal need to be fully understood [16, 17].

One of the main scientific reasons for researching into structure and energetics of bimetallic nanoparticles is that their physical and chemical properties can be widely tuned by simply modifying the composition and the atomic arrangement, as well as by modifying their sizes. Bimetallic nanoparticles exhibit special properties which appear at magic sizes, but can also have an enhanced stability appearing at certain compositions [2]. The nanoparticles surface segregation and structure are important features, since they have a large degree of influence over the overall physical and chemical activity. Apart from segregation effects, due to their finite size, bimetallic nanoparticles can also exhibit special properties, different from their bulk counterparts, since metals that may be immiscible in bulk can alloy at the nanoscale level (e.g. Silver (Ag) and Iron (Fe)) [18]. The improved efficiency of bimetallic nanoparticles can be also attributed to the electronic effects that can be significantly modified with respect to their monometallic counterparts. Characterizing the nanoparticles experimentally using various imaging techniques is of utmost importance for a better understanding of their segregation patterns, degree of control over size distribution, composition, stability, structure evolution at high/low temperatures, etc., but, most importantly, in order to better understand their activity in the field of nanocatalysis. Combining experimental analysis with theoretical ones is one of the main goals in nanotechnology. Theoretically, the first problem that exists is to find, given the size and composition of a bimetallic nanoparticle, the most stable structure (i.e. to determine the geometry and the chemical ordering). This is an important goal, since the most stable structures identified theoretically (i.e. the global minimum (GM) structures) are the most probable candidates to appear in a cluster experiment [19].

One of the main limitations in developing hybrid theoretical/experimental approaches is the size gap. Currently, due to computational limitations, Density Functional Theory (DFT) calculations are limited to sizes up to 100-150 atoms [1], whereas often, experimental applications involve much larger sizes. However, even performed at small sizes, structural predictions/investigations at the DFT level are important as they consist an important step in understanding segregation effects in bimetallic nanostructures, since smaller nanoparticles can be considered "seeds" for the growth of larger nanoparticles. As discussed in Ref. [1], one of the most efficient methods to optimize globally bimetallic nanoparticle systems up to 150 atoms is to perform an initial exploration of the potential energy surfaces (PES) of bimetallic clusters, then, once the global minimum has been roughly located at a certain size and composition – to refine the search (e.g using Basin Hopping Monte Carlo – see Chapter IV), followed by optimizations at DFT level. When the number of atoms is less than a few tens (presently around 50 atoms), direct searches at the DFT level are possible [20]. In Chapter V of this thesis we have shown that a hybrid theoretical and experimental analysis of 25-atom AuPd nanoparticles is possible, regarding the characterization of chemically-synthesized single Pd doped Au_{25} nanoclusters via Scanning Transmission Electron Microscope (STEM) and theoretical methods involving a direct search at the DFT level using Basin Hopping Monte Carlo algorithm.

This thesis aims to bring a contribution in offering a dual experimental and computational analysis of the AuPd bimetallic nanoparticles, for a better understanding of morphology, structure, and segregation in small and large nanoparticles systems.

1.2. Chemical ordering in bimetallic nanoalloys

There are four main types of chemical ordering in bimetallic nanoalloys (Figure 1.1), which depend on the way in which atoms of elements A and B are arranged within the same nanoparticle [10, 21]:

(a) ***Core-shell nanoparticles***: consists of a shell of one type of atom (B) surrounding a core of another (A) (Figure 1.1 (a)). This pattern is denoted by $A_{core}B_{shell}$ and is common for a large class of nanoparticles. Various thermodynamic considerations, discussed further in the thesis, lead to the segregation of metals within core or shell. A subset of this category consists in ***multishell ('onion-like') nanoparticles.*** These nanoparticles have alternating A-B-A shells [1], more often encountered in medium-large size clusters (Figure 1.1 (d)). These structures have been predicted by theoretical simulations AuPd nanoclusters [10, 22, 24], and experimentally, for the chemically prepared gold-palladium (AuPd) nanoparticles, exhibiting an alloy inner core, a Au-rich intermediate shell and a Pd-rich outer shell [23, 25].

(b) ***Layered nanoparticles***: consist of layered A and B nanoparticles (Figure 1.1 (b)). They are commonly referred in the literature as Janus particles, and consist of two types of nanoparticles sharing a common interface [1]. These types of nanoparticles tend to *minimize* the number of bonds between element A and B. These types of nanoparticles have been successfully predicted theoretically for the case of small-size bimetallic AuPd nanoparticles (Ref. [24]) and experimentally, for chemically-synthesized nanoparticles, in Ref. [25].

(c) ***Mixed nanoparticles***: can be either random or ordered (Figure 1.1 (c)). Randomly mixed alloys correspond to solid solutions, whereas ordered nanoalloys correspond to ordered arrangements of A-B atoms. Both have been predicted for the case of bimetallic AuPd nanoparticles in Refs. [21, 26].

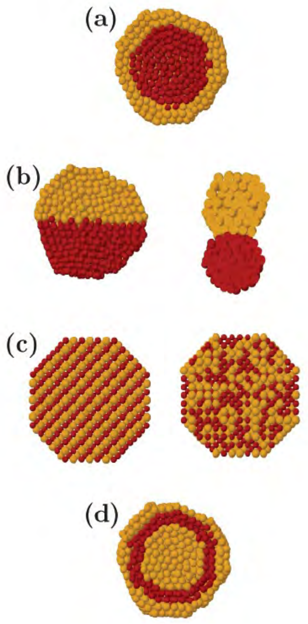

Figure 1.1. Schematic representation (cross section) of various compositions that can be obtained for bimetallic nanoparticles: (a) core-shell; (b) Janus nanoparticles and phase-separated bimetallic nanoparticles; (c) ordered alloy and random mixture alloy; (d) onion-like bimetallic nanoparticles. Taken from Ref. [10].

1.3. Factors influencing segregation, mixing and ordering patterns in nanoalloys

Segregation of metals within a bimetallic system can be understood as interplay between the following effects [1, 10].

- **(a)** **Bond strength –** the relative strengths of A-A, A-B and B-B influences the ordering in bimetallic nanoparticles. Strong homonuclear A-A or B-B bonds influence segregation in bimetallic nanoparticles. If A-B bonds are stronger, this will favor inter-mixing of metals.
- **(b)** **Nanoparticles surface energies –** the metal with the highest surface energy tends to occupy core positions.
- **(c)** **Atomic radius –** the element with the smallest atomic radius tends to occupy core positions; this will influence the relief of strain introduced by inter-mixing of two metals.
- **(d)** **Charge transfer –** in bimetallic nanoparticles, charge transfer could occur from the most electronegative metal to the least electronegative one.
- **(e)** **Strength of binding to surface ligands –** for the case of passivated nanoclusters, the element that binds more strongly to the ligands may be pulled out to the surface of the nanoclusters. This has been predicted theoretically for the case of AuPd nanoclusters, and demonstrated in Ref. [10].

In case of bimetallic nanoparticles, as mentioned previously, exploring the Potential Energy Surface (PES) of a system is an extremely difficult task, due to the presence of *homotops*, a term that has been first introduced by Julius Jellinek (Ref. [2]). This refers to isomers (A_mB_n) with a fixed number of atoms ($N=m+n$) and composition (*m/n ratio*) which have the same geometrical arrangement of atoms but differ on how atoms A and B are arranged (see Figure 1.2). The number of homotops for a bimetallic nanoparticles is [27]:

$$N_H = \frac{N!}{N_A!N_B!} \tag{1.1}$$

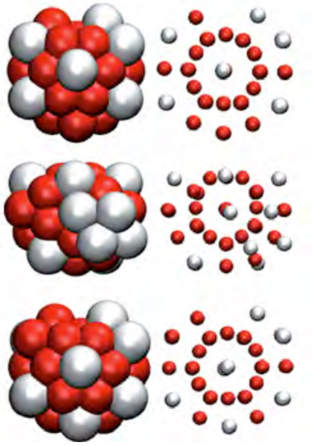

Figure 1.2. A schematic representation of the presence of homotops for $Ag_{11}Ni_{27}$ nanoclusters. For the same size and composition, the spatial arrangement of atoms is different. The nanoparticles on top and middle rows are two isomers of the $Ag_{11}Ni_{27}$, whereas the nanoparticles on the top and bottom rows are homotops of the same cluster. Taken from Ref. [28].

We can thus expect that as the cluster size increases, the number of homotops in a bimetallic nanoparticle would also increase factorially, making the task of identifying the GM structure a difficult issue. For example, a 20 atom AuPd bimetallic nanoparticles ($Au_{10}Pd_{10}$) has approximately N_H=184756 homotops [29], and as the size doubles ($Au_{20}Pd_{20}$), the number of homotops is $N_H=1.38 \times 10^{11}$, an issue that makes the global optimization problems very difficult tasks.

1.4. Methods of production of bimetallic nanoparticles

Previous experimental studies have emphasized that it is possible to design various configurations of AuPd nanoparticles: core-shell configurations (e.g $Pd_{core}Au_{shell}$ [21], $Pd_{shell}Au_{core}$ [30]), three-layer AuPd configurations [25] and mixed structures [31]. *Chemical synthesis methods* can produce bimetallic nanoparticles with controlled size and morphology [21], but the kinetic processes that are involved in the production methods do not offer a high degree of control over the appearance of core-shell configurations [32] and size distribution. *Physical deposition methods* can offer a higher degree of control over the size and segregation in bimetallic nanoparticles (see below). However, this method is more suitable for the production of model nanoparticles and are not extremely feasible for applications in industrial nanocatalysis for example. Each deposition method will be reviewed shortly, below.

A. Physical production methods. One of the most common experimental techniques in generating bimetallic nanoparticles is the *cluster beam* technique. This technique is one of the most versatile and flexible production methods in terms of cluster size selection, choice of materials and supports, control over deposition energy, narrow particles size distribution and high substrate coverage, making them versatile for producing nanoparticles for model nanocatalysis or for applications such as optics [1]. The main steps in cluster beam production methods consist in: (a) *vaporization*: production of atoms and molecules in gas phase. (b) *nucleation* – involving the formation of nucleation seeds in the gas phase; (c) *growth* – addition of more atoms to the nucleation seeds formed a priori. Conditions in cluster source (Argon (Ar) or Helium (He) gas flow) could be controlled in order to produce various configuration bimetallic nanoparticles and (d) *coalescence* – formation of larger clusters by means of merging of small clusters. This deposition methods has been used for the case of production of bimetallic AuPd nanoparticles, as described in the paper of Perez-Tijerina et al. [33].

Cluster beam sources include the following components:

1. *Magnetron sputtering*: Argon plasma is ignited over a target by applying either a *dc* or *rf* potential and confined by a magnetic field [34, 35]. Ar^+ ions in the plasma are then accelerated onto the target, resulting in sputtering. By carefully controlling the conditions of nucleation and sputtering (i.e. Ar and He gas flows), it has been proved that various configuration of bimetallic nanoparticles can be obtained [36], as reported for the case of AuCu bimetallic nanoparticles.

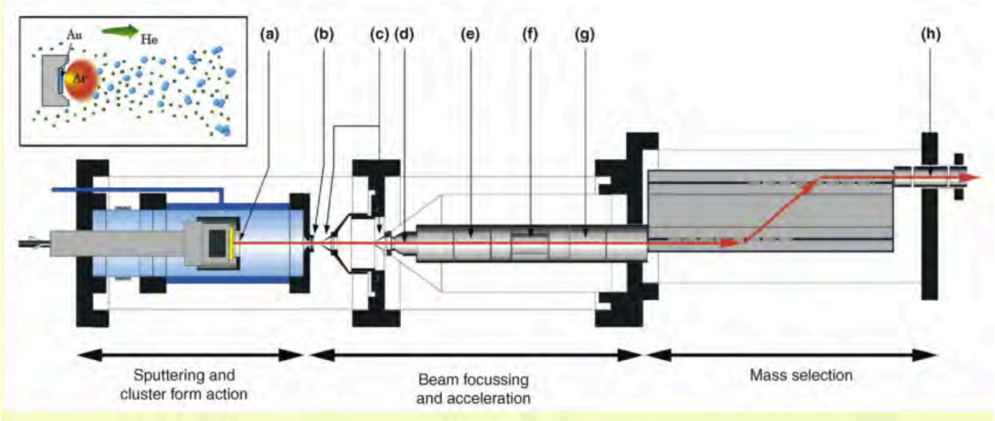
Au
He
Ar
(a)
(b)
(c) (d)
(e)
(f)
(g)
(h)
Sputtering and cluster form action
Beam focussing and acceleration
Mass selection

Figure 1.3. A magnetron sputtering gas aggregation cluster beam source. The setup consists in: (a) magnetron gun with a target; (b) adjustable nozzle; (c) electrostatic skimmers; (d) high voltage lens; (e) Einzel lens for controlling the kinetic energy of the cluster; (f) deflection plates for the spatial control of the cluster beam; (g)-(h) Einzel lenses. All the different chambers of the cluster beam are differentially pumped. *Inset*: Formation of ionized clusters in Ar plasma by gas condensation. Taken from Ref. [37].

In Ref. [36], condensation conditions within the cluster source have been changed in order to obtain either $Au_{core}Cu_{shell}$ or $Cu_{core}Au_{shell}$ nanoparticles with controlled sizes for various applications ranging from optics to catalysis. For AuPd nanoparticles, a similar manipulation of segregation patterns has not yet been attempted for nanoparticles produced using cluster sources.

2. *Laser ablation sources*: in such sources, either two monometallic targets [35], a bimetallic alloy target, a single alloy rod target [38] or mixed metallic powders [39] could be vaporized by the incident beam in order to produce bimetallic nanoparticles. This method

has been used in Ref. [35] for the production of $Au_m(X)_n$ bimetallic nanoparticles (where X=Al, Fe, Co, Ni). Typically, a beam from a solid state laser is focused on a rod/plate that is driven in slow motion such that new areas of their surfaces are continually exposed to the laser beam. Laser ablation can be combined with gas assisted cooling [40]. The vaporized material is incorporated in a carrier gas (typically He); the vapor is cooled causing cluster formation; the cluster beam is then ejected through a nozzle forming a beam of supersonic velocity. The clusters produced with laser ablation sources could be either charged or neutral [41], with a size distribution typically ranging from few hundred atoms per cluster [42]. These types of sources are very versatile in the production of binary clusters [43] and can employ a single laser source and dual target [44] or even dual beam and dual target laser ablation cluster sources [35].

3. *Ion sputtering cluster beam sources:* A metal target is bombarded with high-energy inert gas ions (such as Kr^+ or Xe^+) with energies in the range of 10-30 keV and currents of approximately 10 mA [22, 45].
4. *Pulsed arc cluster ion sources:* The vaporization of monometallic or bimetallic targets is achieved by passing an intense electrical discharge through them [22, 46]. These types of sources are especially effective for the vaporization of materials with high value of melting points [46]. In this type of cluster sources, the target material is vapourized by passing an intense electrical discharge through it. As in the above cases, the resultant vapour is cooled by a carrier gas. The species produced by this cluster sources are typically just 10% charged, the rest being neutral species [41].

5**.** *Physical vapor deposition (PVD) of bimetallic nanoparticles* **–** this method has been traditionally used for the production of monometallic thin films on various surfaces by means of thermal evaporation in vacuum, plasma sputtering, etc., assuring that atoms aggregate into small particles. The clusters assembly is made on the surface and not in gas phase [47], in contrast to the cluster beam sources. The nanoparticles size distribution is typically broader than for the case of other deposition methods. The method offers a large degree of control over the rate of deposition, or substrate temperature and a certain degree of control over bimetallic nanoparticles morphologies, as shown in Chapter VI.

PVD methods are typically employed for the production of monometallic nanoparticles. However, bimetallic thin films have also been produced with PVD, as reported in Ref. [48], where long range ordered structures with <001> type of orientation have been reported. Although this method is versatile and relatively easy to implement, there is however no report in the literature concerning production of bimetallic (AuPd) nanoparticles with PVD. In this thesis one of the approaches used for the production of bimetallic AuPd nanoparticles is PVD (see Chapter VI), followed by subsequent annealing at 500 K, *in situ*. This procedure has led to various morphologies of nanoparticles, from mixed to segregated configurations.

The formation of clusters begins with the deposition of evaporated atoms to the substrate. The atoms in the vapor phase arrive on the substrate and adhere to it, diffuse and find equilibrium positions [47]. The atoms in the vapor phase come in contact with the surface and may create bonds with the constituting atoms of the surface.

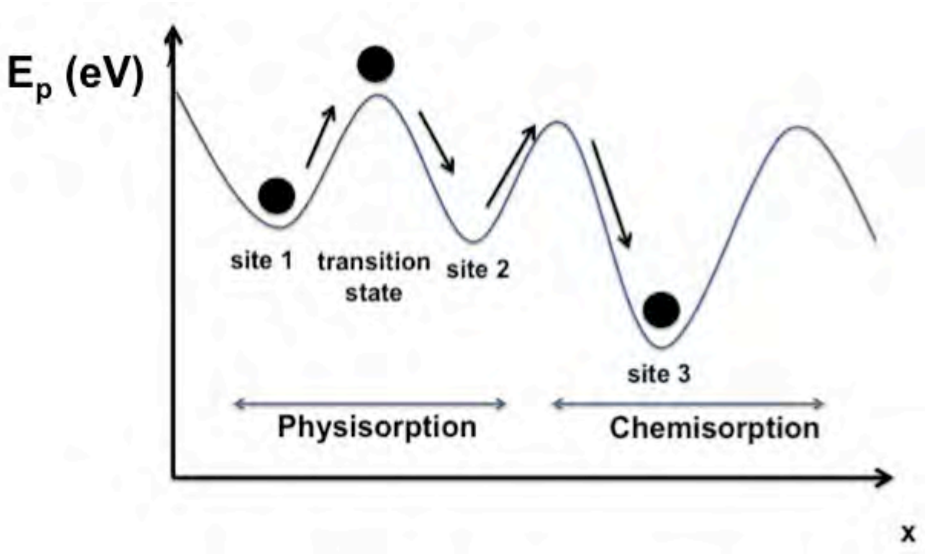

Figure 1.4. The plot of the potential energy vs. the position (*x*) along the surface during the surface diffusion process. Adapted from Ref. [47]

The value of the substrate temperature needs to be sufficiently low such that the vapor phase will be supersaturated with respect to the substrate. If the vapor atoms are forming chemical bonds with the substrate atoms, then a reduction in potential energy will take place (Figure 1.4). The pressure p of the arriving vapor needs to exceed the equilibrium value of pressure, p_e at the substrate temperature.

For the pressure p, the free energy per atom of the vapor above the free energy at pressure p_e is estimated as the work to increase the vapor pressure p_e to p at constant temperature; the work will equal $k_B T \ln\left(\frac{p}{p_e}\right)$, where k_B is the Boltzmann constant and T is the vapor temperature.

According to Ref. [47], the atoms arriving on the substrate reside in equilibrium energy wells. The atoms will oscillate in the potential wells due to the thermal activation and, if they will acquire sufficient energy, will "hop" between adjacent equilibrium wells. This is the principle of surface diffusion. The hopping rate increases with the substrate temperature. If the substrate is uniform, then diffusion will occur randomly, with no net mass transportation on the macroscopic scale; if the surface of the substrate is not uniform, then a net mass transport along the surface will occur at the macroscopic scale.

The presence of crystallographic defects on the substrate (e.g. dislocations, grain boundaries, etc.) are preferred sites for adatom attachment. If the diffusion length is large in comparison to the spacing between surface defects, then adatoms tend to encounter defects and attach to them. This is called *heterogeneous nucleation*. If the spacing between surface defects is large in comparison to the diffusion length, then the migrating atoms tend to lower the energy of the system and bind together with mutual encounters and form clusters. This is called *homogenous nucleation*.

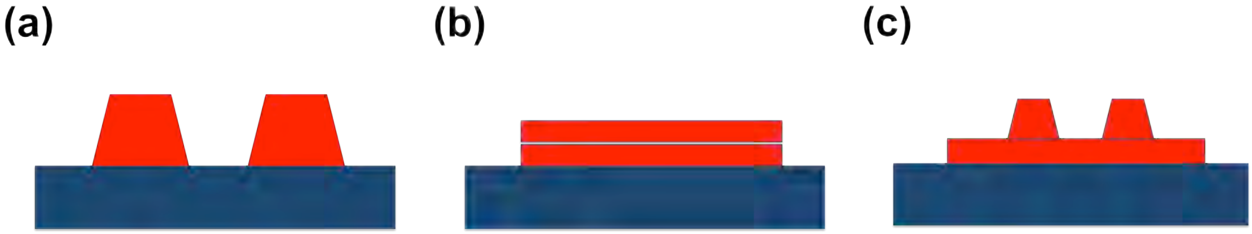

Figure 1.5 (a) Volmer-Weber; (b) Frank-van-der-Merwe; (c) Stranski-Krastanov growth modes. After Ref. [47].

Here, three growth modes can be discerned, based on the relationship between: γ_s (substrate-surface energy), γ_f (“film” – surface energy), γ_i (film-substrate energy) [47] (see Figure 1.5).

- **Volmer-Weber** (island) - $\gamma_s < \gamma_i + \gamma_f$
- **Frank-van-der-Merwe** (layer by layer) - $\gamma_s > \gamma_i + \gamma_f$
- **Stranski-Krastanov** (layer plus island) - $\gamma_s \approx \gamma_i + \gamma_f$

B) Chemical production methods.

1. ***Chemical reduction***. This is one of the most widely used methods for nanoparticles productions. Chemical synthesized nanoparticles are produced by dissolving the metal salts in solvents, usually in the presence of ligands that have the purpose of passivating the clusters surface, as shown in case of Pd_1Au_{24} $(SC_{12}H_{25})_{18}$ nanoclusters supported on multiwall carbon nanotubes, in Ref. [49]. Subsequently, annealing procedures are employed for the removal of ligands and expose the clusters surface for future applications (e.g nanocatalysis) [49]. A colloidal nanoparticle can be described as having a metallic core (Au, Ag, Pd, Pt) surrounded by a ligand shell (e.g alkylthiols – $CH_3(CH_2)_n$-SH [50]) and thioethers ($CH_3(CH_2)_nS$-$(CH_2)_mCH_3$ [51]. A possible mechanism proposed for the growth of colloidal nanoparticles has been described in Ref. [52] and consists in nucleation, growth and further agglomeration of nanoparticles, in which metal nanoparticles with diameters smaller than 1 nm can be considered ‘seeds’ for the further growth of nanoparticles. A modified seed-mediated growth synthesis of bimetallic AuPd nanoparticles have been obtained in the paper of Ding et al, in Ref [53]. Particles sizes can be controlled with the help of *inverse micelles* (an inverse micelle is a hollow, spherical species, whose inner surface has a high affinity towards metal ions while the hydrocarbon chains interact with the organic solvent). A method for producing AuPd nanoparticles with the inverse micelles method, with various ratios of Au/Pd and with a good degree of control over the size distribution has been reported in the paper of Wu et al. [54].

(a) Chemical co-reduction – in this method, two metallic salts are reduced simultaneously in the presence of a stabilizer (e.g $NaBH_4$, N_2H_4, etc.) to form the corresponding bimetallic nanoparticles:

$$A^+ + B^+ \xrightarrow{NaBH_4} A + B \longrightarrow (AB)_n \tag{1.2}$$

During the reduction process, the metal species with highest redox potential will form the core of the bimetallic nanoparticles by precipitating first. Subsequently, the bimetallic nanoparticle shell will be deposited. However, it has been shown that this method is very versatile in producing both core-shell and random mixing patterns in bimetallic nanoparticles [22, 55-57]. According to Ref. [22], the morphology of the resulting nanoparticle is highly dependent also on the affinity of the stabilizer towards a metal or another. Following this consideration it has been shown that if the stabilizer has a higher degree of affinity towards one of the metallic species in the solution, it is likely that the metal which is more attracted towards the stabilizer will occupy surface positions. If no degree of affinity is preferred between the stabilizers and the metals, then mixed configurations will form. In the paper published by Kuai et al. [58], the authors show that both such morphologies (i.e core-shell and mixed nanoparticles) can be achieved in bimetallic AuPd nanoparticles. This method has been used in to achieve the production of $Au_{core}Pd_{shell}$ nanoparticles, as shown the paper of Ding et al. [53], where the nanoparticles external Pd shell has been subsequently modified in thickness, by adding a larger quantity of metal precursors during the nanoparticles formation.

(b) Successive reduction – this procedure has been found the most suitable in order to ensure homogeneity in the structure of the nanoparticles. Usually, a second metal is grown on the surface of a pre-formed metal nanoparticle seed.

$$\begin{tikzcd}
\boldsymbol{A^+} \arrow[r, "NaBH_4"] & \boldsymbol{A} \arrow[r] & \boldsymbol{A_n} \arrow[rr] & & \boldsymbol{(AB)_n} \\
 & & & \boldsymbol{B} & \\
 & & & \boldsymbol{B^+} \arrow[u] &
\end{tikzcd} \qquad (1.3)$$

Usually, a cluster without passivating ligands will undergo a second reduction step in the presence of salts of the other metal [59]. This deposition method does not always offer a homogenous alloy composition within a nanoparticle, but it is successful in the production of core-shell configurations, as it has been reported in [59]. It is interesting to observe that this method is particularly challenging for the production of $Pd_{core}Au_{shell}$ nanoparticles, due to the different redox potentials of Pd and Au ions ($Au^{3+}/Au = 1.498$ V, $Pd^{2+}/Pd = 0.951$ V) but has been reported by other groups [59]. Lee et al. [60] have shown that well-defined core-shell morphologies of AuPd nanoparticles have been obtained, by first reducing $HAuCl_4$ with sodium citrate to form seeds of Au. A subsequent reduction of

H_2PdCl_4 has been attempted, in the presence of hydroxylamine hydrochloride, onto the pre-existent Au seeds. However, one of the most common problems in production of bimetallic nanoparticles with the successive reduction chemical synthesis include the formation of secondary monometallic nanoparticles, morphologies such as cluster-in cluster nanoparticles or random ally configurations. Weak reducing agents have to be used in order to achieve a controlled reduction of the second metal onto the seed pre-formed of another one, in order to avoid the production of monometallic nanoparticles [22].

2. *Electrochemical synthesis.* Bimetallic nanoparticles of metals such as Mo, Rh or Ru can be generated by electrochemical reduction of their salts at the cathode [61]. Various configurations of bimetallic nanoparticles could be obtained, such as core-shell [62] or alloy configuration [63]. An interesting nanocomposite material based on reduced graphene oxide and AuPd nanoparticles with a 1:1 composition has been obtained in Ref. [64]. In this paper, it has been shown that the production method has lead to a homogeneous dispersion of AuPd nanoparticles, large electroactive surface area as well as a high degree of stability against O_2 reduction.

3. *Radiolysis*. In this production method, the aqueous solution is exposed to γ-rays, which leads to solvated electrons which will then reduce the metal ions [65, 66]. The metals will then further coalesce to form nanoparticles. If the production of bimetallic nanoparticles is desired, when a noble metal is usually involved in the reaction it will be preferentially reduced first, and the formation of various bimetallic nanoparticles morphologies (core-

shell or alloy) is highly dependent on the rate of radiolysis (and subsequently on the γ ray dose) or relative concentration of the two metals, etc.

C) Biological methods for synthesis of bimetallic nanoparticles.

Microbial methods. These are relatively new methods for bimetallic nanoparticles synthesis, in which microorganisms (i.e. bacteria) are employed in the nanoparticles production [67, 68]. The experimental production of bimetallic nanoparticles via microbial synthesis typically require a source of metal (e.g. agents such as $HAuCl_4$). The control of size, shape and composition of bimetallic nanoparticles is made by tuning various parameters such as pH, incubation time, temperature, light intensity etc. [69]. Recent literature reports refer to the production of bimetallic AuPd nanoparticles using *Escherichia coli* and *Desulfovibrio desulfurican* bacteria [70, 71]. Metal precursors ($HAuCl_4$ and $[Pd(NH_3)_4]Cl_2$) are reduced in the presence of H_2 (acting as electron donors) in order to form bimetallic AuPd nanoparticles distributed onto a bacterial cell surface. The Au^{3+} and Pd^{2+} ions are then reduced by the enzyme hydrogenase existing in the microbial periplasmic space [72]. A major advantage of this production method consists in the fact that large quantities of bimetallic nanoparticles or their monometallic counterparts can be produced for industrial applications, with less reducing agents or energy required in the production [41].

1.5. Summary - production methods

This section has shortly described the most commonly employed methods for the producing bimetallic AuPd nanoparticles. The two main approaches, the top-down and the bottom-up approaches imply both physical production methods and chemical synthesis methods. The physical production methods have a high degree of control over the size distribution, homogeneity and substrate coverage for the production of bimetallic nanoparticles. However, methods of production such as cluster beam sources- are more suitable for production of model nanoparticles for applications in nanocatalysis, since the yield is too low and the production methods expensive to implement.

On the other hand, physical vapour deposition methods have been less common in depositing especially the AuPd bimetallic system. Contrary to the cluster beam sources, this method is more suitable in producing larger quantities of nanoparticles for applications in domains such as nanocatalysis. However, as mentioned above, the size distribution is not as narrow as in the case of cluster beam sources, since the formation of nanoparticles is highly dependent on the substrate morphology, temperature, hopping distance, etc. However, we show in Chapter VI that, by carefully tuning the post deposition temperature, a manipulation of nanoparticles morphologies is possible, ranging from mixed to segregated.

The chemical production methods used for the synthesis of bimetallic nanoparticles are versatile for producing larger quantities of nanoparticles for applications in catalysis. However, the main difficulties are arising from the control over the size distribution, avoidance of bi-products (such as the monometallic counterparts of the bimetallic nanoparticles– see the successive reduction chemical synthesis method) and, more importantly, the difficulties arising from the control of kinetic processes involved in the production of bimetallic nanoparticles. Novel chemical production methods, involve the use of passivating ligands ("divide and protect" chemical synthesis methods) have recently become successful in keeping a high degree of control over the bimetallic nanoparticles size distribution [49] and a good control over the clusters morphologies.

One such system has been studied in Chapter V, where ligand un-passivated $Au_{24}Pd_1$ nanoclusters, have been analysed. As described in the paper of Xie et al. [49], single metal doping can be achieved, in tandem with a very narrow size distribution, a robust catalytic activity with respect to the monometallic Au_{25} clusters, as well as high stability towards thermal treatment methods (see Chapter V).

1.6. Characterization of bimetallic nanoparticles

Once the metal nanoparticles have been synthesized, it is very important to fully characterize and understand their structure. Over the years, many methods have been developed for a proper understanding of the nanoparticles structure. In this sub-chapter we will however focus on the main techniques with relevance to this thesis, namely the Scanning Transmission Electron Microscope (STEM) and Energy Dispersive X-ray (EDX) spectroscopy.

1.6.1. Application of (S)TEM and Energy Dispersive X-ray (EDX) spectroscopy techniques for the characterization of AuPd bimetallic systems

(S)TEM is a very powerful technique for the characterization of nanoparticles size, composition and crystalline structure. When an electron beam interacts with a sample, the electrons can be either transmitted, scattered, backscattered or diffracted [73, 74]. TEM uses the transmitted electrons signal in order to form the image of the sample. The transmitted electron beam is dependent on the sample thickness; in case in which the sample thickness is sufficiently small (few nanometers), the transmitted electrons pass through it, without significant energy loss. Since the attenuation of the electrons depends preponderantly on the density and thickness of the sample, the transmitted electron beam forms a two-dimensional image of the sample. (S)TEM is a very powerful tool in discerning the intensity variation related to the difference in atomic numbers in bimetallic nanoparticles (Z-contrast), and, when coupled with other characterization methods such as EDX, it can also offer details regarding chemical composition of nanoparticles.

Although, traditionally, the surface of nanoparticles has been investigated through other microscopy techniques such as Scanning Tunneling Microscope (STM) or Atomic Force Microscope (AFM), these characterization techniques are limited for the case of nanoparticles capped with organic ligands. The advantage of the TEM-based techniques is that they offer an insight on the nanoparticles structure and morphology regardless of the presence of capping ligands [75]. Another important feature of a TEM is that small metallic nanoparticles, with large fluxional character under the electron beam (i.e. structural details of small nanoparticles change between consecutive frames, an effect attributable to thermal fluctuations and/or momentum transfer between finely focused electron beam and the cluster [24]) –can also be imaged, since the electron beam current can be modified accordingly, but on the expense of reducing the signal to noise ratio. This particularity of the TEM has been widely used in the literature, especially in order to study beam-induced nanoparticles structural modifications, elemental mapping and equilibrium state structures [76]. General TEM analysis does not have enough resolution in order to determine the crystallinity of a nanomaterial. However, High Resolution Transmission Electron Microscopy (HR-TEM) can be successfully employed for the characterization, with atomic resolution, of the crystallinity of a sample as well as for providing the information regarding electron diffraction analysis. This approach helps in gaining an insight of the ordering of metal atoms in a nanoparticles or to study, in first instance of defects and dislocations. This approach has been adopted for bimetallic AuPd nanoparticles in the paper of Ding et al. [53], where, via chemical production synthesis, AuPd nanoparticles with core-shell configurations have been produced. The authors have controlled, via careful addition of metal precursors – the thickness of the exterior Pd layer, for which they observed that Shockley partial dislocations start to develop and also established, based on HRTEM analysis, ordered crystallographic phases in the AuPd nanoparticles. HR-TEM/HREM offers resolution down to the Angstrom level and offers valuable information on the structure of nanoparticles at atomic resolution [22, 77].

STEM is another mode of operation of TEM, in which a fine electron probe is raster-scanned across the sample [78]. This imaging technique is known for being particularly powerful for the characterization of bimetallic systems. High-Angle Annular Dark Field (HAADF)-STEM is a widely-used imaging technique [78] employed for the characterization of small and large bimetallic particles. The advantage of this technique consists in the fact that the image intensity is proportional to the atomic number of the nanoparticles through a power relation ($I \sim Z^{\alpha}$), where Z is the atomic number and α is usually taken in the range 1.5-2 [79], in order to reveal the structure of the nanoparticles, based on different electron scattering powers of different chemical elements [78, 80]. In Ref. [81], Mayoral et al. have studied the evolution of bimetallic AuPd nanoparticles under the electron beam, monitoring the diffusion of Pd on the substrate, following the sintering process that took place between Au-rich and Pd-rich nanoparticles (also see Figure 1.6). In Figure 1.6, a clear difference between Au and Pd can be observed, due to the atomic number difference.

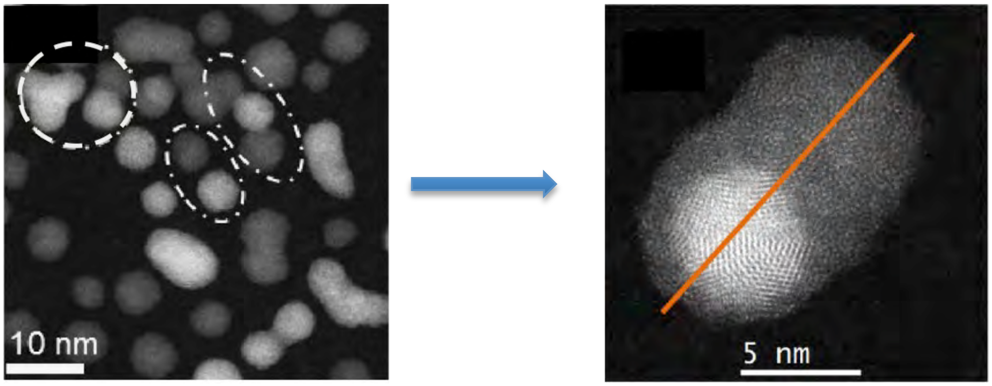

Figure 1.6. A Scanning Transmission Electron Microscope image of the evolution of Au-rich and Pd-rich nanoparticles on the surface of amorphous carbon (left) and the effect of nanoparticles sintering under the electron beam (right). The clear difference between Au and Pd is revealed by the Z-contrast, due to the difference in the atomic numbers of the two elements (Z_{Au}=79, Z_{Pd}=46). From Ref. [81]

Various other studies [23, 82, 83] have focused on the experimental characterization of bimetallic AuPd nanoparticles by combining HAADF-STEM techniques with other complementary analysis methods such as Energy Dispersive X-ray (EDX) Spectroscopy or Electron Energy Loss Spectroscopy (EELS). This approach can become extremely powerful for determining the nanoparticles compositional information in tandem with structural information.

An example of such study has been published by Zhang et al. [84], where the compositional effects in bimetallic AuPd nanoparticles have been observed experimentally using a combination of HAADF-STEM and EELS. Here, the authors have observed that, using a galvanic replacement method, the top-corners of the Pd_{147} nanoparticles can be successfully replaced with Au atoms. The Au-decorated Pd clusters exhibit an enhanced selectivity towards the oxidation of glucose, whereas the activity of pure Pd or Au nanoparticles is much less significant. In Ref. [84], EELS has been used as a complementary analysis method in order to confirm the location of the low-coordinated Au atoms on the surface of Pd_{147} nanoclusters (see Figure 1.7).

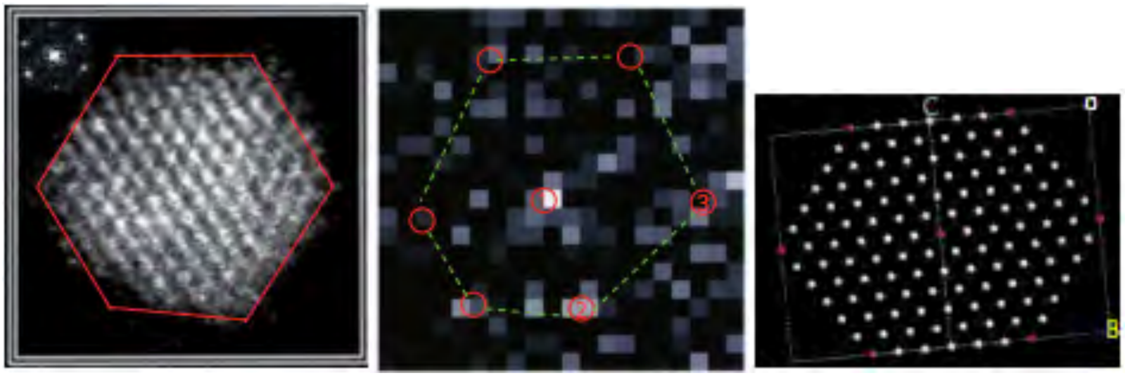

Figure 1.7 HAADF-STEM analysis (left) and EELS mapping (centre), together with the proposed structural model (right) for the Au-decorated Pd_{147} nanoclusters used for the glucose oxidation process. Here, HAADF-STEM information and EELS mapping have been used for a better understanding of the structural arrangement of atoms in AuPd nanoclusters. Taken from Ref. [84].

As mentioned above, the EDX technique, combined with HRTEM/STEM is one of the most useful techniques for compositional determination of bimetallic systems [85, 86]. EDX is an elemental mapping/quantitative analysis tool in which the incident beam excites an electron from the shell while creating an electron hole. An electron from an outer, higher-energy shell will then fill the hole. The difference in energy between the higher-energy shell and the lower-energy shell is released in form of X-rays [86]. The wavelengths of the X-rays emitted from a specimen is a characteristic of the difference in energy between the two shells and therefore of the atomic structure of the element from which they were emitted. This allows the elemental mapping of the specimen. Tiruvalam et al. [83] has, for example, coupled the HAADF-STEM analysis with EDX elemental mapping in order to identify the composition of AuPd bimetallic nanoparticles involved in the oxidation of benzyl alcohol.

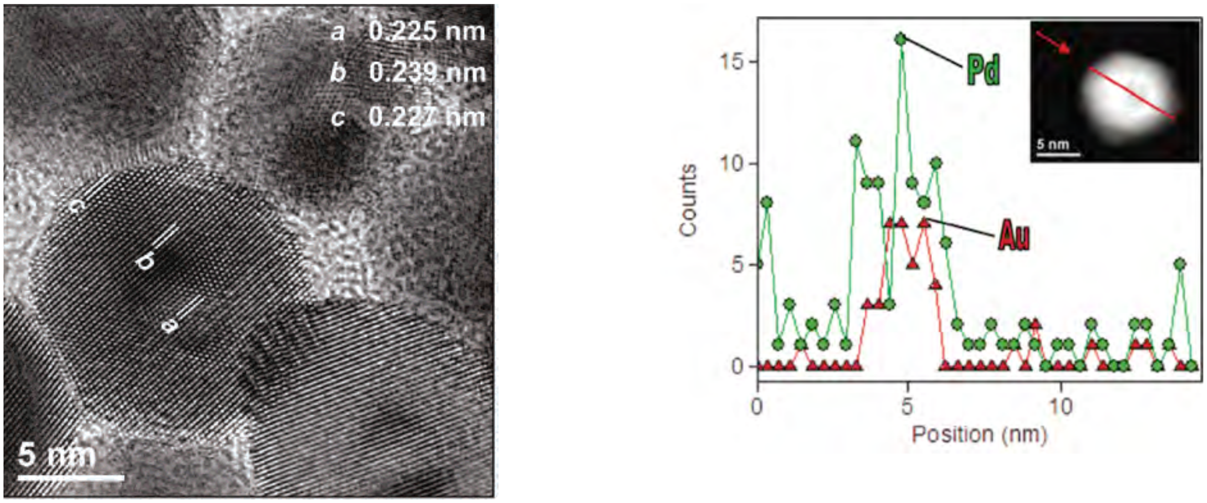

Figure 1.8. (left) TEM image of three-layer AuPd nanoparticles produced via chemical synthesis methods; (right) EDX line profile of a three layer AuPd nanoparticle. Taken from Ref. [25].

Mayoral et al. [81] have used complementary HAADF-STEM/EDX analysis in order to confirm the nature of the diffused Pd layer on the surface of amorphous carbon, following a sintering experiment under the electron beam which involved initial Pd-rich and Au-rich bimetallic nanoparticles. The distribution of elements in bimetallic nanoparticles with three-layer morphologies has been implemented in the paper of Ferrer et al. [25]. In this paper, the authors have complemented the TEM analysis in order to confirm the elemental composition of colloidal nanoparticles produced by successive reduction or metal precursors (see Figure 1.8).

1.7. Research objectives

The objective of this work has been to study the structure and energetics of bimetallic AuPd nanoparticles by means of a *combination of theoretical and experimental analysis*.

The *first system*, the 98-atom AuPd clusters has been *characterized theoretically* in order to establish their structure and energetics. The study has had the purpose of understanding better the segregation effects (the most stable cluster structures) in small AuPd bimetallic clusters, since they can be considered “seeds” for the growth of larger nanoparticles. In this study, we have shown that a combined approach based on the use of empirical potentials (the Gupta potential) and DFT calculations and employing Genetic Algorithms and Basin Hopping Monte Carlo search methods is a powerful tool for the identification of low-energy structural motifs and segregation patterns in bimetallic nanoparticles up to 100 atoms.

The *second system* that has been studied is $Au_{24}Pd_1$ bimetallic nanoclusters supported on multiwall carbon nanotubes. *Experimentally*, the HAADF-STEM imaging technique has been employed for the determination of structure and morphology of two systems: $Au_{24}Pd_1$

nanoparticles supported on Multiwall Carbon Nanotubes and evaporated AuPd nanoparticles. For the first system, the interest stems from important applications of the AuPd catalyst in the aerobic oxidation of benzyl alcohol. In a paper previously published by Xie et al. [49], the authors have postulated that an enhanced catalytic activity, of more than 54%, has been observed for the case of single Pd doped Au_{25} nanoclusters than for the case of their monometallic counterparts. In this thesis we have employed HAADF-STEM analysis in order to establish the morphology of the bimetallic system, in order to determine the number of atoms in the system by using single Au atoms as mass standards, as well as to determine the shape population of the bimetallic clusters. Moreover, the effect of the electron beam over the nanoparticles morphology has been studied for high and low electron dose. The study has been focused on both ligand protected and un-protected $Au_{24}Pd_1$ system. *Theoretically,* the low-energy structures of free/unsupported $Au_{24}Pd_1$ nanoclusters have been determined by performing a direct search at the DFT level using the Basin Hopping Monte Carlo Algorithm. The study is complementing our experimental analysis by identifying the location of the Pd dopant in the clusters. Further analysis has been focused on the determination of the charge transfer and establishing the role of the Pd dopant as a direct reaction site or as an indirect promoter for the surrounding Au cage.

The *third system*, the evaporated AuPd bimetallic nanoparticles have been studied *experimentally*. HAADF-STEM has been employed for the structural characterization and for the analysis of the morphology evolution for the nanoparticles following annealing treatments at 500 K for 60, 120 and 180 minutes respectively. The study has shown that, by carefully tuning the post-deposition conditions, a structural evolution of the evaporated nanoparticles can be obtained, from mixed to segregated. EDX has been used complementary to the HAADF-STEM system, in order to characterize the composition our clusters. The project has aimed to bring a contribution to a better understanding of the bimetallic AuPd system by combining the two approaches with potential further applications in domains such as nanocatalysis.

1.8. Conclusions

This chapter has reviewed bimetallic nanoparticles production and specific characterization methods respectively, with special focus on the production/characterization of bimetallic AuPd systems. The chapter has also been focused on a short description of factors that are influencing the segregation, mixing and ordering patterns in bimetallic nanoparticles and what constitutes the difficulty of characterizing theoretically these systems (the presence of homotops). The following chapters will be focused on the main methodologies for characterizing bimetallic systems, from a theoretical and experimental point of view. A short description of Gupta potentials and basics of Density Functional Theory (DFT) will be made, as they constitute the basics of theoretical characterization used in this thesis. From an experimental point of view, the principle if image formation in STEM will be described shortly, as it is the main tool used for the experimental characterization of the bimetallic AuPd systems. The thesis will then focus on the main results obtained for the characterization of three bimetallic AuPd systems: the 98-atom AuPd nanoparticle (theoretical characterization), the 25-atom AuPd nanoparticles (hybrid theoretical and experimental characterization) and finally, the experimental characterization of AuPd nanoparticles obtained via PVD and the influence of annealing temperature and time on the morphology and structure of nanoparticles.

Bibliography

---

[22] Ferrando, R., Jelinek J., Johnston, R. L. J., *Chem. Rev.*, 3, 845, **2008**.

[23] Ferrer, D., Blom, D. A., Allard, . F., Mejia, S., Perez-Tijerina, E., Jose-Yacaman, M. J., *J. Mater. Chem.*, 18, 2442, **2008**.

[1] Johnston, R. L, Wilcoxon, J. P. (eds), *Frontiers of nanoscience*, Elsevier, Oxford, **2012**.

[2] Jellinek, J.; Krissinel, E. B. (eds), *Theory of Atomic and Molecular Clusters*, Springer, Berlin, **1999**.

[3] Hosseini, M., Barakat, T., Cousin, R., Aboukais, A., Su, B. L., De Weireld, G., Siffert, S., *Appl. Catal. B, Environmental*, 111, 218, **2012**.

[4] Lopez-Sanchez, J. A., Dimitratos, N., Glanville, N., Kesavan, L., Hammond, C., Edwards, J., Carley, A., Kiely, C., Hutchins, G. J., *Appl. Catal. A: General*, 391, 400, **2011**.

[5] Chen, H., Li, Y., Zhang, F., Zhang, G., Fan, X., *J. Mater. Chem.*, 21, 17658, **2011**.

[6] Zhang, H., Watanabe, T., Okumura, M., Haruta, M., Toshima, N., *Nature Materials*, 3143, 1, **2011**.

[7] Kan, C., Cai, W., Li, C., Zhang, L., Hofmeister, H., *J. Phys. D: Appl. Phys.*, 36, 1609, **2003**.

[8] Kreibig., U., Vollmer, M., *Optical Properties of Metal Clusters*, Springer, Berlin, **1995**.

[9] Mayoral, A., Mejia-Rosales, S., Mariscal, M. M., Perez-Tijerina, E., Jose-Yacaman, M., *Nanoscale*, 2, 2647, **2010**.

[10] Paz-Borbon, L. O., *Computational analysis of transition metal nanoalloys*, Springer, Berlin, **2011**.

[11] Demirci, U. B., *J. Power Sources*, 173, 11, **2007**.

[12] Antolini, E., *Mater. Chem. Phys.*, 78, 563, **2003**.

---

[13] Bouwmann, P. J., Dmowski, W., Stanley, J., Cotton, G. B., Swider-Lyons, K. E., *J. Electrochem. Soc*., 151, A1989, **2004**.

[14] Hamnett, A., *Catal. Today*, 38, 445, **1997**.

[15] Cuenya, B. R., *Thin Solid Films*, 518, 3127, **2010**.

[16] Naitabdi, A., Roldan-Cuenya, B., *App. Phys. Lett*., 91, 113110, **2008**.

[17] Rolison, D. R., Hagans, P. L., Swider, K. E., Long, J. W., *Langmuir*, 15, 774, **1999**.

[18] Andrews, M. P., O'Brien, S. C., *J. Phys. Chem*., 96, 8233, **1992**.

[19] Johnston R. L., *Dalton Trans*., 23, 4193, **2003**.

[20] Apra, E., Ferrando, R., Fortunelli, A., *Phys. Rev. B*, 73, 205414, **2006**.

[21] Tiruvalam, R. C., Pritchard, J. C., Dimitratos, N., Lopez-Sanchez, J. A., Edwards, J. K., Carley, A. F., Hutchins, G. J., Kiely, C. J., *Faraday Discuss*., 152, 63, **2011**.

[24] Ismail, R., Johnston, R. L., *Phys. Chem. Chem. Phys*., 12, 8607, **2010**.

[25] Ferrer, D., Torres-Castro, A., Gao, X., Sepulveda-Guzman, S., Ortiz-Mendez, U., Jose-Yacaman, M. J., *Nano Lett.*, 7, 1701, **2007**.

[26] Malola, S., Hakkinen, H., *J. Phys. Chem. Lett*., 2, 2316, **2011**.

[27] Krissinel, E. B., Jellinek, J., *Int. J. Quant. Chem*., 62, 185, **1997**.

[28] Rossi, G., Ferrando, R. in *Nanomaterials: Design and Simulation,* Balbuena, P. B., Seminario, J. M. (eds), Elsevier, Amsterdam, **2007**.

[29] Green, M., O'Brien, P., *Chem. Commun*, 123, 183, **2000**.

[30] Akita, T., Hiroki, T., Tanaka, S., Kojima, T., Kohayama, M., Iwase, A., Hori, F., *Catal. Today*, 131, 90, **2003**.

[31] Tran, N. T., Powell, D. R., Dahl, L. F., *Dalton Trans*., 2, 217, **2004**.

---

[32] Mariscal, M. M., Oldani, N. A., Dassie, S. A., Leiva, E. P., *Faraday Discuss*., 138, 353, **2008**.

[33] Perez-Tijerina, E., Mejia-Rosales, S., Inada, H., Jose-Yacaman, M., *J. Phys. Chem. C*, 114, 6999, **2010**.

[34] Pratontep, S., Carroll, S. J., Xirouchaki C., Sterun, M., Palmer, R. E., *Rev. Sci. Instrum*, 76, 045103, **2005**.

[35] Bouwen, W., Thoen, P., Vanhoutte, F., Bouckaert, S., Despa, F., Weidele, H., Silverans, R., Lievens, P., *Rev. Sci. Instrum*., 71, 54, **2000**.

[36] Yin, F., Wang, Z. W., Palmer, R. E., *J. Am. Chem. Soc.*, 133, 10325, **2011**.

[37] Palmer, R. E., Leung, C., *Trends Biotechnol.*, 25, 48, **2007**.

[38] Shreemoyee, G., Mukul, K., Soumendu, D., Biplab, S., Abhijit, M., *Phys. Rev. B*., 78, 014402, **2008**.

[39] Yang, Y., Saoud, K. M., Abdelsayed, V., Glaspell, G., Deevi, S., El-Shall, M. S., *Catal. Commun*., 7, 281, **2006**.

[40] Wegner, K., Piseri, P., Tafreshi, H. V., Milani, P., *J. Phys. D.: Appl. Phys.*, 39, R439, **2006**.

[41] Sattler, K. D. (eds.), *Handbook of nanophysics: clusters and fullerenes*, CRC Press, Boca Raton, **2010**.

[42] Saito, N., Koyama, K., Tanimoto, M., *Appl. Surf. Sci*., 169, 380, **2001**.

[43] Wagner, R. L., Vann, W. D., Castlemann, A. W., *Rev Sci. Instrum*., 68, 3010, **1997**.

[44] Nonose, S., Sone, Y., Onodera, K., Suodo, S., Kaya, K., *J. Phys. Chem*., 94, 2774, **1990**.

[45] Gillen, G., King, L., Freibaum, B., Lareau, R., Bennett, J., Chmara, F., *J. Vac. Sci. Tech*., 19, 568, **2001**.

---

[46] Siekmann, H. R., Luder, C., Faehrmann, J., Lutz, H. O., Meiwes-Broer, K. H., *Zietschrift fur Physil D Atoms, Molecules and clusters*, 20, 417, **1991**.

[47] Venables, J., *Introduction to surface and thin film processes*, Cambridge University Press., Cambridge, **2000**.

[48] Nagasawa, A., matsuo, Y., Kakinoki, J., *J. Phys. Soc. Jpn*., 20, 1881, **1965**.

[49] Xie, S., Tsunoyama, H., Kurashige, W., Negishi, Y., Tsukuda, T., *ACS Catal.*, 2, 1519, **2012**.

[50] Landman, U., Luedtke, W. D., *Faraday Discuss*., 125, 1, **2004**.

[51] Hakkinen, H., *Nature Chemistry*, 4, 443, **2012**.

[52] Turkevich, J., Stevenson, P. C., Hiller, J., *Discuss. Faraday Soc*., 11, 55, **1971**.

[53] Ding, Y., Fan, F., Tian, Z., Wang, Z. L., *J. Am. Chem. Soc*., 132, 12480, **2010**.

[54] Wu, M. L., Chen, D. H., Huang, T., C., *Langmuir*, 17, 3877, **2001**.

[55] Dash, P., Bond, T., Fowler, C., Hou, W., Coombs, N., Scott, R. W. J., *J. Phys. Chem. C*., 113, 12719, **2009**.

[56] Toshima, N., Yonezawa, T., *New J. Chem*., 22, 1179, **1998**.

[57] Hou, W., Dehm, N. A., Scott, R. W. J., *J. Catal.*, 253, 22, **2008**.

[58] Kuai, L., Yu, X., Wang, S., Sang, Y., Geng, B., *Langmuir*, 28, 7168, **2012**.

[59] Scott, R. W. J., Wilson, O. M., Oh, S. K., Kenik, E. A., Krooks, R. M., *J. Am. Chem. Soc.*, 126, 15583, **2004**.

[60] Lee, A. F., Baddeley, C. J., Hardcare, C., Ormerod, R. M., Lambert, R. M., Schmid, G., West, H., *J. Phys. Chem.* , 99, 6096, **1995**.

[61] Bonnemann, H., Richards, R. M., *Eur. J. Inorg. Chem*., 137, 2455, **2001**.

[62] Kolb, U., Quaiser, S. A., Winter, M., Reetz, M. T., *Chem. Mater*., 8, 1889, **1996**.

[63] Jitianu, M., Kleisinger, R., Lopez, M., Goia D. V., *J. Mater. Electrochem. Sys*., 10. 67, **2007**.

[64] Yang, J., Deng, S., Lei, J., Ju, H., Gunasekaran, S., *Biosens. and Bioelectron*., 29, 159, **2011**.

[65] Belloni, J., Mostafavi, M., Remita, H., Marignier, J. L., Delcourt, M. O., *New. J. Chem*., 22, 1239, **1998**.

[66] Braunstein, P., Oro, L. A., Rauhtby, P. R. (eds.), *Metal clusters in chemistry*, Wiley-VCH: Weinheim, **1999**.

[67] Tran, D. T., PhD thesis, University of Birmingham, **2010**.

[68] Sarikaya, M., Tamerler, C., Jen, A. K. Y., Schulten, K., Baneyx, F., *Nat. Mater*., 2, 577, 2003.

[69] Klaus, T., Joerger, R., Olsson, E., Granqvist, C., *Proc. Natl. Acad. Sci. USA*, 96, 13611, **1999**.

[70] Redwood, M. D., Deplanche, K., Baxter-Plant, V. S., Macaskie, L. E., *Biotech. Bioeng*., 99, 1405, **2008**.

[71] Deplanche, K., Woods, R. D., Mikheenko, I. P., Sockett, R. E., Macaskie, L. E., *Biotech. Bioeng*., 101, 873, **2008**.

[72] Konishi, Y., Tsukiyama, T., Tachimi, T., Saitoh, N., Nomura, T., Nagamine, S., *Electrochem. Acta*, 53, 186, **2007**.

[73] Frenkel, A. I., Hills, C. W., Nuzzo, R. G., *J. Phys. Chem. B*, 105, 12689, **2001**.

[74] Williams, D. B., Carter, B. C., *Transmission Electron Microscopy*, Plenum Press, New York, **1996.**

[75] Wang, Z. L., *J. Phys. Chem. B*, 104, 1153, **2000**.

[76] Koga, K., Sugawara, K., *Surf. Sci.*, 529, 23, **2003**.

[77] Pauwels, B., Van Tendeloo, G., Zhurkin, E., Hou, M., Verschoren, G., Theil Kuhn, L., Bouwen, W., Lievens, P., *Phys. Rev. B*, 63, 165406, **2001**.

[78] Reimer, L., *Transmission Electron Microscopy*, 2nd edition, Springer, Berlin, **2008**.

[79] Young, N. P., Li, Z. Y., Chen, Y., Palomba, S., Di Vece, M., Palmer, R. E., *Phys. Rev. Lett.*, 101, 246103, **2008**.

[80] Mariscal, M. M., Mayoral, A., Olmos-Asar, J. A., Magen, C., Mejia-Rosales S., Perez-Tijerina, Jose-Yacaman, M, *Nanoscale*, 3, 5013, **2011**.

[81] Mayoral, A., Deepak, F. L., Esparza, R., Casillas, G., Magen, C., Perez-Tijerina, E., Jose-Yacaman, M., *Micron*, 43, 557, **2012**.

[82] Mariscal, M. M., Mayoral, A., Olmos-Asar, J., A., Magen, C., Mejia-Rosales, S., Perez-Tijerina, E., Jose-Yacaman, M., *Nanoscale*, 3, 5013, **2011**.

[83] Tiruvalam, R. C., Pritchard, J. C., Dimitratos, N., Lopez-Sanchez, J. A., Edwards, J. K., Carley, A. F. , Hutchins, G. J., Kiely, C. J., *Faraday Discuss.*, 152, 63, **2011**.

[84] Zhang, H., Watanabe, T., Okumura, M., Haruta, M., Toshima, N., *Nature Materials*, 3143, 1, **2011**.

[85] Schmid, G., Lehnert, A., Malm, J. O., Bovin, J. O., *Angew. Chem. Int. Ed.*, 30, 874, **1991**.

[86] Herzing, A. A., Watanabe, M., Edwards, J. K., Conte, M., Tang, Z. R. Hutchins, G. J., Kiely, C. J., *Faraday Discuss.*, 138, 337, **2008**.

Chapter II

Theoretical investigation of bimetallic nanoparticles: Empirical potentials and Density Functional Theory

2.1. Overview

The importance of theoretical characterization of bimetallic nanoparticles can be understood in terms of better rationalizing their activity in the field of optics [1], catalysis, medicine [2] etc. This can be based either on first principle approaches (different quantum chemistry techniques, density functional theory (DFT) and hybrid methodologies), based on models (e.g. jellium model, tight-binding theory [2,3]) or fitted semi-empirical potentials [4, 5]. Regardless of the analysis technique involved in these studies, the main purpose is to identify, for a given cluster size and composition – the location of the global mimimum (GM) [5], which corresponds to the structures with the lowest potential energy.

Identifying the GM clusters for monometallic nanoparticles is not a trivial task, as the number of minima increases exponentially with increasing the cluster size. The problem becomes even more difficult when bimetallic nanoclusters are involved, due to the existence of "*homotops*" [2]. Although a number of literature reports have been previously published regarding the theoretical analysis of bimetallic AuPd nanoclusters, the size range is often limited to less than 100-atom clusters [6-9] due to computational limitations.

In this chapter, theoretical approaches used in this thesis for modeling bimetallic nanoparticles will be described. Empirical Gupta potentials and Density Functional Theory (DFT) will be treated briefly.

2.2. Exploring Potential Energy Surfaces (PES)

As mentioned in Chapter I, the identification of the GM structure of bimetallic nanoparticles is a very difficult task, as the properties of each system are dependent on the elemental composition and size [8]. Various search techniques have been developed in order to identify, for a given size and composition, the location of the GM. A nanoparticle can have multiple higher energy structural states (*local minima* [3]) aside from GM. The potential energy surface (PES) of a nanoparticle is represented in atomic coordinates [8] having $3N-6$ dimensions, where N represents the number of atoms in the system ($3N$ is the number of degrees of freedom). The forces are obtained as derivatives of energy (V) with respect to atomic positions (R) [10]:

$$F = -\frac{\partial V}{\partial R} \tag{2.1}$$

As shown in Ref. [10], on a PES, for local minima, the gradient of the potential energy is zero ($\nabla V_{cluster} = 0$) and the second derivatives (all curvatures) are positive, any displacement leading to higher energy cluster configurations. The lowest energy configuration is called the global minimum [10] (see schematic representation in Figure 2.1).

2.2.1. Global topology of the PES

The shape of a PES is influenced by the placement/ordering of the local minima and their connectivity through transition states [11]. There are several modalities to describe the topology of an energy surface. For example, in Ref. [12], one way is to consider a sequence of local minima, which are inter-connected by transition states, for which the energy of the minima monotonically decreases. Therefore, monotonic sequences that would lead to the same minimum form an energy funnel [11].

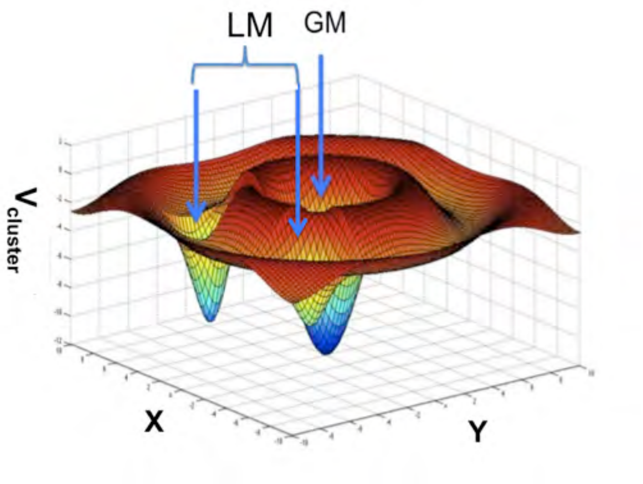

Figure 2.1. A schematic representation of a potential energy surface (PES) of a cluster. In this schematic representation, the potential energy surface has two local minima (LM) and a global minimum (GM).

When systems have only one funnel converging towards the GM, they are called single funnel systems. Systems with multiple sequence basins are called multi-funnel systems (Figure

2.2) [10, 11]. As the PES is explored, once in the "wrong" funnel, a system must overcome several energy barriers in order to reach the GM.

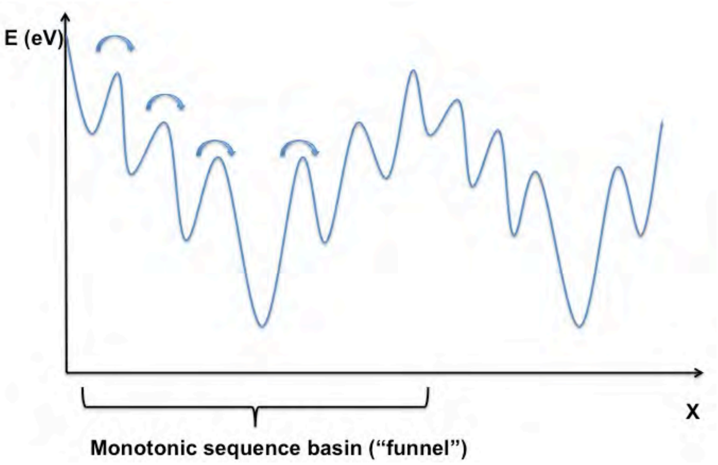

Figure 2.2. Schematic representation of a multiple-funnel PES with a monotonic sequence basin. From Ref. [11].

2.2.2. Genetic Algorithms

Determining nanoparticles structures requires identification of the LM as well as, more importantly, the GM configuration. Energetically higher-lying (metastable isomers) are also important to identify, as they may be observed experimentally due to finite temperature or kinetic effects [5,11,13].

In order to identify all isomers, particularly the GM, a search algorithm is used, in order to "scan" the environment and also to sample the PES. A modality to do this is by using genetic algorithms (GAs) [2]. The name of these algorithms comes from the Darwinistic principle of the survival of the fittest [5]. GAs were developed in 1970's by John Holland [14] and further implemented for the optimization problems in areas such as computational chemistry [5] or biomedical engineering [15], etc. GAs are based on the use of operators of crossover, mutation and natural selection [5]. In this thesis, the Birmingham Cluster Genetic Algorithm (BCGA) [5] has been employed to locate the GM for the bimetallic AuPd clusters, and we have used the Gupta empirical potential in order to model the interatomic interactions, as described below.

The search begins using an initial population of nanoparticles. Various operations are further applied to the initial population (e.g. mutation, crossover, natural selection) in order to identify the most stable nanoparticle configurations [16]. The *initial population* is a set of randomly generated clusters. Each nanoparticle is considered as an individual and the Cartesian coordinates are generated within a volume proportional to the number of atoms in a cluster [8, 17]. The potential energy of the nanoparticle is a function of the Cartesian coordinates. Furthermore, the potential energy will be minimized to the nearest local minimum [5, 18].

A *fitness value* is allocated for every member of the population in order to establish its relative stability. For the GA algorithm used in our work, the highest fitness value is allocated to the lowest energy nanoparticle whereas the lowest fitness value is allocated to the higher energy nanoparticle [5].

In the BCGA, the potential energy of a certain cluster, V_i, is re-scaled with respect to the highest and lowest-fitness clusters in the corresponding population, an operation which is performed with the help of a probabilistic factor ρ:

$$\rho = \frac{V_i - V_{\min}}{V_{\max} - V_{\min}} \tag{2.2}$$

In equation 2.2, V_{min} is the potential energy associated with the lowest-energy cluster, and V_{max} is associated with the highest energy cluster [5]. According to Ref. [5], in BCGA, a fitness function, f_i, is used in order to determine the individuals for the next cluster generation. The fitness value is a randomly generated number between 0 and 1 ($f_i >$ Rnd [0,1]).

The fitness value depends on the probabilistic factor, ρ:

$$f_i = \frac{1}{2}\left[1 - \tanh\left(2\rho - 1\right)\right] \tag{2.3}$$

Individuals will be selected for crossover based on the fitness value. There are various methodologies to perform this: roulette-wheel and tournament selection. In the latter case, a number of strings are randomly selected from the population; the two-highest fitness strings are then selected [5]. For the case of roulette wheel selection, a slot is assigned to each member of the population [5, 16]. Based on the fitness value, each slot has a certain width (see Figure 2.3).

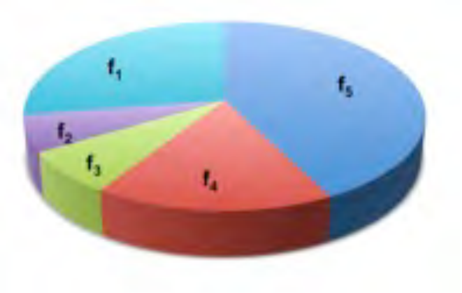

Figure 2.3. Schematic representation of the roulette wheel selection method employed in the BCGA. A fitness value, f_i, is assigned to each individual in the population. The probability of selecting the individual will be corresponding to its fitness value (i.e. to the width of each slot in the roulette wheel selection method). From Ref. [5].

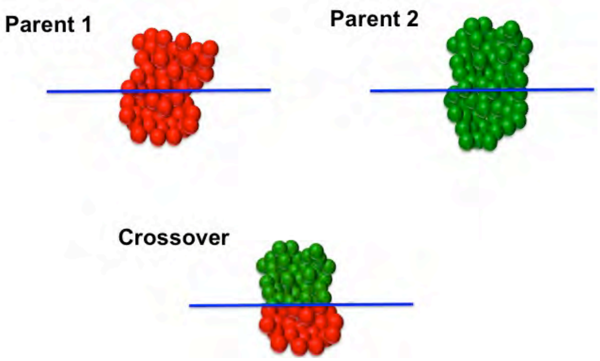

Figure 2.4. Schematic representation of the BCGA crossover operator. Adapted after Ref. [8].

The *crossover operator* involves the use of information from two (or more than two parents) in order to generate an offspring [19]. In BCGA, a 1-point weighted crossover is used, where the cut position is chosen based on the fitness value of parents [5, 8]. The algorithm slices two parent nanoparticles and unifies complementary parts; more atoms are usually chosen from the parent whose fitness value is higher (Figure 2.4) [5].

The *mutation operator* is responsible for introducing new genetic material in the new population [5] (Figure 2.5).

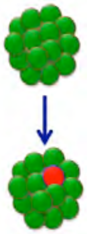

Figure 2.5. The mutation operator in BCGA. This operator introduces new genetic material in the newly generated cluster population. From Ref. [8].

The mutation operator is introduced to avoid stagnation at a local minimum and also to enhance diversity [20]. Various mutation schemes have been implemented in BCGA [5]:

- *Replacement* – This operator is used to remove one existing nanoparticle from the population and replace it with a new one, randomly generated in a similar manner in which the "parent" cluster has been generated.

- *Rotation/twisting* – This operator is used in order to rotate with a random angle the atomic coordinate of the top half of the cluster with respect to the bottom half [8].

- *Exchange* – According to Ref. [8], this operator is used in order to exchange approximately a third of the *A* types of atoms with *B* atoms in a cluster, without changing the original coordinates in the cluster. This operator is mainly used in algorithms for optimizing bimetallic nanoclusters.

- *Displacement* – This mutation operator is replacing the coordinates of a certain number of atoms in a cluster with new coordinates generated within an interval, across their original positions.

In BCGA, the selection criterion is applied to parents, offsprings and mutants respectively, selected to "survive" in the next generation. The selection process is based on the fitness value. It is possible for example, to either accept all mutant structures, or not to accept the parents for next generation or to keep only individuals with the highest value of the fitness ("elitist" selection) [5, 8].

All the operators described above (crossover, mutation, selection) are constantly repeated for a certain number of generations. This process is repeated until it is considered that the optimum solution has been achieved (the convergence criterion is met when, for a number of generations, the potential energy of the nanoparticles is no longer changed).

In this thesis, after identifying the location of the putative GM, the search is refined, by applying the Basin Hopping Monte Carlo (BHMC) algorithm [21]. A short description of the algorithm is given below.

2.2.3. The Basin Hopping Monte Carlo (BHMC) algorithm

For the case of large size bimetallic nanoparticles (~100 atoms), the BHMC algorithm is usually performed in order to refine the search for the GM configuration and optimize the chemical ordering (as shown in Chapter IV, for the case of 98-atom AuPd nanoclusters). Moreover, in this thesis, for the 25-atom AuPd nanoclusters, the BHMC algorithm has been coupled with DFT in order to identify the GM composition.

As described in Ref. [21], the BHMC starts from a random nanoparticle configuration and explores the PES by applying various movements in order to modify the cluster initial geometry. The moves employed can be either “atom-exchange” moves, in which the atom positions are inter-changed, or “shake” moves, in which the cluster atomic coordinates are modified in three Cartesian coordinates [10]. A schematic of the algorithm is shown in Figure 2.6. In the BHMC algorithm the PES is transformed into a step function [21]. In this approach, each point of the configurational space has associated the energy of its nearest local minimum [21]. In Figure 2.6, it is shown a schematic representation of path from A to F explored by the algorithm. According to Ref. [21], if A is considered to be the starting point, the algorithm locally minimizes the energy of the nanoparticle to reach configuration B. Further atom exchange/shake moves are then applied to the cluster resulting in configuration C, followed by a local minimization of its energy in order to reach configuration D. The move from B to D will be accepted, as the potential energy of the latter point is lower. The next structure modification applied to D gives the configuration E that is locally minimized to configuration F. The latter is the GM. The rate of efficiency for BHMC is high, comparable to GAs [21].

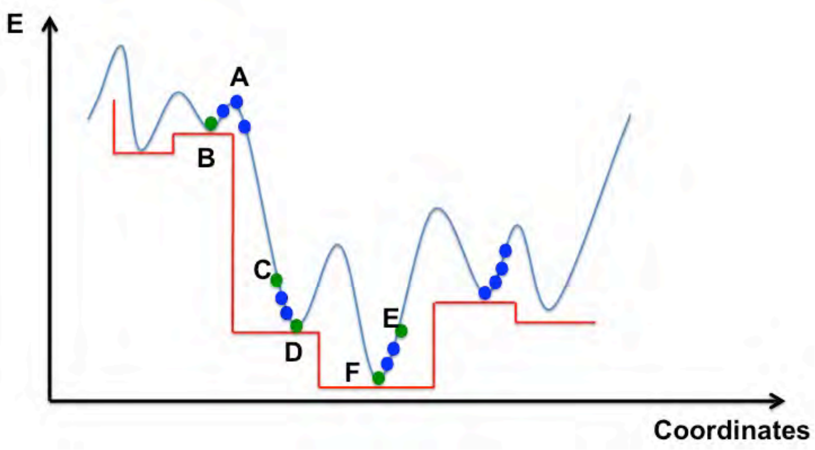

Figure 2.6. Schematic representation of the BHMC algorithm. The BHMC starts from an initial cluster configuration and applies various operators on the atoms of the cluster (“exchange”, “shake”) in order to minimize the total energy of the cluster. Adapted after [21]. See text for the meaning of A, B, C, D, E and F.

During the BHMC optimization, the parameter that plays an important role in a move’s acceptance probability is the fictitious temperature parameter (the k_BT factor, where k_B is the Boltzmann’s constant and T is the temperature). The value of this parameter is chosen as low as possible. The lower the value of the factor $k_B T$, the more appropriate is its choice for performing searches in a PES deep energy funnels [8]. If several funnels are localized in the PES, the GM can be localized by applying BHMC, if the starting point of the algorithm is a nanoparticle localized at a composition close to the GM structure [11]. It has been previously found that the GA approach may not be able to identify from start the most favorable chemical ordering [22]. However, the optimization of the chemical ordering can be performed efficiently by coupling the GA with BHMC algorithm [23]. This justifies our combined search method of first identifying the basin where the GM may be located and then refining the search by performing atom exchange moves on the lowest-energy structures.

2.2.4. Shell Optimization Routine

The Shell Optimization routine [8] has been employed in this work in Chapter IV in order to generate a special type of cluster, the Leary Tetrahedron (LT) [24]. This method is usually applied for high-symmetry poly-icosahedron clusters [8]. As shown in Ref. [8], a reduction in the search space is obtained if the atomic shells (symmetry-equivalent atoms) are set to be of the same chemical species. For a given structure, this reduces the number of permutational isomers to 2^S, where S is the number of atomic shells. The Leary Tetrahedron is a high-symmetry cluster, and the number of shells is S=9 [8]. Therefore, in total 512 isomers are obtained, with the shell sequence of 4:12:12:12:4:6:12:12:24 atoms, in the order of increasing distance from the cluster centre. An example of the Leary Tetrahedron is shown in Figure 2.7.

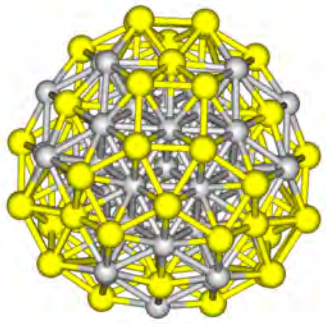

Figure 2.7. The high symmetry Leary Tetrahedron structure found for a composition of $Pd_{52}Au_{46}$ for the 98-atom AuPd clusters.

2.2.5. Empirical approaches: The Gupta potential

Exploring the PES of a cluster can be made either when the cluster bonding is calculated *empirically* or with *ab-initio* methods. *Ab-initio* procedures imply the use of quantum mechanics principles by applying many-body quantum theories such as Density Functional Theory (DFT) [25]. Although DFT is a very accurate method for the determination of clusters geometries and energetics, it is computationally expensive and difficult to implement when the dimensions of the system exceed 100 atoms [26, 27]. Therefore, a full DFT based global optimization is quite difficult to implement and is a very complex issue, being limited to small size bimetallic clusters [3].

For large systems (e.g. the 98-atom AuPd system described in Chapter IV), it is important to complement *ab-initio* calculation methods with *non-ab-initio* ones, based on atomistic empirical potentials in order to pre-select which are the lowest energy clusters. Non *ab-initio* methods are based on the use of atomistic potentials (e.g. Gupta) in which the parameters involved are fitted to experimental data.

The Gupta potential is based on the second moment approximation of tight binding theory [28, 29]. The Gupta potential is written as summation over all the N atoms of a repulsive (V^r) and an attractive many-body term (V^m):

$$V_{clus} = \sum_{i}^{N} \left\{ V^r(i) - V^m(i) \right\} \tag{2.4}$$

where the repulsive term is:

$$V^r(i) = A(a,b) \sum_{j \neq i}^{N} \exp\left(-p(a,b) \left(\frac{r_{ij}}{r_0(a,b)} - 1 \right) \right) \tag{2.5}$$

and the attractive term is:

$$V^m(i) = \xi(a,b) \sqrt{ \sum_{j \neq i}^{N} \exp\left(-2q(a,b) \left(\frac{r_{ij}}{r_0(a,b)} - 1 \right) \right) } \tag{2.6}$$

where a and b are the element types, $A(a,b)$ is the cohesive energy, $\xi(a,b)$ is the many-body energy scaling parameter, $p(a,b)$ is the repulsive interaction range, $q(a,b)$ is the attractive interaction range, r_{ij} is the interatomic distance, and $r_0(a,b)$ is the equilibrium nearest-neighbor distance (NND) [5]. The values of the Gupta parameters have previously been reported in the literature [7] for Pd-Pd, Au-Au and Pd-Au interactions and will be discussed in detail in Chapter IV.

2.3. Density Functional Theory (DFT)

Density Functional Theory is one of the approaches used in order to solve a system of interacting electrons based on the principles of quantum mechanics [25]. This is a popular method used in order to calculate a system's energy, electronic structure, geometry optimization, etc. [8]. The formalism is described below.

The interaction of N electrons in the ground state can be described by the Hamiltonian $\hat{H}$ [30]:

$$\hat{H} = \hat{T} + \hat{V} + \hat{V}_{ee} \tag{2.7}$$

where $\hat{T}$ is the kinetic energy, $\hat{V}$ is the external potential and $\hat{V}_{ee}$ corresponds to the electron-electron interaction.

In an explicit form, the Hamiltonian can be written as:

$$\hat{H} = -\frac{1}{2}\sum_{i=1}^{N_e}\nabla_i^2 + \sum_{i=1}^{N_e}\sum_{a}^{N}\frac{Z_a}{\left|\vec{r}_i - \vec{R}_a\right|} + \sum_{i=1}^{N_e}\sum_{j\neq i}^{N_e}\frac{1}{\left|\vec{r}_i - \vec{r}_j\right|} = -\frac{1}{2}\sum_{i=1}^{N_e}\nabla_i^2 + \sum_{i=1}^{N_e}\upsilon\left(\vec{r}_i\right) + \sum_{i=1}^{N_e}\sum_{j\neq i}^{N_e}\frac{1}{\left|\vec{r}_i - \vec{r}_j\right|} \tag{2.8}$$

where $\upsilon(\vec{r}_i) = -\sum_{a=1}^{N}\frac{Z_a}{\left|\vec{r}_i - \vec{R}_a\right|}$ is the 'external' potential acting on electron i, due to nuclei of charge Z_a and vector coordinate $\vec{R}_a$, N is the total number of atoms and N_e is the total number of electrons.

The Hamiltonian described in equation (2.8) takes into account the Born-Oppenheimer approximation according to which the atomic nucleus is fixed in position with respect to the electrons due to the mass difference between the nucleus and the electrons. As a consequence, the

Hamiltonian will describe a decoupled motion between electrons and the nuclei. Hence, equation (2.8) will only need to be resolved for the electronic part.

In this formalism, the energy of a system E, can be written as a functional of the electron wavefunction, Ψ, in the following way:

$$E\left[\Psi\right]=\int \Psi^{*}(\vec{r}_1,\vec{r}_2,\ldots,\vec{r}_n)\hat{H}\Psi(\vec{r}_1,\vec{r}_2,\ldots,\vec{r}_n)\,d\vec{r}_1\,d\vec{r}_2\ldots d\vec{r}_n=\left\langle\Psi\middle|\hat{H}\middle|\Psi\right\rangle \tag{2.9}$$

The energy of the system must satisfy the variational principle according to which the energy computed from a 'guessed' wavefunction Ψ is an upper bound to the true ground state energy, E_0 [25]:

$$E\left[\Psi\right]\geq E_0 \tag{2.10}$$

A way of identifying the energy of the system is to solve equation (2.7) analytically. However, this is *not feasible* and an approximation of the energy of the system is made in modern DFT. The fundamentals of modern DFT have been stated in the paper of Hohenberg and Kohn [31] (1964) and subsequently in the work of Kohn and Sham [32], in 1965. These papers describe a formalism, in which the ground state properties such as the total electronic energies, the equilibrium positions, etc. can be expressed with the help of the total electronic density, $\rho(\vec{r})$. Two theorems sit at the basis of modern DFT and are stated below [25, 32]:

Hohenberg-Kohn I: The external potential and the total energy of the system (represented by the Hamiltonian in equation (2.7)) is *uniquely* determined *within an additive constant*, by the total electron density, $\rho(\vec{r})$. This means that the energy is a functional of the density.

Hohenberg-Kohn II: The functional that determines the ground state energy of a system determines the lowest energy if and only if the input density is the ground state density.

Here, the electron density is:

$$\rho(\vec{r}) = \langle \psi | N | \psi \rangle \tag{2.11}$$

where $N = \sum_i \delta(\vec{r} - \vec{r}_i)$ is the total number of interacting electrons.

The second Hohenberg-Kohn theorem is a reformulation of the variational principle, in which the energy functional is dependent of the total electronic density and *not* on the wavefunction [33]:

$$E\left[\rho\left(\vec{r}\right)\right] \geq E_0 \tag{2.12}$$

Assuming the differentiability of $E\left[\rho\left(\vec{r}\right)\right]$, this imposes that the ground state energy satisfies the *stationary principle* [25]:

$$\delta\left[E\left[\rho\left(\vec{r}\right)\right] - \mu\left[\int \rho\left(\vec{r}\right)d\vec{r} - N_e\right]\right] = 0 \tag{2.13}$$

The energy functional can be derived from equation (2.8) in the following manner:

$$E\left[\rho\left(\vec{r}\right)\right] = T\left[\rho\right] + V_{ne}\left[\rho\right] + V_{ee}\left[\rho\right] = \int \rho\left(\vec{r}\right)\upsilon(\vec{r})\,d\vec{r} + F_{HK}\left[\rho\right] \tag{2.14}$$

where

$$F_{HK}\left[\rho\right] = T\left[\rho\right] + V_{ee}\left[\rho\right] \tag{2.15}$$

As equation (2.15) shows, the functional $F_{HK}\left[\rho\right]$ is independent on the external potential $\upsilon\left(\vec{r}\right)$; this means that the quantity $F_{HK}\left[\rho\right]$ is a universal functional of density.

The kinetic and electron interactions (the terms $T\left[\rho\right]$ and $V_{ee}\left[\rho\right]$ in equation (2.15)) can only be approximated. Kohn and Sham [32] proposed a method to compute the kinetic energy of a system of N_e non-interacting electrons with enough accuracy (up to a residual correction), by introducing orbitals (denoted as ϕ_i) into the formalism. This is explained below.

The kinetic energy of a system of N_e *non-interacting electrons* can be expressed as follows:

$$T_n = \sum_{i=1}^{N_e} \left\langle \phi_i \left| -\frac{1}{2}\nabla^2 \right| \phi_i \right\rangle \tag{2.16}$$

The ground state density can be expressed as [25,32]:

$$\rho\left(\vec{r}\right) = \sum_{i=1}^{N_e} \left|\phi_i\right|^2 \tag{2.17}$$

In this formalism, the energy functional (2.14) can be re-written taking into consideration that the electron-electron interaction comprise classic Coulomb energy (the Hartree energy, V_H) and the exchange-correlation functional $E_{xc}\left[\rho\right]$:

$$E\left[\rho\right] = T_n\left[\rho\right] + V_{ne}\left[\rho\right] + V_H\left[\rho\right] + E_{xc}\left[\rho\right] \tag{2.18}$$

Explicitly, the Hartree energy can be expressed as [11]:

$$V_H\left[\rho\right] = \frac{1}{2}\int \frac{\rho\left(\vec{r}_1\right)\rho\left(\vec{r}_2\right)}{\left|\vec{r}_1 - \vec{r}_2\right|} dr_1 dr_2 \tag{2.19}$$

and the exchange correlation functional is the sum of errors arising when a non-electron interacting kinetic energy is used and the error arising when the classical electron-electron interaction is used [25, 33].

$$E_{xc}\left[\rho\right] \equiv T\left[\rho\right] - T_n\left[\rho\right] + V_{ee}\left[\rho\right] - V_H\left[\rho\right] \tag{2.20}$$

Equation (2.20) is the exchange-correlation energy.

Considering the stationary principle (2.13) for the case of the energy functional (2.20), and considering that the functional is indirectly dependent on the non-interacting orbitals ϕ_i (through equation (2.17), one can derive the Kohn-Sham equations [30]:

$$\left[-\frac{1}{2}\nabla^2+\upsilon(\vec{r})+\int\frac{r(\vec{r}\,')}{|\vec{r}-\vec{r}\,'|}dr'+\upsilon_{xc}(\vec{r})\right]\phi_i^{KS}(\vec{r})=\varepsilon_i\phi_i^{KS}(\vec{r}) \tag{2. 21}$$

In equation (2.19), ϕ_i^{KS} are the Kohn-Sham orbitals and υ_{xc} is the exchange-correlation potential:

$$\upsilon_{xc}=\frac{\delta E_{xc}[\rho]}{\delta\rho[\vec{r}]} \tag{2.22}$$

DFT *does not* offer a description on how to find the value of the exchange-correlation energy, $E_{xc}[\rho(\vec{r})]$. However, DFT *emphasizes* the existence of $E_{xc}[\rho(\vec{r})]$, the universal functional, which is valid for all the systems. Various *approximations* have been further proposed [25], namely the Local-Density Approximation (LDA) [34] and the generalized-gradient approximation (GGA) [34, 35, 36]. A brief description of both approximations is given below.

The Local Density Approximation (LDA)

In this formalism, the expression of $E_{xc}[\rho(\vec{r})]$ is approximated by considering an inhomogeneous system of charge distribution treated as locally homogeneous.

The functional $E_{xc}\left[\rho\left(\vec{r}\right)\right]$ is approximated as an integral of the product between a local functional, $\varepsilon_{xc}^{LDA}\left[\rho\left(\vec{r}\right)\right]$ and the electron density, $\rho\left(\vec{r}\right)$:

$$E_{xc}^{LDA}\left[\rho\left(\vec{r}\right)\right]\approx\int\varepsilon_{xc}^{LDA}\left[\rho\left(\vec{r}\right)\right]\cdot\rho\left(\vec{r}\right)d\vec{r} \tag{2.23}$$

Here, $\varepsilon_{xc}^{LDA}\left[\rho\left(\vec{r}\right)\right]$ indicates the exchange and correlation energy per particle of a uniform gas of density ρ [25] and can be written as

$$\varepsilon_{xc}^{LDA}\left(\rho\right)=\varepsilon_{x}\left(\rho\right)+\varepsilon_{c}\left(\rho\right) \tag{2.24}$$

The exchange-correlation potential becomes:

$$\upsilon_{xc}^{LDA}=\frac{\delta E_{xc}^{LDA}\left[\rho\right]}{\delta\rho\left(\vec{r}\right)} \tag{2.25}$$

and the Kohn-Sham equations become:

$$\left[-\frac{1}{2}\nabla^{2}+\upsilon\left(\vec{r}\right)+\int\frac{\rho\left(\vec{r}\,'\right)}{\left|\vec{r}-\vec{r}\,'\right|}dr'+\upsilon_{xc}^{LDA}\left(\vec{r}\right)\right]\phi_{i}^{KS}=\varepsilon_{i}\phi_{i}^{KS} \tag{2.26}$$

The solution of equation (2.26) defines the Kohn-Sham local-density approximation (LDA).

The Generalized Gradient Approximation (GGA)

In this formalism, the exchange-correlation functional can be approximated as:

$$E_{xc}^{GGA}\left[\rho\right]\approx\int\rho\left(\vec{r}\right)\varepsilon_{xc}\left(\rho,\nabla\rho\right)d\vec{r} \tag{2.27}$$

in which the exchange-correlation functional is explained in terms of density gradient. This approximation describes well systems with low-varying electron densities and is known to explain better than LDA approximation quantities such as binding energies of nanoparticles [8, 35, 37].

Conclusions

This chapter aimed to offer a short description of the theoretical principles used in this thesis in order to study the structure and energetics of the bimetallic nanoparticles. We have offered a description of the principles of search methods such as Genetic Algorithms and basin Hopping Monte Carlo, as well as the principles of Density Functional Theory. These concepts are used throughout Chapter IV and Chapter V as follows. Chapter IV is focused on the determination of the structure and stability of bimetallic AuPd nanoparticles using a Genetic Algorithms coupled with Gupta potentials to model the inter-atomic interactions. The search has been then refined using the Basin Hopping Monte Carlo algorithm, followed by a relaxation of the Global Minimum cluster (and clusters located at compositions close to the global minimum) at the DFT level. Chapter V will however be focused on a direct search at the DFT level of the equilibrium structure for the $Au_{24}Pd_1$ nanoclusters in order to determine structure, energetics and atomic arrangements of this particular cluster.

Bibliography

---

[1] Kelly, K. L., Coronado, E., Zhao, L. L., Schatz, G. C., *J. Phys. Chem. B.*, 107, 668, **2003**.

[2] Johnston, R. L., *Atomic and Molecular Clusters*, Taylor & Francis, London, **2002**.

[3] Jellinek, J., Krissinel, E. B. (eds.), *Theory of Atomic and Molecular Clusters*, Springer, Berlin, **1998**.

[4] Jellinek, J., Garzon, I., *Z. Phys. D.*, 20, 239, **1991**.

[5] Johnston, R. L., *Dalton Trans.*, 22, 4193, **2003**.

[6] Paz-Borbon, L. O., Johnston. R., Barcaro, G., Fortunelli, A., *J. Chem. Phys.*, 128, 134517, **2008**.

[7] Ismail. R., Johnston. R. L., *Phys. Chem. Chem. Phys*, 12, 8607, **2010**.

[8] Paz-Borbon, L. O., *Computational studies of transition metal nanoalloys*, Springer, Berlin, **2011**.

[9] Pittaway, F., Paz-Borbon, L. O., Johnston, R. L., Arslan, H., Ferrando, R., Mottet, C., Barcaro, G., Fortunelli, A., *J. Phys. Chem. C*, 113, 9141, **2009**.

[10] Wales, D. J. in *Energy landscapes with applications to clusters, biomolecules and glasses*, Cambridge University Press, Cambridge, **2003**.

[11] Gehrke, R., PhD thesis, University of Berlin, **2008**.

[12] Kunz, R. E., Berry, R. S., *J. Chem. Phys.*, 103, 1904, **1995**.

[13] Baletto, F., Mottet, C., Ferrando, R., *Phys. Rev. B.*, 63, 155408, **2001**.

[14] Holland, J., *Adaptation in Natural and Artificial Systems*, University of Michigan Pres., Ann Arbor, MI, **1975**.

---

[15] Goletsis, Y., Papaloukas, C., Fotiadis, D. I., Likas, A., Mikhalis, L. K., *IEEE Trans. Biomed. Engin.*, 10, 1717, **2005**.

[16] Johnston, R. L., Mortimer-Jones, T. V., Roberts, C., Darby, S., Manby, F. R., *Application of Genetic Algorithms in Nanoscience: Cluster Geometry Optimization, Lecture Notes in Computer Science*, 2279, 92, **2002**.

[17] Zeiri, Y., *Phys. Rev. E.*, 51, 2769, **1995**.

[18] Byrd, R. H., Lu, P., Nocedal, J., Zhu, C., *J. Scient. Comp.*, 5, 1190, **1995**.

[19] Deaven, D. M., Ho, K. M., *Phys. Rev. Lett.*, 75, 228, **1995**.

[20] Haupt, R., R. L., Haupt, S. E., *Practical Genetic Algorithms*, Wiley Interscience, Hoboken, **1998**.

[21] Rossi, G., Ferrando, R. in: *Nanomaterials: Design and Simulations*, Balbuena, P. B., Seminario, J. M. (eds.), Elsevier, Amsterdam, **2007**.

[22] Doye, J. P. K., *Phys. Rev. E.*, 62, 8753, **2000**.

[23] Bruma, A., Ismail, R., Paz-Borbon, L., Arslan, H., Barcaro, G., Fortunelli, A., Li, Z. Y., Johnston, R. L., *Nanoscale*, 5, 646, **2013**.

[24] Leary, R. H., Doye, J. P. K., *Phys. Rev. E.*, 60, R6320, **1999**.

[25] Parr, R., Yang, W., *Density Functional theory of Atoms and Molecules,* Oxford University Press, Oxford, **1989**.

[26] Ekardt, W., *Metal Clusters*, Springer, Berlin, **1999**.

[27] Ferrando, R., Jellinek, J., Johnston, R. L., *Chem. Rev.*, 108, 846, **2008**.

[28] Gupta, R. P., *Phys. Rev. B*, 23, 6275, **1981**.

[29] Cleri, F., Rosato, V., *Phys. Chem. B*, 48, 22, **1993**.

---

[30] Wichmann, E. H., *Berkeley Physics Course: Quantum Physics*, McGraw Hill, Berkeley, **1965.**

[31] Hohenberg, P., Kohn, W., *Phys. Rev*, 136, (3B) B864, **1964**.

[32] Kohn W., Sham, L. S., *Phys. Rev*, 140, (4A) A1133, **1965**.

[33] Tran, D., *Gold-containing bimetallic nanoparticles*, PhD thesis, University of Birmingham, UK, **2010**.

[34] Kohn, W., *Rev. Mod. Phys*., 51, 1253, **1999**.

[35] Perdew, J. P., Wang, Y., *Phys. Rev. B*, 33, 8800, **1986**.

[36] Perdew, J. P., Chevary, J. A., Vosko, S. H., Jackson, K. A., Pederson, M. R., Singh, D. J., Fiolhaus, C., *Phys. Rev. B*, 46, 6671, **1992**.

[37] Perdew, J. P., Burke, K., Ernzerhof, M., *Phys. Rev. Lett.,* 77, 3865, **1996**.

Chapter III

Experimental characterization of nanoparticles:

The Aberration-Corrected Scanning Transmission Electron Microscope (AC-STEM)

3.1. Overview

This chapter is dedicated to a brief description of the instrumentation used to characterize the bimetallic nanoparticles. The chapter will be focused on the description of the working principle of the Scanning Transmission Electron Microscope (STEM), a description of the image formation, lens aberrations and components. The chapter will then be focused on the practical use of STEM for the analysis of the bimetallic nanoparticles, referring to measurements of integrated intensities, determining nanoparticles aspect ratio and other geometrical, morphological and structural characterization, concepts that will be used further in the practical analysis of bimetallic systems.

3.2. The instrument

The invention of the Transmission Electron Microscope (TEM) in 1931-1934 by Max Knoll and Ernst Ruska [1-4] was a ground breaking discovery. (S)TEM is one of the most powerful non-destructive analysis techniques for nanoparticles of a few nanometers in size, used in order to reveal the size, morphology, crystalline structure, etc. Although other imaging techniques, such as the Atomic Force Microscope and Scanning Tunelling Microscope can also be used for the characterization of nanoparticles (size, shape, etc.), bimetallic nanosystems cannot be sufficiently well characterized by these techniques.

Scanning Transmission Electron Microscopy is a “penetrating technique”, allowing atomic resolution imaging on nanoparticles, as it has the ability to discern the contrast between two or more metals of various atomic numbers, to perform analysis regarding elemental distribution, electron energy loss spectrometry, etc. By optimizing microscope conditions (e.g. electron beam current, acceleration voltage, etc.), nanoparticles can be observed with minimized damage or, on the contrary, to study their structural evolution under electron beam.

In this chapter, a description is provided of the working principle of TEM and TEM-based analysis techniques for the characterization of bimetallic AuPd nanoparticles.

A TEM consists in (see Figure 3.1):

- Illumination system
- Specimen stage
- Objective lens
- Magnification system
- Data recording system
- Elemental analysis system

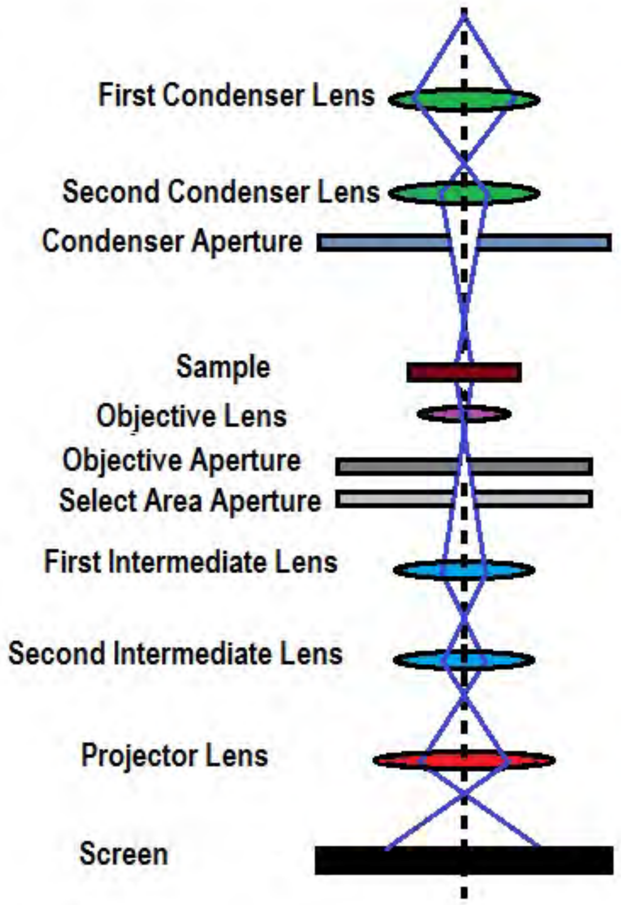
First Condenser Lens
Second Condenser Lens
Condenser Aperture
Sample
Objective Lens
Objective Aperture
Select Area Aperture
First Intermediate Lens
Second Intermediate Lens
Projector Lens
Screen

Figure 3.1. A schematic representation of the diagram of rays in a TEM. Adapted after Ref. [5].

3.2.1. The Illumination system

Electrons are generated by an electron gun, accelerated towards an anode and focused on a specimen with the help of a condenser lens. An electron gun must fulfil several conditions: high brightness, a small source size (i.e. electrons must emanate from a single point on a filament surface), small energy spread.

Assuming that all electrons emanate from the same circular region of radius *r*, on the tip of the filament, then a point *P* at a distance *q* from the filament (Figure 3.2), will "see" the electron source with surface area of πr^2. The source size is typically expressed as a solid angle, $\Omega = \frac{\pi r^2}{q^2} = \pi\theta^2$. The total current density, *j*, passing through the point *P* is [5]:

$$B = \frac{j}{\pi\theta^2} \tag{3.1}$$

where *B* is the beam brightness. A higher current density will thus increase the beam brightness.

One of the conventional ways to generate electrons is by *thermoionic emission*. For this process, a filament tip (typically a hairpin shaped or a pointed tungsten wire) is heated such that the energy of electrons exceeds the energy of the work function (*W*) and leave the tip. This process is possible for materials with high melting temperatures (such as tungsten) or with low work function, such as lanthanium hexaboride (LaB_6) [5, 6]. The current density is given by:

$$j = AT^2 e^{\frac{-W}{k_B T}} \tag{3.2}$$

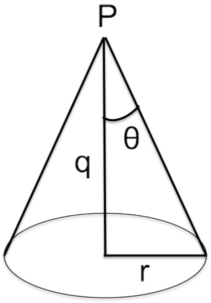

Figure 3.2. Schematic illustration of a solid angle and aperture semi-angle, θ. Adapted after Ref. [5].

In equation (3.2), A is called the Richardson-Dushman constant, k_B is the Boltzmann constant and T is the temperature [5]:

$$A = \frac{4\pi m e k_B^2}{h^3} = 1.20175 \times 10^6 \quad \frac{A}{m^2 K^2} \tag{3.3}$$

Here, m is the mass of electron, e is the charge and h is Planck's constant. LaB_6 filaments are typically employed due to their operating temperatures (ranging between 1800 K and 1900 K [5]), increasing the brightness and reducing the energy spread of the emitted electrons [6].

Another method used to generate electrons is by applying a high electric field at a small tip. If the tip radius is around 10-50 nm then, typically, fields in the range 10^7-10^8 V/cm are generated. This enables electrons to tunnel through the potential barrier. If the electric fields are larger than 10^7 V/cm, the electron current density can be described as [7, 8]:

$$j = \frac{1.54 \times 10^{-6}}{W t^2 (y)} E^2 e^{-\frac{-6.8\times10^{-7} v(y) W^{\frac{3}{2}}}{E}} \tag{3.4}$$

where E is the electric field applied at the tip, W is the work function, v and t depend through y ($y=3.79\text{x}10^{-4}E^{1/2}/W$) to the applied electric field and have been described in the literature [9, 10]. These types of sources are called *(cold) field emission guns (cold FEGs).* Important features of these types of electron guns are: a reduced size of the emitting area, and a value of brightness three orders of magnitude larger than for thermoionic sources (See Table 3.1) [5, 6]. However, the use of FEGs implies ultra high vacuum (UHV) (values of ~ 10^{-10} mbar) to keep the surface of the electron emitter clean, and it also involves magnetic shielding around the electron emitter. It is important to mention that the lifetime of such sources is short [8].

For *thermal-assisted FEGs*, a tungsten filament is coated with a fine layer of ZrO (*Schottky*); in this case, the work function is reduced from 4.5 eV to approximately 2.5 eV [5]. Following the coating, the operating temperature for these types of guns is also reduced to 1800 K. The Schottky guns are very common in commercial TEMs and preferred, due to their high lifetime, stability and high intensity [6]. A few features of each electron gun described above is given in Table 3.1. For the microscope used in this work, the JEOL JEM2100F, a Schottky Field Emission Gun is employed. The operating voltages used in a TEM are usually comprised between 80-300 kV [6]. For example, a TEM operating at 80 kV implies a speed of electrons of approximately 150 000 km/s, a value which is half the speed of light [6]. This value rises to 230 000 km/s for a 300 kV TEM. As observed, the values of electron velocities are fractions of the speed of light. Therefore, a relativistic correction is necessary for the wavelength. Considering the wave-particle dualism, the wavelength is $\lambda = \frac{h}{p}$, where h is the Plank constant and p is the relativistic momentum of electrons. Considering the rest mass of the electron, m_0 and its charge, e, the velocity given by an electric potential V is $v = \sqrt{\frac{2eV}{m_0}}$, implying a wavelength of $\lambda = \frac{h}{\sqrt{2em_0V}}$.

The relativistic correction however implies that [6]:

$$\lambda = \frac{h}{\sqrt{2em_0V}} = \frac{1}{\sqrt{2m_0eV\left(1+\frac{eV}{2m_0c^2}\right)}} \tag{3.5}$$

Considering equation 3.5, for a 200 kV TEM the wavelength is 2.5 x 10^{-3} nm. This basically allows determination of distances of ~ 1.5x10^{-3} nm [11]. This value is much smaller than the length scale of atoms, where atomic radii are typically of the order of 0.1 nm and the inter-atomic spacings are of the order 0.2-0.5 nm. This would imply that, if we ignore limitations imposed by the imaging system, electrons accelerated to voltages of this order are able to interact with atoms in order to reveal atomic scale information about the sample.

Table 3.1. Approximate values of parameters characterizing electron guns. From Ref. [5].

	Thermoionic emission		Field emission	
	LaB_6	Tungsten	Schottky	Field emission
Work function (eV)	2/7	4.5	2.8	4.5
Operating temperature (K)	1700	2700	1800	300
Current density (A/cm^2)	25-100	1-3	10^4-10^6	10^4-10^6
Source diameter (nm)	10 000	50 000	10-15	3-5
Brightness ($A/ cm^2 sr$)	10^6	10^4	10^8-10^9	10^8-10^9
Energy spread (eV)	0.5-2	1-3	0.3-1	0.2-0.3
Gun vacuum (mbar)	10^{-7}	10^{-5}	10^{-9}	10^{-10}
Lifetime (hrs)	500-1000	25-100	> 1000	>1000

3.2.2. High resolution TEM. Image formation

We first illustrate the image formation process in a conventional TEM (Figure 3.3). The TEM will be depicted as a single lens microscope, in which a single objective lens is considered for imaging. The main justification of this approach is that the resolution in a TEM is mainly determined by the objective lens [5, 12]. In Figure 3.3, for simplification, the intermediate lenses and the projection lenses will be omitted [12]:

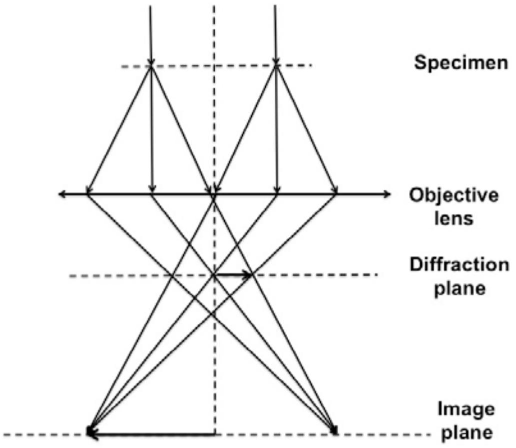

Figure 3.3. Image formation mechanism in a TEM. From Ref. [12].

As illustrated in Figure 3.3, a thin specimen is illuminated by a parallel electron beam. When the electron beam passes through the specimen, it will be diffracted by the periodic crystal lattice of the specimen, forming the Bragg beams, which will be propagating in different directions. The interaction with the specimen will result in changes in amplitude and phase of the electron waves. These changes are described by the principles of quantum mechanical diffraction theory, and their description is beyond the purpose of this thesis. We note the transmitted wave function with $\psi(x,y)$; the transmitted wave function will contain all the structural information about the specimen. The diffracted beams will be then focused in the back focal plane, where an objective aperture can be inserted. A thin ideal lens will bring the transmitted waves to a focus on the axis in the back focal plane [13]. All the waves leaving the specimen at the same angle θ with the optical axis will be focused at a point in the back focal plane and will form a *diffraction pattern*. However, the electrons scattered at the angle θ will also be affected by the spherical aberration and objective lens defocus respectively, experiencing a phase shift. The phase shift can be caused by: (1) the spherical aberration - this is caused by the change in the focal length depending on the electron scattering angle; (2) the objective lens defocus - caused by the spherical characteristics of the emitted electron waves in free space (Huygens principle) [12, 14]. The diffraction amplitude function in the diffraction plane (back focal plane) is given by [5, 12]:

$$\psi'(\vec{u}) = \psi(\vec{u}) e^{i\chi(\vec{u})} \tag{3.6}$$

where $\psi(\vec{u})$ is the Fourier transform (FT) of the wave $\psi(\vec{r})$ at the exit surface of the specimen, vector $\vec{u}$ is the reciprocal space vector, related to the scattering angle θ through the relation $u = 2\sin(\theta)/\lambda$. In equation (3.6), $\chi(\vec{u})$ is the phase function introduced by the objective lens and is dependent on both the spherical aberration coefficient of this lens, (Cs) and the objective defocus (Δf) respectively [12]:

$$\chi(\vec{u}) = \pi \Delta f \lambda u^2 + \frac{\pi}{2} C_s \lambda^3 u^4 \tag{3.7}$$

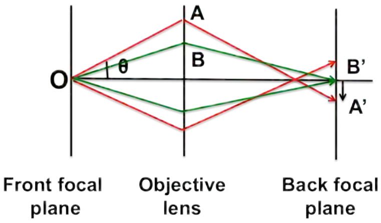

Figure 3.4. Schematic diagram illustrating the phase shift introduced by the spherical aberration. From Ref. [5].

In equation (3.7), the *phase due to the spherical aberration* of the objective lens is related to the variation in the focal length as a function of the electron scattering angle, which results in a path length difference [12]. This is illustrated schematically in Figure 3.4: ray OA, scattered at a higher angle is focused at a shorter focal length in comparison to ray OB scattered at a smaller scattering angle. Therefore, a broadening of the image will be observed in the back focal plane. The *phase shift which related to the defocus* is the phase shift of the electrons scattered at an angle θ due to an increase in the path length [12].

As described in Ref. [12], any TEM image of a crystalline specimen is formed by the interference of the Bragg reflected beams. However, since the phase of each Bragg beam is affected by the phase shift introduced by both the spherical aberration and the defocus, the information about the object will be transmitted non-linearly [12]. Taking into account the considerations above, the image intensity can be expressed mathematically as the inverse Fourier transform (FT^{-1}) of $\psi'(\vec{u})$ [12]:

$$I(x,y) = \left|FT^{-1}[\psi'(\vec{u})]\right|^2 = \left|\psi(x,y) \otimes t_{obj}(x,y,\Delta f)\right|^2 \tag{3.8}$$

Here, by $\otimes$ we understand the convolution product between $\psi(x,y)$ and $t_{obj}(x,y,\Delta f) = FT[\exp(i\chi(\vec{u}))]$; the latter is the inverse Fourier transform of the phase function $\exp(i\chi(\vec{u}))$ [12].

3.3. Types of contrast

There are several types of contrast in a TEM: the diffraction contrast, phase contrast and thickness contrast respectively. The *diffraction contrast* is mainly produced due to deformations in the lattice of the specimen: strains, defects and dislocations. These perturb the intensity of the diffracted beam [15].

In the *phase contrast*, the incident electron wave is modulated in phase when it transmits through the crystal potential, $V_{crystal}(x,y,z)$ [12]. When an electron passes through a specimen of thickness *d*, its kinetic energy will be perturbed by the variation of the potential field [12]. This will result in a phase shift in comparison to an electron wave which will travel in a space free of potential field. The phase shift can be written as [12]:

$$\psi \approx \frac{\pi}{\lambda V_{acc}} V_{crystal}(x,y) \tag{3.9}$$

If we note $\sigma = \frac{\pi}{\lambda V_{acc}}$ then equation (3.9) can be re-written as:

$$\psi \approx \sigma V_{crystal}(x,y) = \sigma \int_0^d V(x,y,z)\,dz \tag{3.10}$$

where *d* is the specimen thickness. Equation (3.10) shows that the phase contrast image is the result of the thickness-projected image along the beam direction (the *z* axis) [12, 14].

The electrons which are transmitted through a thin specimen can be characterized by a phase modulation function [12]. In this approximation, we assume that the electron wave function is modulated only in phase and not in amplitude. In this case, the electron wave at the exit surface of a thin specimen can be written as [12]:

$$\psi(x,y) \approx \exp[i\sigma V_{crystal}(x,y)] \tag{3.11}$$

Considering that the incident electron beam travels along a low-index zone axis, then, according to eq. (3.11) the variation of the thickness-projected potential is fast. This is happening since an atom can be considered as a narrow potential well of width of ~ 0.2-0.3 Å [12]. This variation sits at the basis of the phase contrast in a conventional TEM.

The third type of contrast is the Z-contrast (*atomic number contrast*). Atoms with various atomic numbers have different scattering powers. Here, if the image is formed by collecting electrons scattered at high angles, then the image contrast will be sensitive to the atomic number [12]. This type of contrast is employed in the Scanning Transmission Electron Microscope (STEM), and will be discussed later.

If the electrons pass through an extremely thin specimen, then, in equation (3.11) we can approximate $\left|\sigma V_p\right| << 1$ [12]:

$$\psi(x,y) \approx 1 + \sigma V_{crystal}(x,y) \tag{3.12}$$

Therefore, if we consider equation (3.8) and (3.12), and if we ignore the term σ^2, the image intensity can be written as [12]:

$$I(x,y) \approx 1 + 2\sigma V_p \otimes t_s(x,y,\Delta f) \tag{3.13}$$

where $t_s = \operatorname{Im}\left[t_{obj}(x,y,\Delta f)\right]$.

From equation (3.13), we understand that a phase modulation which is introduced by the objective lens will result in a contrast variation in the observed image [12, 14]. Although we have used the first order approximation as a simplification, this is still useful in order to describe the physics of the TEM imaging [16]. A TEM image is a two-dimensional projection of an object, in which atomic columns are observed as spots if their orientation is parallel to the electron beam [12].

As mentioned above, in a TEM the spherical aberration coefficient is maintained at a fixed value, the value of the defocus being the only varying parameter [12]. Therefore, by varying the value of the defocus, the contrast in a HRTEM will be varied as well. Following the variation of the defocus, the projection of the atomic columns will modify, as dark and bright spots.

3.5. The High Angle Annular Dark Field (HAADF) Scanning Transmission Electron Microscope (STEM)

In STEM, a convergent beam of electrons is raster-scanned across a sample. The transmitted and scattered electrons can be detected post specimen, using various detectors.

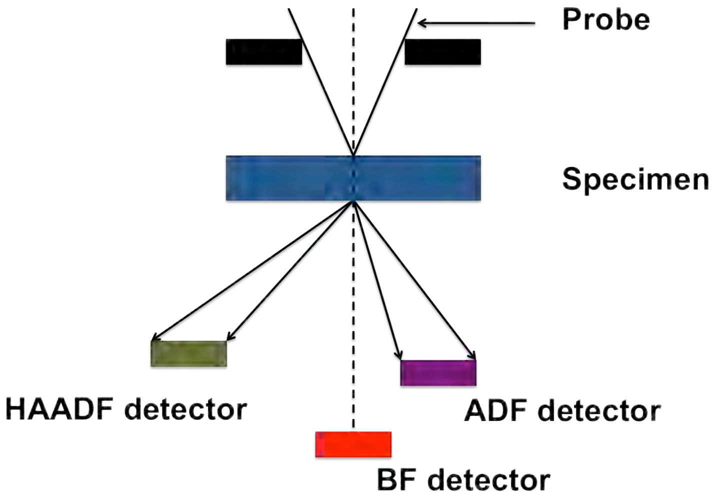

Figure 3.5. Schematic representation of STEM showing the position of the detectors. In this thesis, both the HAADF and BF detectors have been used. Adapted after Ref. [17]

Two types of detectors are the most commonly employed: the Bright Field (BF) detector and High Angle Annular Dark Filed (HAADF) detector. The BF detector usually collects electrons that are scattered at low angles, smaller than 10 mrad with respect to the optical axis [12]. This detector will be thus centred around the optical axis. A HAADF detector collects electrons that are scattered at large scattering angles, typically larger than 40-50 mrad with respect to the optical axis [14] (Figure 3.5.).

3.5.1. BF STEM

According to Refs. [18, 20], the formation of the convergent beam electron diffraction (CBED) pattern in the diffraction plane of the microscope is obtained by placing the electron beam on the specimen. However, in CBED, the convergence angle is chosen to have a small enough value, and therefore the diffraction discs will not overlap. Therefore, the CBED will be independent on the probe position. In STEM however the CBED will overlap, as shown in Figure 3.6 [19]. In the overlap region, different diffracted beams will interfere. In the reciprocal space, the probe position will be written as an aperture function [18, 21]:

$$A(\vec{k}_i) = H(\vec{k}_i)\exp[-i\chi(\vec{k}_i)] \tag{3.14}$$

Here, $\vec{k}_i$ is the incident transverse wave vector. The probe wave function will be written as the Fourier transform of $A(\vec{k}_i)$ [18, 21]:

$$P(\vec{x}) = \int A(\vec{k}_i)\exp[2\pi\vec{k}_i \cdot \vec{x}]d\vec{k}_i \tag{3.15}$$

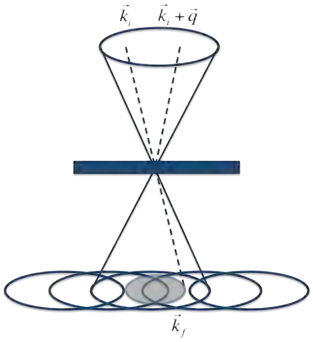

Figure 3.6. Schematic illustration of the formation of the BF STEM image. Due to the overlap of discs, the incident wave vectors, $\vec{k}_i$ and $\vec{k}_i + \vec{q}$ are scattered by the specimen and will interfere in the plane of the detector, forming a final vector, noted $\vec{k}_f$; the phase difference between the two incident plane vectors will depend on the probe position. Adapted after Ref. [19].

Therefore, examining equation (3.15), it is observable that any change in the probe position, $\vec{x}$, will correspond to a phase shift in the reciprocal space. Following this, we can write that $A(\vec{k}_i) \rightarrow A(\vec{k}_i)\exp[-i2\pi\vec{k}_i \cdot \vec{x}_0]$, where $\vec{x}_0$ is the probe position [18, 21].

The intensity in the detector plane can be therefore written as [18,21]: $I(\vec{k}_f, \vec{x}_0) = \left|\int A(\vec{k}_i)\exp[-2\pi i\vec{k}_i \cdot \vec{x}_0]\psi(\vec{k}_f, \vec{k}_i)d\vec{k}_i\right|^2$. If we expand this equation and perform further calculations, then:

$$I(\vec{k}_f, \vec{q}) = \int A(\vec{k}_i)A^*(\vec{k}_i + \vec{q})\psi(\vec{k}_f, \vec{k}_i)\psi^*(\vec{k}_f, \vec{k}_i + \vec{q}) \qquad (3.16)$$

We can interpret equation (3.16) in the following manner [18]: two incident plane waves, $\vec{k}_i$ and $\vec{k}_i + \vec{q}$ will be scattered by the specimen into a final wave vector, $\vec{k}_f$ in the detector plane, as shown in Figure 3.6. In the detector plane, interference will occur and this will contribute to the image spatial frequency, $\vec{q}$ [18]. This effect will occur only in the disk overlap regions in the CBED [21]. As seen in equation (3.16), the phase difference between the incident plane waves is $2\pi\vec{q} \cdot \vec{x}_0$. While the probe will be raster scanned across the specimen, by changing the value of $\vec{x}_0$, then $\vec{k}_i$ and $\vec{k}_i + \vec{q}$ will always interfere, giving rise to vector $\vec{k}_f$. However, as seen in equation (3.16), since the phase difference will change, this will make the intensity oscillate with a frequency $\vec{q}$. Placing a detector in the diffraction plane, an image will be therefore formed. In the STEM imaging mode, placing a detector on the optical axis, will allow the interference between the central, non-diffracted disc and the diffracted discs [18].

3.5.2. HAADF STEM

When the probe is placed on a column of heavy atoms, more electrons will be scattered at higher angles where the detector will be located, because the atoms with higher atomic number *Z* will scatter electrons in a different manner [5]. The angular distribution of scattering from an atom with the atomic number Z can be written as [17, 19]:

$$\frac{d\sigma(\theta)}{d\Omega} = \frac{e^4 Z^2}{16(4\pi\varepsilon_0)^2 E_0^2 \sin^4 \frac{\theta}{2}} \tag{3.17}$$

Here, e is the charge of the electron, ε_0 is the permittivity of the free space, σ is the scattering cross section, E_0 is the beam energy, Ω is the collection solid angle and Z is the atomic number of the sample. Therefore, heavier atoms (atoms with a larger value of the atomic number *Z*) will scatter more strongly to high angles.

The HAADF-STEM is an incoherent imaging mode, therefore, the image intensity will be a convolution between the probe wave function and the object wave function which represents the specimen [19]:

$$I(x) = |P(x)|^2 \otimes O(x) \tag{3.18}$$

In equation (3.18), $P(x)$ is the point spread function (probe intensity profile) [20]. Equation (3.18) is basically the definition of the incoherent imaging, which imposes that all the rays that emerge from various parts of the specimen do not have a fixed phase relationship [19]. The incoherent scattering in the HAADF-STEM has two causes: (1) the large size of the HAADF detector and (2) the thermal diffuse scattering [21].

If we consider the effect of the detector, then taking into account equation (3.16) we can integrate the value of the intensity in the detector plane over a detector function, $\eta(\vec{k}_f)$ [18]:

$$\tilde{I}(\vec{q}) = \int A(\vec{k}_i - \frac{\vec{q}}{2}) A^*(\vec{k}_i + \frac{\vec{q}}{2}) \times \int \eta(\vec{k}_f) \psi(\vec{k}_f - \vec{k}_i + \frac{\vec{q}}{2}) \psi^*(\vec{k}_f - \vec{k}_i - \frac{\vec{q}}{2}) d\vec{k}_f \, d\vec{k}_i \qquad (3.19)$$

The function $\eta(\vec{k}_f)$ has the value 1 where the detector is present and has the value 0 otherwise [18-21]. If the detector is large, then the second integral will depend on the $\vec{k}_i$ insignificantly. In this case we can separate the two integrals as follows [18]:

$$\tilde{I}_{HAADF}(\vec{q}) = \int A(\vec{k}_i - \frac{\vec{q}}{2}) A^*(\vec{k}_i + \frac{\vec{q}}{2}) d\vec{k}_i \times \int \eta(\vec{k}_f) \psi(\vec{k}_f - \vec{k}_i - \frac{\vec{q}}{2}) d\vec{k}_f = T(\vec{q}) \tilde{O}(\vec{q}) \qquad (3.20)$$

If we consider the inverse Fourier transform of the equation (3.20), then we will obtain the following formula for the intensity in the real space [18]:

$$I_{HAADF}(\vec{x}_0) = \left| P(\vec{x}_0) \right|^2 \otimes O(\vec{x}_0) \qquad (3.21)$$

This equation is the re-formulation of the incoherence principle formulated in equation (3.18).

The equations (3.19)-(3.21) basically state that a large detector relative to the overlap between the discs separated by the reciprocal vector $\vec{q}$ allows the integral in equation (3.19) to be separated [18, 21]. This, expressed mathematically, state that a large detector implies integration over multiple final wave vectors $\vec{k}_f$, destroying the coherence [18].

3.5.3. Probe formation and lens aberrations

The resolution in a STEM image depends on the probe. The smaller is the electron probe then the better the resolution will be. The size of the objective aperture will decide the convergence angle of the incident beam [18]. Several factors such as the electron wavelength, the defocus of the beam as well as the spherical aberration of the probe-forming lens, will determine how large the probe will be. These factors are the most severe limitations of an uncorrected STEM.

In recent years, small probe sizes in commercial TEMs have been achieved [22]. Usually, magnetic lenses used in the microscopes are designed having a circular geometry and all suffer from spherical aberration [21]. In commercial STEMs, multipole lenses can be used in order to correct these effects. These adjustments have been coupled with various computational tunings in order to correct high order aberrations that cannot be corrected manually [20].

The lens aberrations can be chromatic or monochromatic [19,20]. *Chromatic aberrations* appear if the electron beam will contain electrons with a multitude/spectrum of wavelengths. Therefore each electron that will pass through the lens will be deflected by the lens in a different manner, which is dependent on its wavelength. Hence, different wavelengths will cause different focal points and a general loss of image quality. Monochromatic aberrations will basically occur through different path lengths of the electrons from the lens to the focal point [17]. One such aberration is the *spherical aberration* (see Figure 3.4). This type of aberration has been corrected in commercial microscopes by means of a spherical aberration correctors. The idea about the spherical aberration corrected microscopes is to introduce a corrector that produces negative spherical aberration. This then combines with the positive spherical aberration of the objective lens to give a total of zero spherical aberration [5].

Astigmatism is caused by the non-uniform magnetic fields that act upon electrons passing through the lens. The effect of the astigmatism on the electron beam will be similar to the effect of the spherical aberration. However, astigmatism can also be created by the apertures. An incorrectly inserted aperture, non centred along the optical axis may disturb the field. Moreover, if the apertures are contaminated, this is an extra factor that can have an influence on the electron beam [17, 19].

3.5.4. Energy Dispersive X-ray (EDX) Spectroscopy

EDX is a characterization technique that is used for the elemental analysis of the samples. The technique is based on the interaction of the electron beam with the specimen, which produce X-rays characteristic of the elements existent in the specimen. The incident electron beam can excite an electron from an inner shell, ejecting it while creating a hole. An electron from an outer, higher energy shell will then fill this hole, the difference of energy between the higher energy shell and the lower energy shell being released in the form of characteristic X-rays. Characteristic X-rays are then collected in order to map various elements present in the specimen (see Figures 3.7 and 3.8).

For this study, EDX was carried out using the JEOL JEM 2100F Scanning Transmission Electron Microscope fitted with a Brucker silicon drift detector [23]. As shown in Figure 3.7, EDX uses an X-ray detector, placed in the TEM column in close proximity with the specimen stage.

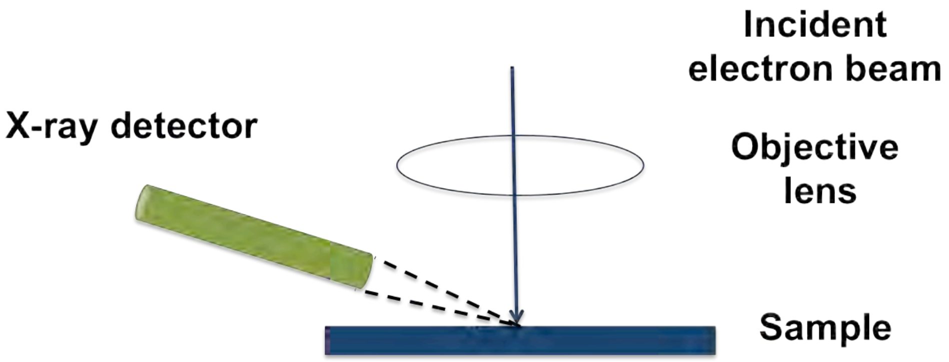

Figure 3.7. Diagram of the EDX detector.

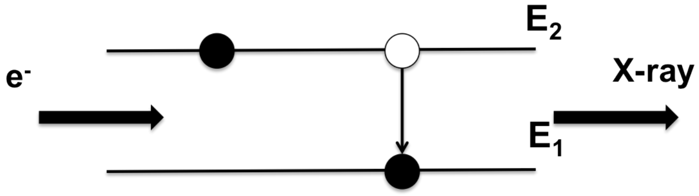

Figure 3.8. Schematic representation of the X-ray principle

The spatial resolution of EDX is influenced by the spatial resolution of the STEM probe. The energy resolution is however determined by the accuracy of the detector [19]. For the analysis in this thesis, EDX has been used in order to perform elemental mapping. This is accomplished by collecting emitted X-rays at a series of points along the scanned area of the sample. The signal collected at each point in the selected area allows the intensities of various elements in the sample to be mapped. However, acquiring elemental maps involves a much longer acquisition time as well as repeating the sample scanning in order to achieve a high count rate. From this point of view, this makes the elemental mapping for small nanoparticles an extremely challenging issue, mainly due to the drift that affects the sample. This has been one of the challenges in mapping the chemical composition of bimetallic AuPd nanoparticles (see Chapter VI), since the nanoparticles have a diameter range of the order of ~ 2-4 nm.

3.6. Conclusions

This chapter aimed to offer a short description of the main components in a TEM, as well as to describe the image formation. The chapter further focuses on the differences and similarities between TEM and STEM, as well as on a description of the two imaging modes used in this thesis, Bright Field and Dark Field STEM. The chapter focused in the last section on the description of the principles of EDX, used for the elemental mapping of the AuPd nanoparticles (see Chapter VI). The next three chapters of this thesis will present exclusively the results regarding the computational and experimental analysis of small and large bimetallic nanoparticles. Chapter IV is focused on the investigation of the structure and energetics of the 98-atom bimetallic AuPd nanoparticles. The results presented further in Chapter V refer to a hybrid experimental and theoretical analysis of the single Pd doped Au_{25} nanoclusters. The last chapter of the thesis refers to the experimental characterization of evaporated AuPd nanoparticles.

Bibliography

---

[1] Ruska, E., *Z. Physik*, 87, 580, **1934**.

[2] Ruska, E., *Z. Physik*, 89, 90, **1934**.

[3] Knoll, M., Ruska, E., *Z. Physik*, 78, 318, **1932**.

[4] Knoll, M., Ruska, E., *Ann. Physik*, 12, 607, **1932**.

[5] De Graef, M., *Introduction to Conventional Transmission Electron Microscopy*, Cambridge University Press, Cambridge, **2003**.

[6]http://www.fei.com/uploadedfiles/documents/content/introduction_to_em_booklet_july_10.pdf

[7] Schwettman, H.A., Turneaure, J.P., Waites, P.F., *J. Appl. Phys*., 45**,** 914, **1974**.

[8] Mogk, S., *PhD thesis*, University of Groningen, **2004**.

[9] Fowler, R. H., Nordheim, L., *Proc. R. Soc*., 119, 173, **1928**.

[10]https://smartech.gatech.edu/bitstream/handle/1853/33206/e18622_186036_fr.pdf.txt?sequence=3

[11]http://www.jeol.com/PRODUCTS/ElectronOptics/TransmissionElectronMicroscopesTEM/200kV/tabid/119/Default.aspx

[12] Wang, Z. L., *J. Phys. Chem. B*, 104, 1153, **2000**.

[13] Wang, Z. L., *Reflection electron microscopy and spectroscopy for surface analysis*, Cambridge Univ. Press, Cambridge, **1996**.

[14] Zhang, J., Wang, Z. L., Liu, J., Chen, S., Liu, G. Y., *Self-assembled nanostructures*, Kluwer Academic Publishers, New York, **2004**.

[15] Hirsch, P. B., Howie, A., Nicholson, R. B., Pashley, R. B., Whelan, M. J., *Electron microscopy of thin crystals*, Roberts E. Krieger Publishing Company, New York, **1977**.

---

[16] Tran, D., *PhD thesis*, University of Birmingham, UK, **2010**.

[17] Permain, D., *PhD thesis*, University of Birmingham, UK, **2011**.

[18] Bjorge, R., *PhD thesis*, Norvegian University of Science and Technology, **2011**.

[19] William, D. B., Carter, C. B., *Transmission Electron Microscopy*, 2nd edition, Springer, Berlin, **2009**.

[20] Pennycook, S. J., *Scanning Electron Microscopy for Nanotechnology*, Springer, Berlin, **2007**.

[21] Nellist, P. D., Penycook, S. J. in *Advances and Imaging in Electron Physics*, Academic Press. Inc., San Diego, **2000**.

[22] Haider, H., Rose, H., Uhlemann, S., Schwan, E., Kabius, B., Urban, K., *Ultramicroscopy*, 75, 53, **1998**.

[23] http://www.bruker.com/en/products/x-ray-diffraction-and-elemental-analysis/x-ray-microanalysis-and-ebsd/quantax-eds-for-tem/overview.html

Chapter IV

DFT Studies of Structure and Energetics of 98-atom AuPd Nanoparticles

4.1. Overview

In this chapter, a theoretical analysis of the structure and energetics of the 98-atom AuPd nanoparticles is made at both empirical level as well as at the DFT level. Global optimization methods based on the use of genetic algorithms (GAs) and Gupta potentials (with different parametrizations) in order to model interatomic interactions are employed for the localization of the global minimum clusters. A detailed analysis of the segregation effects as well as competition between different structural families at both empirical and DFT level is made. The results in this chapter have been published: *Bruma A., Ismail, R., Paz-Borbon, L. O., Arslan, H., Barcaro, G., Fortunelli, A., Li, Z. Y., Johnston, R. L., Nanoscale, 5, 646, 2013.*

4.2. Introduction

A number of DFT theoretical studies have been published for the analysis of the bimetallic AuPd nanoparticles up to 50 atoms [1-4]. From a thermodynamic point of view, the $Pd_{core}Au_{shell}$ configuration is preferred, due to considerations based on concepts such as cohesive energy (E_{coh}), which is larger for Pd than Au (see Table 4.1) and thus maximizing the number of homonuclear bonds, or surface energy (E_{surf}) of Pd which is higher than for Au and thus minimizing the total surface energy of the cluster. Other parameters such as atomic radius (r_a) and electronegativity (χ) can also be used as indicators for the Pd core-segregation: Pd has a smaller atomic radius, which helps minimizing the bulk elastic strain [2]. A degree of charge transfer from Pd to Au is also favourable, due to the lower electronegativity of Pd, as indicated in Ref. [5].

Empirical potentials (EP) have been widely used for the determination of the structure and energetics of bimetallic nanoparticles in order to overcome computational limitations imposed by more computationally expensive first principle calculations. The EP are versatile, but important modifications can be brought by electronic effects [6] and therefore it is important to verify the predictions of the EPs by performing DFT calculations.

The latter are one of the most accurate methods used in order to characterize thoroughly monometallic and bimetallic systems. However, DFT calculations have been limited to a small number of atoms (e.g 50-atom AuPd clusters [4]) due to the highly-demanding computational power necessary in order to explore vast areas of the configurational space.

Table 4.1. Elemental properties of Au and Pd. From Ref. [2].

Element	E_{coh} (eV/atom)	E_{surf} (meV Å^{-2})	r_a (Å)	χ
Pd	3.89	131	1.38	2.2
Au	3.81	96.8	1.44	2.4

The search becomes even more difficult in the case of bimetallic systems, due to the existence of homotops, as described in Chapters I and II.

In this chapter, a hybrid approach based on the use of genetic algorithms (GAs) and Basin Hopping Mone Carlo (BHMC) homotop searching [7] at the EP level, followed by DFT local relaxations have been used to perform a thorough search of the configurational space for the 98-atom AuPd nanoclusters. Three different parametrizations for the Gupta potentials have been used, namely DFT-fit, Exp-fit and Average, and DFT local relaxations have been performed for the putative global minimum clusters identified for all sets of parameters.

The 98-atom clusters have been previously studied for PdPt nanoparticles using hybrid GA and BHMC atom-exchange routine in order to identify the low-energy homotps for a fixed composition [7]. At empirical level, the GA has been able to identify, for fixed sizes and compositions, the existence of the Leary Tetrahedron (LT) as the most stable structure, located at ~ 50%-50% composition. The authors in Ref. [7] have shown that, by further performing an optimization of the chemical ordering using BHMC, the LT structures have been found more stable than other clusters structures, namely FCC-HCP, FCC and Marks Decahedron (M-Dh). However, the analysis regarding the 98-atom PdPt clusters is lacking DFT calculations.

The 98-atom LT cluster is of great interest, as it has been discovered by Leary and Doye as the global minimum (GM) cluster for the 98-atom Lennard-Jones cluster [8]. Moreover, this structure has also been predicted for the case of 98-atom silver (Ag) clusters, as described by the Sutton-Chen potential [l8] and for an aggregate of C_{60} molecules [2]. These findings have motivated our interest in identifying if the LT is a stable structure for the case of AuPd nanoclusters, and to perform the optimization of the analysis of the stability of various structural motifs (LT, FCC-HCP, M-Dh and Icosahedron (Ico)) over a certain compositional range located around $Pd_{49}Au_{49}$, at both empirical and DFT levels.

4.3. Computational Details

4.3.1. Genetic Algorithm parameters

Global structural optimization has been made using a genetic algorithm, as encoded in the Birmingham Cluster Genetic Algorithm (BCGA) program [9], which has been described in detail in Chapter II. The parameters that have been used in this algorithm are: population size=40; crossover rate=0.8 (i.e. 32 offsprings are produced per generation); crossover type=1-point weighted (the splice position is calculated based on the fitness value of the parents); selection=roulette wheel; mutation type=mutate_move; number of generations=400. The high number of GA runs is necessary due to the relative large size of clusters and the presence of homotops. A value of cutoff on distances has not been included.

4.3.2. Basin Hopping Monte Carlo parameters

The Basin Hopping Monte Carlo algorithm [10, 11] has been employed in this analysis for the optimization of the chemical ordering, allowing only Pd-Au atoms exchange moves [11-13] for a fixed size and composition. For each size and composition, a search of 50 000 steps at k_BT=0.05 eV has been performed, followed by a more refined search, of 20 000 steps for k_BT=0.02 eV.

4.3.3. DFT calculations parameters

DFT calculations have been made using Quantum Espresso Plane Wave Self Consistent Field (PWscf) code [14]. Calculations have been made using the Perdew-Burke-Ernzerhof (PBE) exchange-correlation (XC) functional [15] and ultrasoft pseudopotentials. Following convergence and accuracy tests, the following parameters have been used: values of 40 and 160 Ry (1 Ry=13.606 eV) were selected as the energy cut-off for the selection of the plane-wave basis set for the description of the wavefunctions and the electron density respectively.

Eigenvalues and eigenstates of the Kohn-Sham Hamiltonian have been calculated at the gamma point only of a cubic cell of side of approximately 20 Å, applying a Gaussian smearing technique with a broadening of one-particle level of 0.03 eV. The DFT local relaxations were performed by fully relaxing the coordinates of the metal atoms until the forces are smaller than 0.1eV/Å. Calculations have been performed on the University of Birmingham BlueBEAR high performance computer [16].

4.3.4. Gupta Pd-Au parameters

Three sets of parameters have been chosen for the Gupta potential are: DFT-fit, Exp-fit and Average, listed in Table 4.2 (as taken from Refs. [17,18]) and described in detail below.

(a) *DFT fit parameters*: the parameters corresponding to Pd-Pd, Pd-Au and Au-Au interactions are fitted to DFT calculations of solid phases [19]. As described in Ref. [2], this requires rescaling the DFT cohesive energy curves to fit the experimental ones, in order to obtain similar values for the cohesive energy, lattice parameters, etc. The rescaling factors are then used to re-scale the cohesive energy curves of the system which will be used to fit the parameters of the heteronuclear Pd-Au interaction.

(b) *Exp-fit parameters*: the Pd-Pd, Au-Au and Pd-Au parameters are fitted to the experimental properties of bulk Pd, Au and features of the Pd-Au phase diagrams. This implies that, the two parameters of the Gupta potential, A and ξ are fitted to the dissolution energy of one impurity of Pd into bulk Au and viceversa [2].

According to Ref. [2], the values of the dissolution energies are the slope of the mixing enthalpy curves from each side of the Pd-Au phase diagram [20], namely for the Pd-rich phase for the dissolution of one impurity of Au into Pd and Au-rich phase for the dissolution energy of one Pd impurity into Au. Parameters p and q (the repulsive interaction range and the attractive interaction range parameters), as well as the atomic radii for the Pd-Au interactions have been taken as the arithmetic means of the pure values.

(c) *Average parameters*: for this set of parameters, the heteronuclear Pd-Au parameters are obtained as the average of Pd-Pd and Au-Au parameters [21].

4.4. Results and Discussions

4.4.1. Global optimization of 98-atom AuPd nanoclusters

First, an extensive search of the potential energy surface (PES) has been made using a combination of GA and BHMC for the three sets of Gupta potentials (see Section 4.3.4) for all compositions Pd_mAu_{98-m}. Second, the value of the excess energy with respect to the pure clusters has been computed for each set of parameters.

We have then performed a more refined analysis compositional $Pd_{46}Au_{52}$-$Pd_{52}Au_{46}$, corresponding to clusters with the lowest values of the excess energy and performed DFT relaxation calculations. The results regarding the analysis at the EP and DFT level, and the study of competition between different structural families are presented below in detail.

Table 4.2. Comparison of the DFT-fit, Exp-fit and Average (Ave) Gupta potential parameters. From Refs. [17, 18].

	Pd-Pd			**Pd-Au**			**Au-Au**		
	Ave	**DFT-fit**	**Exp-fit**	**Ave**	**DFT-fit**	**Exp-fit**	**Ave**	**DFT-fit**	**Exp-fit**
A (eV)	0.174	0.1653	0.17149304	0.19	0.1843	0.276	0.201	0.2019	0.2095706
ξ (eV)	1.718	1.6805	1.7018732	1.75	1.7867	2.082	1.79	1.8097	1.8152764
p	10.867	10.853	11.000	10.54	10.542	10.56	10.22	10.243	10.139
q	3.742	3.7516	3.794	3.89	3.8826	3.913	4.036	4.0445	4.033
r_0	2.7485	2.7485	2.7485	2.816	2.8160	2.816	2.884	2.8840	2.884

A) Gupta potential with DFT-fit parameters

In Figure 4.1, the DFT-fit potential excess energy curve is shown in blue. The lowest values of the excess energy are located in the compositional range $Pd_{39}Au_{59}$-$Pd_{59}Au_{39}$, corresponding to relatively stable structures. The composition for which the excess energy is minimum is $Pd_{51}Au_{47}$, with an Ino-Dh structure.

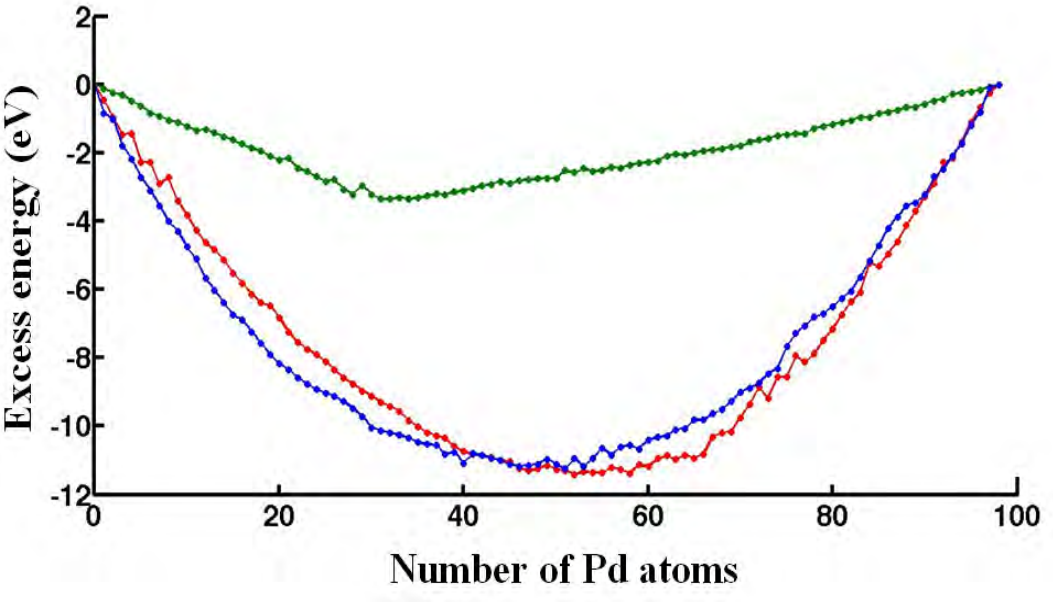

Figure 4.1. Excess energy for 98-atom Pd_mAu_{98-m} clusters with respect to Au_{98} and Pd_{98} clusters, determined for the: DFT-fit (blue curve), Exp-fit (red curve) and Average (green curve) Gupta potentials.

The structural motifs of nanoclusters are shown in Table 4.3. Here we can notice that the dominant structural motif over a wide range ($Pd_{34}Au_{54}$-$Pd_{74}Au_{42}$) is the Marks Decahedron (M-Dh).

Gupta potential	
DFT-fit	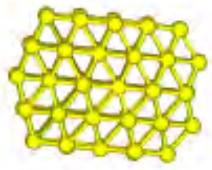 Au_{98} 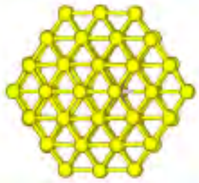 Pd_1Au_{97} 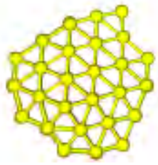 Pd_2Au_{96} 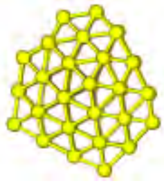 $Pd_{14}Au_{84}$ 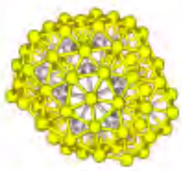 $Pd_{21}Au_{77}$ 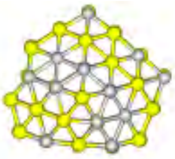 $Pd_{51}Au_{47}$ 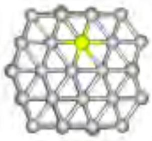 $Pd_{93}Au_5$ 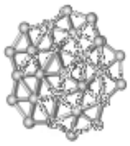 Pd_{98}

Figure 4.2. Structural motifs for selected Pd_mAu_{98-m} clusters using the DFT-fit Gupta potential.

Outside this range, several other structural families such as Ino-Decahedron (Ino-Dh) (e.g. $Pd_{14}Au_{84}$), Ino-Icosahedron (In-Ico) (e.g $Pd_{21}Au_{77}$), FCC (e.g. Pd_1Au_{97}) and FCC-HCP (e.g. $Pd_{93}Au_5$) can also be encountered (all exemplified in Figure 4.2). For pure clusters, the motifs are as follows: Au_{98} is FCC-HCP and Pd_{98} is characterized by a M-Dh structure (Figure 4.2).

Table 4.3. Structure types for Pd_mAu_{98-m} clusters obtained with the DFT-fit Gupta potential.

m	Structure	m	Structure	m	Structure
0	FCC-HCP	**33**	M-Dh	**66**	Dh
1	FCC	**34**	M-Dh	**67**	M-Dh
2	Dh	**35**	Dh	**68**	Dh
3	FCC-HCP	**36**	M-Dh	**69**	M-Dh
4	FCC-HCP	**37**	M-Dh	**70**	M-Dh
5	FCC-HCP	**38**	M-Dh	**71**	M-Dh
6	M-Dh	**39**	M-Dh	**72**	M-Dh
7	M-Dh	**40**	Dh	**73**	M-Dh
8	M-Dh	**41**	M-Dh	**74**	Dh
9	In-Ico	**42**	M-Dh	**75**	Dh
10	M-Dh	**43**	M-Dh	**76**	In-Ico
11	M-Dh	**44**	M-Dh	**77**	Dh
12	M-Dh	**45**	M-Dh	**78**	M-Dh
13	M-Dh	**46**	M-Dh	**79**	M-Dh
14	Dh	**47**	In-Ico	**80**	Dh
15	M-Dh	**48**	M-Dh	**81**	M-Dh
16	M-Dh	**49**	M-Dh	**82**	M-Dh
17	Dh	**50**	M-Dh	**83**	M-Dh
18	Dh	**51**	Dh	**84**	M-Dh
19	Dh	**52**	M-Dh	**85**	Dh
20	Dh	**53**	Dh	**86**	M-Dh
21	In-Ico	**54**	M-Dh	**87**	Dh
22	In-Ico	**55**	M-Dh	**88**	M-Dh
23	In-Ico	**56**	In-Ico	**89**	M-Dh
24	Dh	**57**	M-Dh	**90**	FCC-HCP
25	In-Ico	**58**	M-Dh	**91**	M-Dh
26	M-Dh	**59**	M-Dh	**92**	FCC-HCP
27	M-Dh	**60**	M-Dh	**93**	FCC-HCP
28	M-Dh	**61**	M-Dh	**94**	Dh
29	Dh	**62**	M-Dh	**95**	M-Dh
30	M-Dh	**63**	M-Dh	**96**	M-Dh
31	M-Dh	**64**	M-Dh	**97**	Dh
32	Dh	**65**	Dh	**98**	M-Dh

The GA global optimization using the DFT-fit Gupta potential tends to find clusters with a high degree of mixing between Au and Pd. This is discussed in more detail in Section 4.4.2, where an analysis of the number of heteronuclear and homonuclear bonds is made for each potential for the compositional range $Pd_{46}Au_{52}$-$Pd_{52}Au_{46}$.

B) Gupta potential with Exp-fit parameters

The Exp-fit excess energy curve is shown in red in Figure 4.1. The curves for Exp-fit and DFT-fit potential are similar. The composition for which the excess energy is minimum is $Pd_{52}Au_{46}$, with an In-Ico geometry (Figure 4.3). In contrast to the DFT-fit potential the Exp-fit potential offers a higher degree of structural variety.

Gupta potential	
Exp-fit	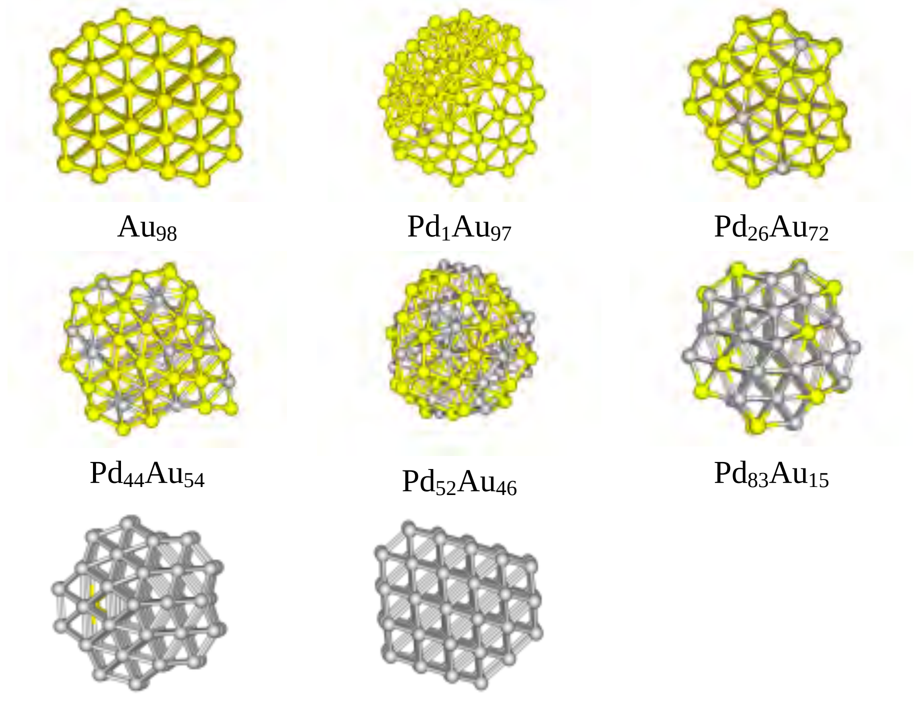 Au_{98} Pd_1Au_{97} $Pd_{26}Au_{72}$ $Pd_{44}Au_{54}$ $Pd_{52}Au_{46}$ $Pd_{83}Au_{15}$ $Pd_{97}Au_1$ Pd_{98}

Figure 4.3. Structural motifs found for selected Pd_mAu_{98-m} clusters using the Exp-fit Gupta potential.

Table 4.4. Structure types for Pd_mAu_{98-m} nanoparticles obtained with the Exp-fit Gupta potential.

m	**Structure**	**m**	**Structure**	**m**	**Structure**
0	FCC-HCP	**33**	M-Dh	**66**	In-Ico
1	In-Ico	**34**	M-Dh	**67**	In-Ico
2	FCC-HCP	**35**	Dh	**68**	In-Ico
3	Dh	**36**	M-Dh	**69**	In-Ico
4	In-Ico	**37**	FCC-HCP	**70**	In-Ico
5	FCC-HCP	**38**	In-Ico	**71**	In-Ico
6	In-Ico	**39**	M-Dh	**72**	In-Ico
7	M-Dh	**40**	M-Dh	**73**	In-Ico
8	FCC-HCP	**41**	M-Dh	**74**	In-Ico
9	FCC-HCP	**42**	Dh	**75**	In-Ico
10	In-Ico	**43**	M-Dh	**76**	In-Ico
11	In-Ico	**44**	Dh	**77**	In-Ico
12	Dh	**45**	In-Ico	**78**	In-Ico
13	In-Ico	**46**	M-Dh	**79**	In-Ico
14	Dh	**47**	M-Dh	**80**	In-Ico
15	In-Ico	**48**	In-Ico	**81**	In-Ico
16	In-Ico	**49**	In-Ico	**82**	Dh
17	M-Dh	**50**	In-Ico	**83**	M-Dh
18	M-Dh	**51**	Dh	**84**	In-Ico
19	Dh	**52**	In-Ico	**85**	M-Dh
20	FCC	**53**	In-Ico	**86**	Dh
21	In-Ico	**54**	In-Ico	**87**	Dh
22	Dh	**55**	In-Ico	**88**	M-Dh
23	FCC-HCP	**56**	In-Ico	**89**	Dh
24	M-Dh	**57**	In-Ico	**90**	Dh
25	M-Dh	**58**	In-Ico	**91**	Dh
26	Dh	**59**	In-Ico	**92**	M-Dh
27	M-Dh	**60**	In-Ico	**93**	FCC-HCP
28	M-Dh	**61**	In-Ico	**94**	FCC-HCP
29	Dh	**62**	In-Ico	**95**	M-Dh
30	M-Dh	**63**	Dh	**96**	M-Dh
31	Dh	**64**	In-Ico	**97**	M-Dh
32	In-Ico	**65**	In-Ico	**98**	Dh

A transition from In-Ico to Dh appears on the left side of the minimum excess energy curve, (i.e. biased towards pure Au), from $Pd_{47}Au_{51}$ to $Pd_{24}Au_{64}$, with exceptions like $Pd_{32}Au_{66}$, $Pd_{45}Au_{53}$ and $Pd_{37}Au_{61}$, with an FCC-HCP structure (see Table 4.4). The pure clusters, Au_{98} and Pd_{98} have an FCC-HCP and FCC-like geometries, all exemplified in Figure 4.3 along with other interesting structural motifs.

C) Gupta Potential with Average parameters

The excess energy for the Average potential is plotted in Figure 4.1, green curve. Compared with the fitted potentials, the values of the excess energies are noticeably less negative and the shape of the curve is quite different.

Gupta Potential	
Average	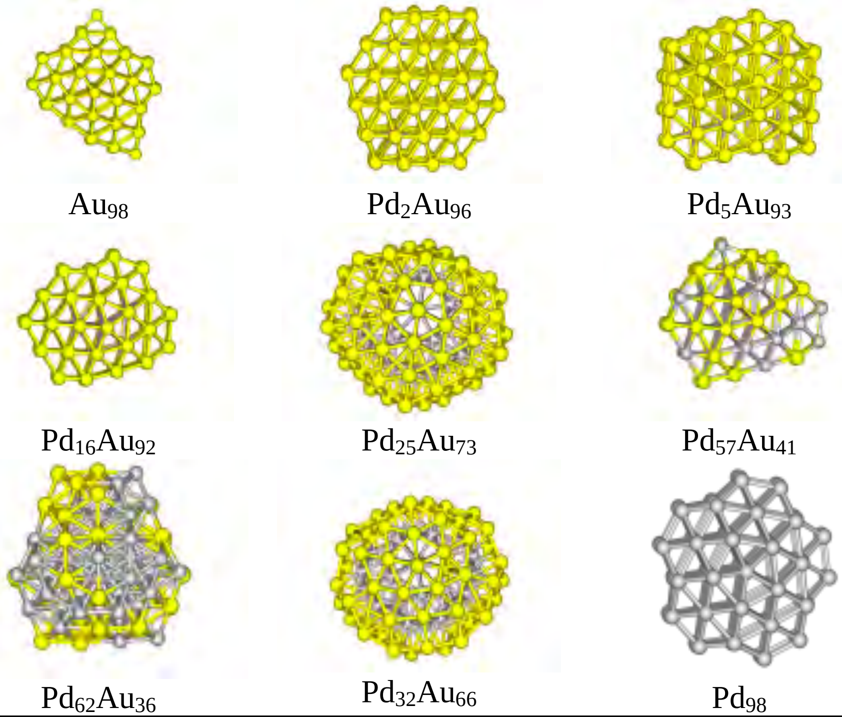 Au_{98} Pd_2Au_{96} Pd_5Au_{93} $Pd_{16}Au_{92}$ $Pd_{25}Au_{73}$ $Pd_{57}Au_{41}$ $Pd_{62}Au_{36}$ $Pd_{32}Au_{66}$ Pd_{98}

Figure 4.4. Structural motifs found for selected Pd_mAu_{98-m} clusters using the Average Gupta potential

Table 4.5. Structure types for Pd_mAu_{98-m} clusters obtained with the Average Gupta potential

m	Structure	m	Structure	m	Structure
0	Dh	**33**	In-Ico	**66**	M-Dh
1	M-Dh	**34**	Dh	**67**	M-Dh
2	FCC	**35**	In-Ico	**68**	M-Dh
3	M-Dh	**36**	In-Ico	**69**	M-Dh
4	In-Ico	**37**	In-Ico	**70**	In-Ico
5	FCC-HCP	**38**	In-Ico	**71**	M-Dh
6	FCC	**39**	In-Ico	**72**	M-Dh
7	FCC-HCP	**40**	Dh	**73**	Dh
8	M-Dh	**41**	In-Ico	**74**	M-Dh
9	FCC-HCP	**42**	Dh	**75**	M-Dh
10	Dh	**43**	In-Ico	**76**	M-Dh
11	M-Dh	**44**	In-Ico	**77**	FCC-HCP
12	Dh	**45**	M-Dh	**78**	M-Dh
13	Dh	**46**	M-Dh	**79**	Dh
14	Dh	**47**	M-Dh	**80**	Dh
15	Dh	**48**	M-Dh	**81**	Dh
16	Dh	**49**	M-Dh	**82**	M-Dh
17	Dh	**50**	M-Dh	**83**	Dh
18	Dh	**51**	In-Ico	**84**	Dh
19	Dh	**52**	Dh	**85**	M-Dh
20	Dh	**53**	M-Dh	**86**	M-Dh
21	In-Ico	**54**	M-Dh	**87**	M-Dh
22	In-Ico	**55**	Dh	**88**	Dh
23	Dh	**56**	Dh	**89**	M-Dh
24	In-Ico	**57**	Dh	**90**	Dh
25	In-Ico	**58**	In-Ico	**91**	M-Dh
26	Dh	**59**	Dh	**92**	Dh
27	In-Ico	**60**	Dh	**93**	M-Dh
28	In-Ico	**61**	M-Dh	**94**	In-Ico
29	In-Ico	**62**	In-Ico	**95**	M-Dh
30	In-Ico	**63**	M-Dh	**96**	FCC-HCP
31	In-Ico	**64**	M-Dh	**97**	M-Dh
32	In-Ico	**65**	In-Ico	**98**	M-Dh

The composition for which the excess energy is minimum is $Pd_{32}Au_{66}$, with an In-Ico geometry (Figure 4.4). This is an interesting structure, as the 32 Pd atoms sit in the centre of the cluster, surrounded by a shell of 66 Au atoms. Also, by examining Table 4.5, we can notice that Dh clusters are encountered predominantly for Pd rich compositions, and there is a trend to In-Ico clusters for Au rich compositions, with exceptions (e.g. $Pd_{26}Au_{62}$, $Pd_{40}Au_{58}$, $Pd_{42}Au_{56}$, etc., which are all Dh. Other interesting structural motifs have been identified, such as FCC-HCP (e.g. $Pd_{9}Au_{89}$), FCC (e.g. $Pd_{6}Au_{92}$). The pure clusters, Au_{98} and Pd_{98} respectively have a Dh and M-Dh structure respectively, all exemplified in Figure 4.4).

As observed from Figure 4.4, as we increase the concentration of Au atoms in clusters, Au tends to occupy surface sites, forming patches distributed over the clusters' surface. An interesting motif is found for $Pd_{62}Au_{36}$ which has a structure based on a rearrangement of a fragment of the Leary Tetrahedron.

4.4.2. Determination of number of homonuclear and heteronuclear bonds

As shown earlier, the fitted potentials (Gupta DFT-fit and Exp-fit) tend to offer a larger degree of segregation between Au and Pd in comparison with the Average potential. This is confirmed by the quantification of the number of homonuclear and heteronuclear bonds, as shown in Table 4.6. By examining Table 4.6, over the studied compositional range ($Pd_{46}Au_{52}$-$Pd_{52}Au_{46}$), we can notice that the number of Pd-Pd and Au-Au bonds are maximized for the Average potential relative to the fitted potentials.

Table 4.6. Number of heteronuclear and homonuclear bonds for the GM structures in the interval $Pd_{46}Au_{52}$-$Pd_{52}Au_{46}$ for the Gupta Average, DFT-fit and Exp-fit potentials.

Gupta Potential	**$Au_{46}Pd_{52}$**	**$Au_{47}Pd_{51}$**	**$Au_{48}Pd_{50}$**	**$Au_{49}Pd_{49}$**	**$Au_{50}Pd_{48}$**	**$Au_{51}Pd_{47}$**	**$Au_{52}Pd_{46}$**
Average							
Au-Au	206	194	180	174	166	156	152
Pd-Au	318	322	332	328	326	324	334
Pd-Pd	332	340	344	354	364	376	370
DFT-fit							
Au-Au	154	150	138	140	130	120	122
Pd-Au	462	454	470	476	444	492	458
Pd-Pd	240	252	248	240	282	244	276
Exp-fit							
Au-Au	174	160	162	170	166	148	148
Pd-Au	476	478	456	418	442	402	402
Pd-Pd	204	218	238	282	266	324	324

This can be directly linked to the values of the Gupta parameters emphasized in Table 4.2. As shown here, the Exp-fit potential has a pair (repulsive) energy scaling parameter (A) that is larger for Pd-Au than for either Pd-Pd or Au-Au. Previously, for Pd-Pt clusters, this has been shown to favour layer segregation [22].

However, this potential also has a larger value of the many body energy scaling parameter, ξ, which is greatest for Pd-Au, favouring heteronuclear mixing [4]. The value of the ξ parameter will eventually dominate, such that the fitted potentials should favour more Pd-Au mixing.

4.4.3. Leary Tetrahedron (LT) clusters

As shown previously [21], the LT is difficult to find using the GA. For the case of PdPt clusters, this is typically found about in 1% of the cases. This is probably due to the existence of a narrower, but deeper potential energy basin for the LT structures. The shell program (Chapter II) constrains the structure to be LT such that, if the shell routine finds, for a given composition, a LT isomer lower in energy than the structures found by the GA, it shows that the GA did not find the right structure.

As it has been shown in the previous sections, the GA has not been able to identify any LT structures, irrespective of the type of potential used to model inter-atomic interactions. As seen in our analysis and also mentioned in Refs. [2, 8], there is a preferential funnelling towards structures such as M-Dh, Ico as GM structures, and a lack of funnelling towards the LT GM in the PES.

This has been previously described in the paper of Leary and Doye (Ref. [8]) for 98-atom Lennard-Jones (LJ_{98}) clusters, where, by using a modified version of the BHMC algorithm, the LT has been found in approximately 10% of cases.

Possibly, there could be a lower structure – or even a lower-symmetry LT by switching the positions of unlike atoms, a possibility that has been tested by applying the BHMC algorithm with exchange-only moves, for the case of 98-atom PdPt clusters, as shown in Ref. [21]. However, for the case of 98-atom AuPd clusters, when both the GA and BHMC algorithm encounter similar difficulties in funnelling towards structures such as the LT, it is possible that this could be directly related to the topography of the PES.

Step-by-step construction of the Leary Tetrahedron

The 98-atom LT has been described by Leary and Doye [8]. It consists of [2]:

- a 20-atom central tetrahedron with a high proportion of (111) facets
- each of the (111) facets has a truncated tetrahedron built on them, forming a 56-atom stellated tetrahedron
- six centred hexagonal patches are places on the original tetrahedron, decorating the closed-packed surfaces of the original tetrahedron, generating the high-symmetry LT.

The step-by-step construction is shown below:

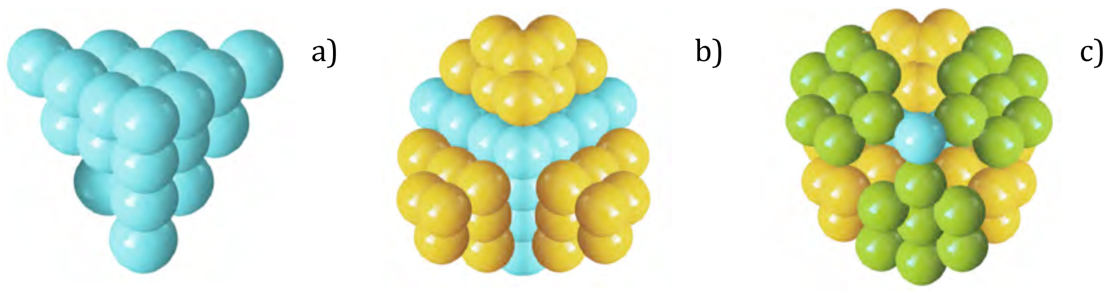

Figure 4.5. Step by step construction of the LT structure: a) 20-atom central tetrahedron with high proportion of (111) facets; b) 56-atom stellated tetrahedron built on the original 20-atom tetrahedron; c) the complete Leary tetrahedron structure. Adapted after Ref. [2].

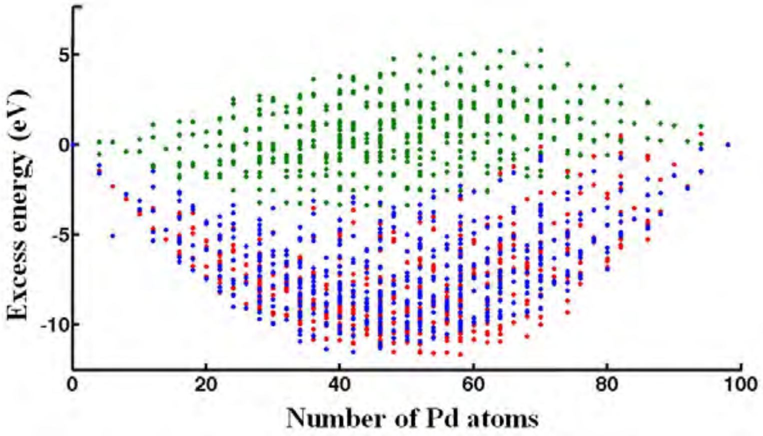

Figure 4.6. Plot of the LT excess energy as a function of Pd content for the high symmetry 98-atom AuPd clusters modelled by Gupta DFT-fit (blue dots), Exp-fit (red dots) and Average (green dots) potentials.

As described in Ref. [8], the LT, with its quasi-spherical shape, the core, fcc-packing and the high proportion of the (111) facets offers a better atomic arrangement for medium sized-clusters, with 432 nearest neighbours, compared to other structural motifs. The excess energy curve for the LT as a function of number of Pd atoms in clusters is emphasized in Figure 4.6 for Gupta DFT-fit (blue dots), Exp-fit (red dots) and Average (green dots).

4.4.4. DFT local relaxation

GM structures found at the EP level for compositions $Pd_{46}Au_{52}$-$Pd_{52}Au_{46}$ were relaxed at the DFT level. The variation of the excess energy as a function of Pd content is shown in Figure 4.7 for isomers obtained with: Gupta DFT-fit (blue line), Exp-fit (red line) and Average (green line). The plot of the excess energy in Figure 4.7 is rather jagged, especially with the isomers produced by the DFT-fit and Exp-fit potentials. In Figure 4.7 it is visible that the Average potential has lead to values of the excess energies more negative than the case of the isomers obtained with the DFT-fit and Exp-fit potentials, with few exceptions (e.g. $Pd_{46}Au_{52}$ for which the DFT isomer is lower and $Pd_{51}Au_{47}$ for which the Exp-fit isomer is lower). The reason why this is happening is that the Average potential favours $Pd_{core}Au_{shell}$ isomers, in contrast with the Exp-fit and DFT-fit isomers, who prefer more mixed configurations.

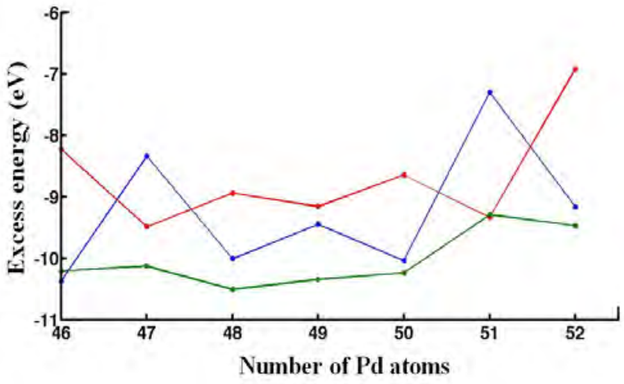

Figure 4.7. DFT relaxation for the ‘putative’ GM for the DFT-fit (blue line), Exp-fit (red line) and Average (green line) Gupta potentials. The compositional interval is $Pd_{46}Au_{52}$-$Pd_{52}Au_{46}$.

This has also been supported by our calculation of the number of heteronuclear and homonuclear bonds for each potential, in Table 4.6. The isomers of the DFT-fit, Exp-fit and Average potentials, after DFT relaxations, are shown in Figure 4.8.

We can conclude that the DFT-fit and Exp-fit potentials are overestimating the stability of the mixed isomers relative to the DFT calculations.

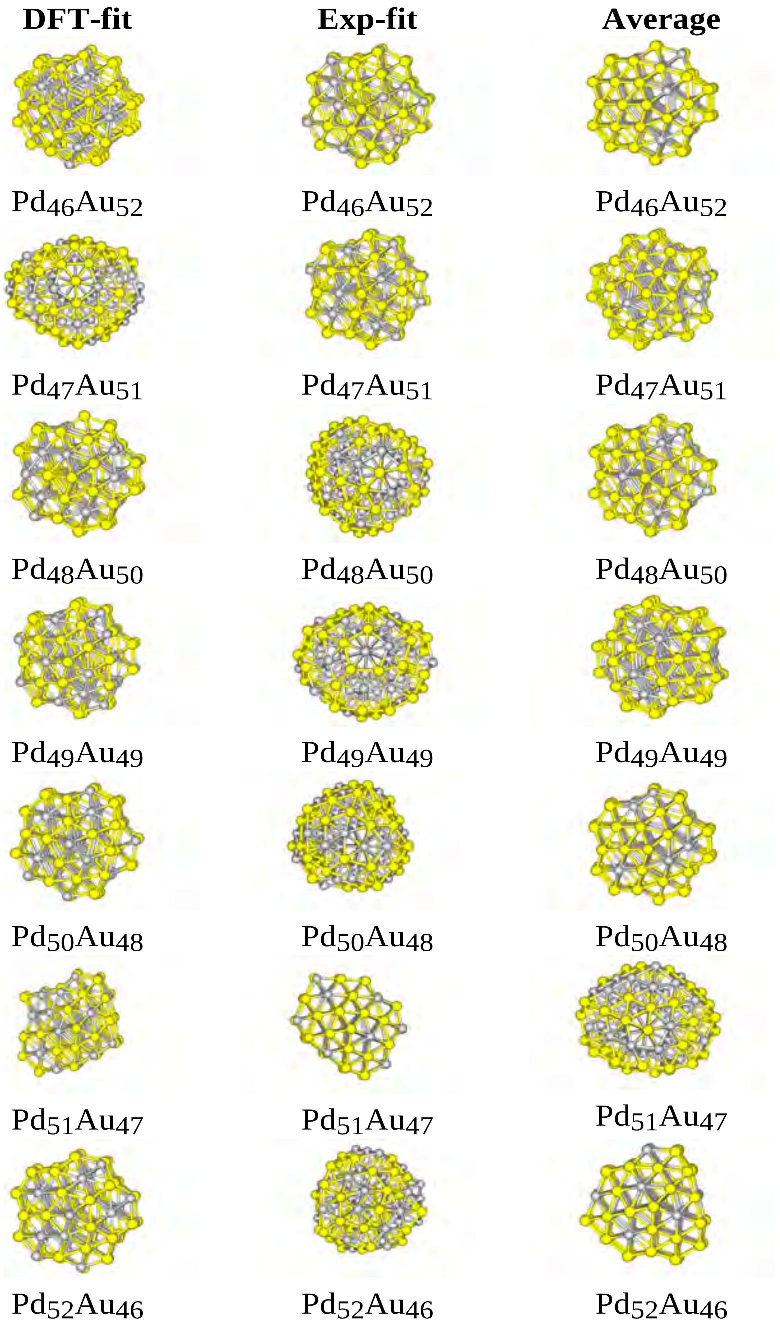
DFT-fit
Exp-fit
Average
$Pd_{46}Au_{52}$
$Pd_{46}Au_{52}$
$Pd_{46}Au_{52}$
$Pd_{47}Au_{51}$
$Pd_{47}Au_{51}$
$Pd_{47}Au_{51}$
$Pd_{48}Au_{50}$
$Pd_{48}Au_{50}$
$Pd_{48}Au_{50}$
$Pd_{49}Au_{49}$
$Pd_{49}Au_{49}$
$Pd_{49}Au_{49}$
$Pd_{50}Au_{48}$
$Pd_{50}Au_{48}$
$Pd_{50}Au_{48}$
$Pd_{51}Au_{47}$
$Pd_{51}Au_{47}$
$Pd_{51}Au_{47}$
$Pd_{52}Au_{46}$
$Pd_{52}Au_{46}$
$Pd_{52}Au_{46}$

Figure 4.8. Structures of AuPd clusters (generated as GM for the three Gupta potentials in the interval $Pd_{46}Au_{52}$-$Pd_{52}Au_{46}$), after DFT relaxation and before the optimization of chemical ordering.

4.4.5. Optimization of chemical ordering and DFT relaxations

Figures 4.9 (a)-(c) show the excess energy for four different structural motifs after the optimization of the chemical ordering using BHMC. The four structural motifs are: LT (black line), M-Dh (green line), Ico (red line) and FCC-HCP (blue line).

For compositions for which these structural motifs have not been found by GA and BHMC, these have been generated and subsequently subjected to BHMC atom exchange in order to optimize the chemical ordering.

We have then performed DFT local relaxations on the optimized isomers obtained with the Average potential (see Figure 4.10 and Table 4.7 for the values of the excess energy for each motif). This is justified because the Average potential has earlier shown to yield isomers with the lowest excess energy values after relaxation at the DFT level (see Figure 4.9).

It is interesting to see that, in Figure 4.9, at the EP level, for the DFT-fit and the Exp-fit potentials there is a close competition between the FCC-HCP and M-Dh motifs which are significantly lower in energy than the LT motifs by approximately 0.3 eV. The order is however reversed for the Average potential (see Figure 4.9 (c)) for which the LT isomers are competitive with M-Dh but are much lower in energy by 0.3 eV or more than FCC-HCP.

DFT relaxations of the structural motifs optimized for the Average potential leads to a change in the stability order, with the lowest excess energies now belonging to the FCC-HCP and M-Dh motifs. It is quite clear that the LT motif is de-stabilized at the DFT level compared with FCC-HCP and M-Dh structures, although it is still less considerably lower in energy than the Ico structures.

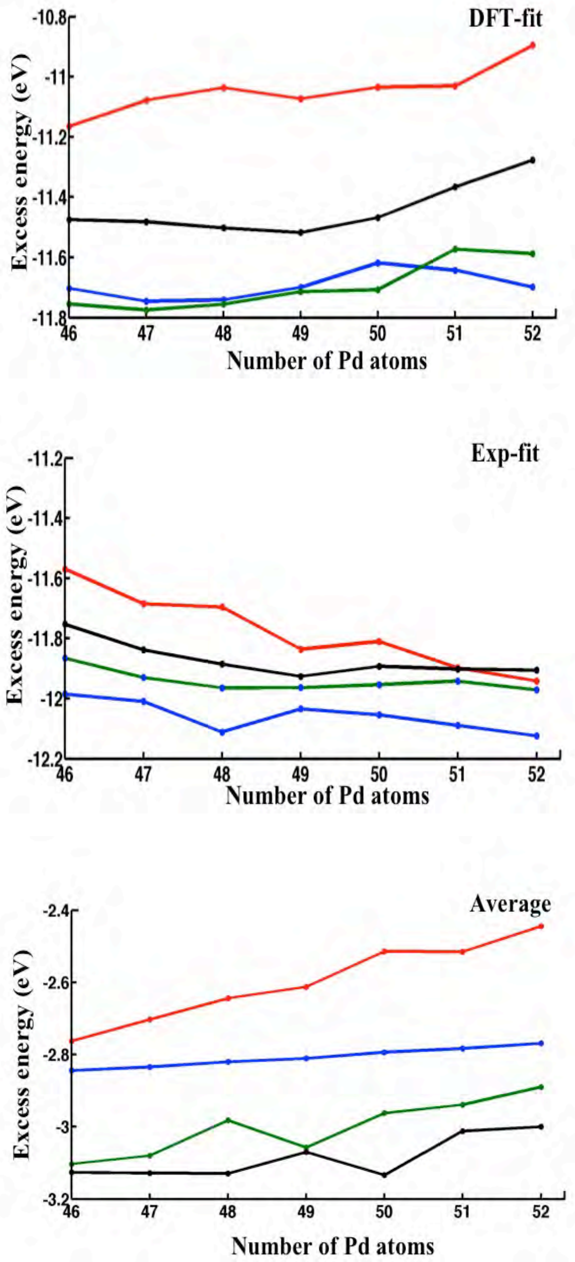

Figure 4.9. Excess energy plot comparing LT (black line), M-Dh (green line), Ico (red line) and FCC-HCP (blue line) structural motifs in the compositional range $Pd_{46}Au_{52}$-$Pd_{52}Au_{46}$; (a)-(c) results of BHMC chemical ordering optimization for Gupta DFT-fit, Gupta Exp-fit and Gupta Average potentials.

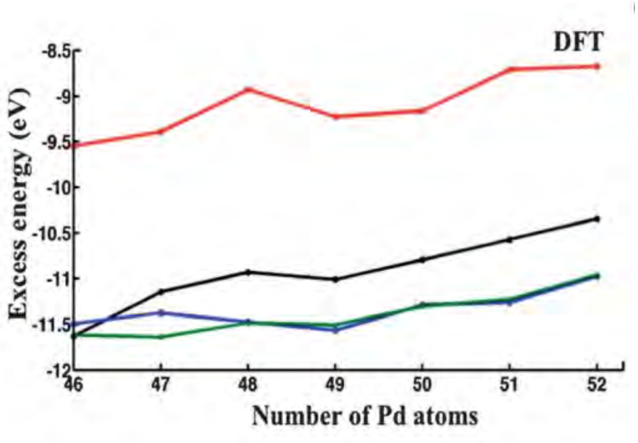

Figure 4.10. Excess energy of LT (black line), M-Dh (green line), Ico (red line) and FCC-HCP (blue line) obtained with the Average potential. The plot represents the relaxation of these structural motifs at the DFT level, after the optimization of the chemical ordering.

Table 4.7. Excess energies (eV) for various structural motifs obtained for the Average potential (after BHMC homotop optimization) and subsequently relaxed at the DFT level.

Composition	Leary Tetrahedron	FCC-HCP	Icosahedron	Marks Decahedron
Pd$_{46}$Au$_{52}$	-11.6273	-11.4923	-9.5497	-11.6147
Pd$_{47}$Au$_{51}$	-11.1456	-11.3739	-9.3903	-11.6383
Pd$_{48}$Au$_{50}$	-10.9303	-11.4708	-8.9275	-11.4839
Pd$_{49}$Au$_{49}$	-11.0112	-11.5620	-9.2246	-11.5060
Pd$_{50}$Au$_{48}$	-10.7925	-11.2877	-9.1592	-11.3032
Pd$_{51}$Au$_{47}$	-10.5726	-11.2604	-8.7121	-11.2280
Pd$_{52}$Au$_{46}$	-10.3450	-10.9750	-8.6772	-10.9586

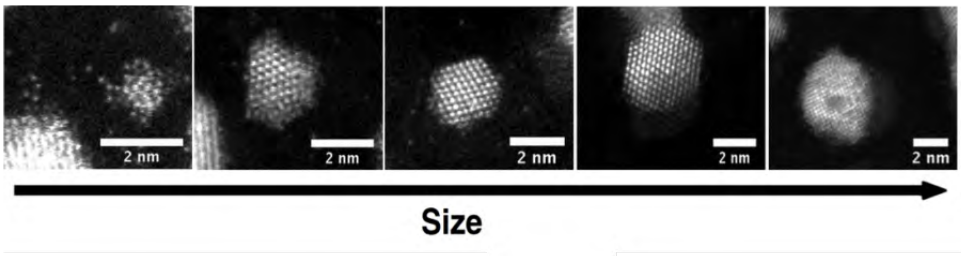

Figure 4.11. Structural evolution with size of AuPd nanoparticles deposited via physical vapour deposition on amorphous carbon substrate and annealed for 473 K for 2 hours. Various morphologies of AuPd nanoparticles can be observed as size increases, from alloy to Janus structures.

This theoretical prediction can be directly linked to our experimental study of evaporated AuPd nanoparticles (Figure 4.11), where structural motifs such as FCC are commonly encountered, whereas LT structures have not been yet observed for AuPd nanoparticles.

4.5. Conclusions

Three parameters sets (DFT-fit, Exp-fit and Average) have been taken under study for the Gupta potential in order to investigate the structure and energetics of 98-atom AuPd nanoclusters. An extensive search of the configurational space has been made using a genetic algorithm, in order to identify global minimum clusters for all three Gupta potentials, at the DFT level. It was found that the fitted potentials (DFT-fit and Exp-fit) favour a higher degree of mixing between Au and Pd in contrast to the Average potential, that tends to favour $Pd_{core}Au_{shell}$ configurations. This is in good agreement with the DFT calculations, which stabilizes core-shell configurations. A shell optimization program has been employed for the generation of the high-symmetry Leary Tetrahedron which have been found to be the most stable motif for the Average potential. However, Basin Hopping Monte Carlo optimization of the homotops of a number of low energy structures followed by DFT local relaxations destabilize the LT, favouring other structural motifs such as FCC-HCP and Marks Decahedron.

Bibliography

---

[1] Paz-Borbon, L. O., Johnston, R. L., Barcaro. G., Fortunelli, A., *J. Chem. Phys*, 128, 124517, **2008**.

[2] Paz-Borbon, L. O., *Computational Studies of Transition Metals Nanoalloys,* Springer Theses, Berlin, **2011**.

[3] Ascensio, J., Liu, H. B., Pal, U., Perez, R. J., *Phys. Chem. B*, 110, 5191, **2006**.

[4] Pittaway, F., Paz-Borbon, L. O., Johnston, R. L., Arslan, H., Ferrando, R., Mottet, C., Barcaro, G., Fortunelli, A., *J. Phys. Chem. C.*, 113, 9141, **2009**.

[5] Yuan, D. W., Gong, X. G., Wu, R., *Phys. Rev. B.*, 75, 085428, **2007**.

[6] Ferrando, R., Fortunelli, A., Rossi, G., *Phys. Rev. B.*, 72, 085449, **2005**.

[7] Paz-Borbon, L. O., Mortimer-Jones, T. V., Johnston, R. L., Posada-Amarillas, A., Barcaro, G., Fortunelli, A., *Phys. Chem. Chem. Phys*., 9, 5202, **2007**.

[8] Leary, R. H., Doye, J. P. K., *Phys. Rev. E,* 60, R6320, **1999**.

[9] Johnston, R. L., *Dalton Trans*., 2, 4193, **2003**.

[10] Doye, J., Wales, D., *J. Phys. Chem. A*, 101, 5111, **1997**.

[11] Rossi, G., Ferrando, R. in *Nanomaterials: Design and Fabrication*, Elsevier, Amsterdam, **2007**.

[12] Schmid, G., Lehnert, A., Malm, J. O., Bovin, J. O., *Angew. Chem. Int. Ed. Engl*., 30, 874, **1991**.

[13] Lee, A. F., Baddley, C. J., Hardcare, C., Orneord, R. M., Lambert, R. M., Schmid, G., West, H., *J. Phys. Chem*., 99, 6096, **1995**.

[14] Gianozzi, P., Baroni, S., Bnini, N., Calandra, M., Car, R., Cavazzoni, C., Ceresoli, D., Chiarotti, G. L., Cococcioni, M., Dabo, I., Corso, A. D., De Gironcoli, D., Fabris, S., Fratesi, G., Gebauer, R., Gertsman, U., Gougoussis, C., Kokalj, A., Lazzeri, M., Martin-Samos, L.,

---

Marzari, N., Mauri, F., Mazarello, R., Paolini, S., Pasquarello, A., Paulatto, L., Sbraccia, C., Scandolo, S., Sclauzero, G., Seitsonen, A., Smogunov, A., Umari, P., Wentzcovich, R. M., *J. Phys.:Condens. Matter*., 21, 395502, **2009**.

[15] Perdew, J. B., Burke, K., Ernzernhof, M., *Phys. Rev. Lett*., 77, 3865, **1996**.

[16] http://www.bluebear.bham.ac.uk

[17] Ismail, R., Johnston, R. L., *Phys. Chem Chem. Phys*., 12, 8607, **2010**.

[18] Cleri, F., Rosato, V., *Phys. Rev. B*, 22, 48, **1993**.

[19] Pitttaway, F., Paz-Borbon, L. O., Johnston, R. L., Arslan, H., Ferrando, R., Mottet, C., Barcaro, G., Fortunelli, A., *J. Phys. Chem. C*, 113, 9141, **2009**.

[20] Hultgren, R., Desai, P. D., Hawkins, D. T., Gleiser, M., Kelley, K. K., *Values of the thermodynamic properties of binary alloys,* American Society for Metals, Jossey-Bass Publishers, Berkeley, **1981**.

[21] Paz-Borbon, L. O., Johnston, R. L., Barcaro, G., Fortunelli, A., *J. Chem. Phys*., 128, 134517, **2008**.

[22] Massen, C., Mortimer-Jones, T., Johnston, R. L., *J. Chem. Soc. Dalton Trans*., 23, 4375, **2002**.

Chapter V

Direct atomic imaging and density functional theory study of the $Au_{24}Pd_1$ cluster catalyst

5.1. Overview

This chapter is focusing on the characterization of single Pd doped Au_{25} clusters supported on Multiwall Carbon Nanotubes (MWCNTs) by means of experimental and theoretical studies.

The interest in the investigation of structural properties and applications of the 25-atom Au systems arose since the report published by Brust et al. [1], where thiolate protected Au_{25} clusters were first synthesized. This system has attracted considerable attention ever since, due to its unique chemical and thermodynamic stability in comparison with clusters of other sizes [2-4]. Many experimental studies focused on the analysis of the 25-atom Au system have revealed that these systems exhibit properties such as photoluminescence [5, 6] and paramagnetism [7].

Doping Au nanoclusters with foreign metals provides a viable approach to modify the chemical, electronic and optical properties of the parent cluster [8, 9]. For example, platinum doped Au clusters have attracted major research interest due to their important applications in the domain of nanocatalysis [10-13], especially for their enhanced selectivity towards various low temperature oxidation reactions. Au and Pd are interesting candidates because their cohesive energies are very similar, and therefore, a high degree of miscibility can be expected at the nanoscale. Indeed, it has been shown that larger AuPd nanoparticles (~ 10 nm) show a high degree of miscibility and a tendency to form mixed or core-shell configurations [14, 15]. However, it has been well established that small nanoparticles (10-20 atoms) are more suitable catalysts than larger nanoparticles [16]. For this size regime, the properties of small metallic nanoparticles can be modified considerably by doping the nanoclusters with just one foreign atom [10].

While physical synthesis techniques have a good control over the size distribution of metallic nanoparticles [10], a robust control of the size distribution for chemically synthesized metallic ligand protected nanoclusters is still a challenging issue. Improvements brought to the chemical synthesis method developed by Brust et al. [1] and advances in the nanoparticles structure determination using single crystal X-ray diffraction for the thiolate protected Au_{25} nanoclusters [17] have brought a breakthrough in the research field regarding small chemically synthesized metallic nanoparticles [2,4].

The doped nanoparticles not only have an enhanced electronic structure and better applications in fields like nanocatalysis, but are also more stable than the monometallic parent clusters. As shown in Refs. [18, 23], the $Au_{24}Pd_1$ cluster has a considerably increased resistance to degradation in solution and laser dissociation when compared to the ligand protected Au_{25} clusters.

DFT calculations on ligand (thiolate) protected $Au_{24}Pd_1$ nanoclusters have predicted several properties of this system:

- The most stable structure of the ligand protected cluster is a core-shell configuration [19, 20]
- Doping the nanoclusters with Pd will increase its thermodynamic stability [21].

However, the theoretical analyses mentioned above are lacking a thorough global optimization method to identify the global minimum (GM) structure. Global optimization methods are still a challenging issue for nanoparticles with a number of atoms up to 50. Moreover, theoretical analysis is significantly complicated for bimetallic nanoparticles, as discussed in detail in Chapter II, as the number of homotops increases combinatorially with cluster size [22].

A recent experimental study of the $Au_{24}Pd_1$ system has shown that the ligand-free doped clusters have 54% more rate of conversion towards the aerobic oxidation of benzyl alcohol in comparison with their monometallic counterparts [23]. The analysis of the purity of the compounds is based on the Matrix Assisted Laser Desorption Ionization (MALDI) Time of Flight (TOF) mass spectrometry and the structural analysis has been based on High Resolution Transmission Electron Microscopy (HR-TEM).

The TEM analysis reported in Ref. [23] is limited to an *average* diameter analysis. Although the analysis provides evidence that the clusters have a good size control, it was unable to explain the catalytic activity of doped Au clusters and the role of the Pd dopant as either a direct reaction site or as an indirect electron promoter for the surrounding Au atoms. Predictions based on previous DFT calculations of Au_nPd_1 clusters (where n=54, 78, 91 and 97 atoms) [24], as well as thermodynamic considerations [25] were taken into account in order to estimate, indirectly, the position of the Pd dopant in the cluster.

In this study, we take a combined experimental and computational approach to investigate in detail the ligand-free $Au_{24}Pd_1$ clusters supported on MWCNTs. Experimentally, the aberration-corrected STEM has been employed to obtain atomic-scale structural information of the clusters, in terms of their size and 3D morphology. In particular, efforts have been made in performing quantitative and statistical analysis of the clusters to get information regarding the total number of atoms within the clusters.

A theoretical analysis is also performed, for the determination of the structure and energetics of the global minimum (GM) $Au_{24}Pd_1$ cluster, using a hybrid Basin Hopping Monte Carlo (BHMC) DFT analysis. Finally, the charge transfer was investigated, by performing the Löwdin population analysis, in order to observe the changes induced by the Pd dopant in the electronic structure of the clusters. Wherever possible, we try to link the experimental results with that of the calculations.

The results of this chapter have been accepted for publication in *Nanoscale*: Bruma, A., Negreiros, F., Xie, S., Tsukuda, T., Fortunelli, A., Li, Z. Y., "*Direct imaging and density functional theory study of the* $Au_{24}Pd_1$ *cluster catalyst*", DOI: 10.1039/C3NR01852K, 2013.

5.2. Quantitative Z-contrast imaging

This section describes experiment conducted for the determination of the α exponent in the relation $I \sim Z^{\alpha}$ using single Au and Pd atoms. This is a method that offers a good degree of accuracy for determining the integrated intensity of bimetallic systems [26, 27] and for estimating the number of atoms in clusters.

The image contrast in HAADF-STEM is a function of various parameters such as: (i) sample thickness [28-30], (ii) specimen orientation [31], (iii) value of inner collection angle [31]. The HAADF-STEM is also known as Z-contrast imaging, as the image contrast in HAADF-STEM scales with Z^{α}, where Z is the atomic number of the material and the exponent α takes values within the interval $1.4 < \alpha < 2$, with a pure Rutherford scattering for α =2 [32].

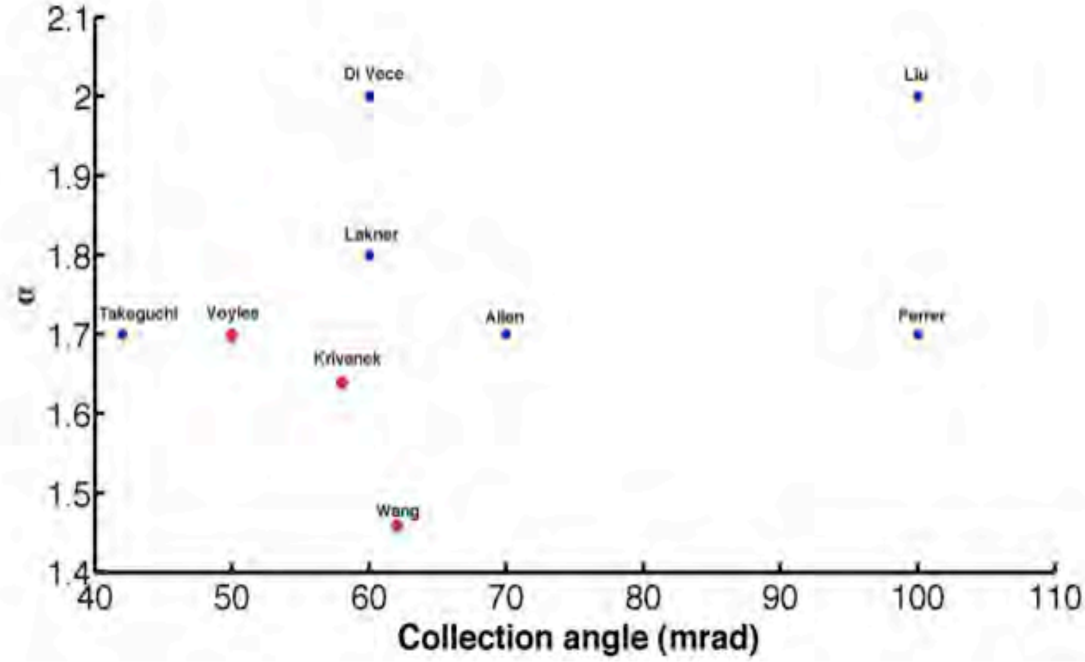

Figure 5.1. Estimated exponent α in the relationship $I \sim kZ^{\alpha}$ between annular dark-field intensity I and atomic number Z as a function of the collection angle admitted by the detectors. (●) Without calibration analysis; (●) With calibration analysis. Names in the plot refer to the first authors of the corresponding references: Ferrer et al. [26], Kirvanek et al. [27], Wang et al. [39], Voyles et al. [33], Takeguchi et al. [34], Lakner et al. [35], Di Vece et al. [36], Allen et al. [37], Liu et al. [38].

For quantitative analysis of the HAADF-STEM image contrast, one needs to know the value of α. Currently, the values of the α exponent reported in the literature are dispersed (see Figure 5.1).

As shown here, apart from the studies published in Refs. [27, 39, 40], where a direct experimental analysis is made based on either size selected clusters or contrast arising from boron nitride thin films (studies marked with red points in Figure 5.1), the majority of the studies rely on other analyses previously reported in the literature (studies marked with blue points in Figure 5.1).

5.2.1. Methodology

Au and Pd nanoparticles have been deposited via PVD onto amorphous carbon thin films TEM microgrids (Agar Inc.) using an Edwards 306 Turbo evaporation system. During the deposition of Pd and Au, the substrate was maintained at room temperature. A low-magnification image is shown for each case in Figure 5.2 (a) and (b) respectively, for a collection angle of 61.58 mrad.

Throughout the experiment, the microscope conditions have been noted stable. The parameters are: emission current: 129 µA, inner collection angle range: 52.70 to 93.12 mrad. Encircled, in the vicinity of nanoparticles single Au and Pd atoms can be seen.

5.2.2. Results and discussions

A statistical analysis of the variation of the integrated HAADF-STEM intensities, after background subtraction as a function of the inner collection angles (modified by varying the camera length) has been made and is shown for the Au and Pd atoms in Figure 5.3 (a)-(f) and (g)-(l) respectively.

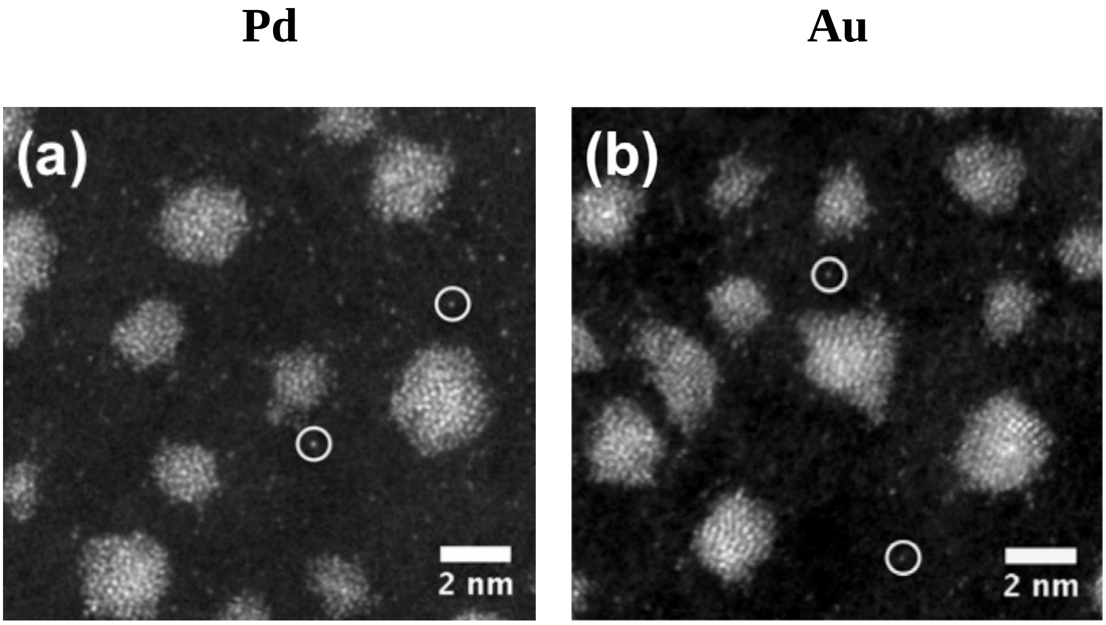

Figure 5.2. Typical HAADF-STEM images of (a) evaporated Pd and (b) evaporated Au nanoparticles on amorphous thin film. In the vicinity of nanoclusters, encircled, single atoms can be observed.

In all cases, we notice that there are discrete peaks with equal spacing, which allows us to associate them as monomers, dimers and trimers respectively.

Examining the data from Figure 5.3, we also notice a decrease in the integrated HAADF-STEM intensities as collection angle is increased for both Au and Pd entities. This is more evident in Figure 5.4 (a)-(c) where a plot of the variation of the integrated HAADF-STEM intensity as a function of the inner collection angle of the detectors for monomers (a), dimers (b) and trimers (c) is shown, for both Au and Pd.

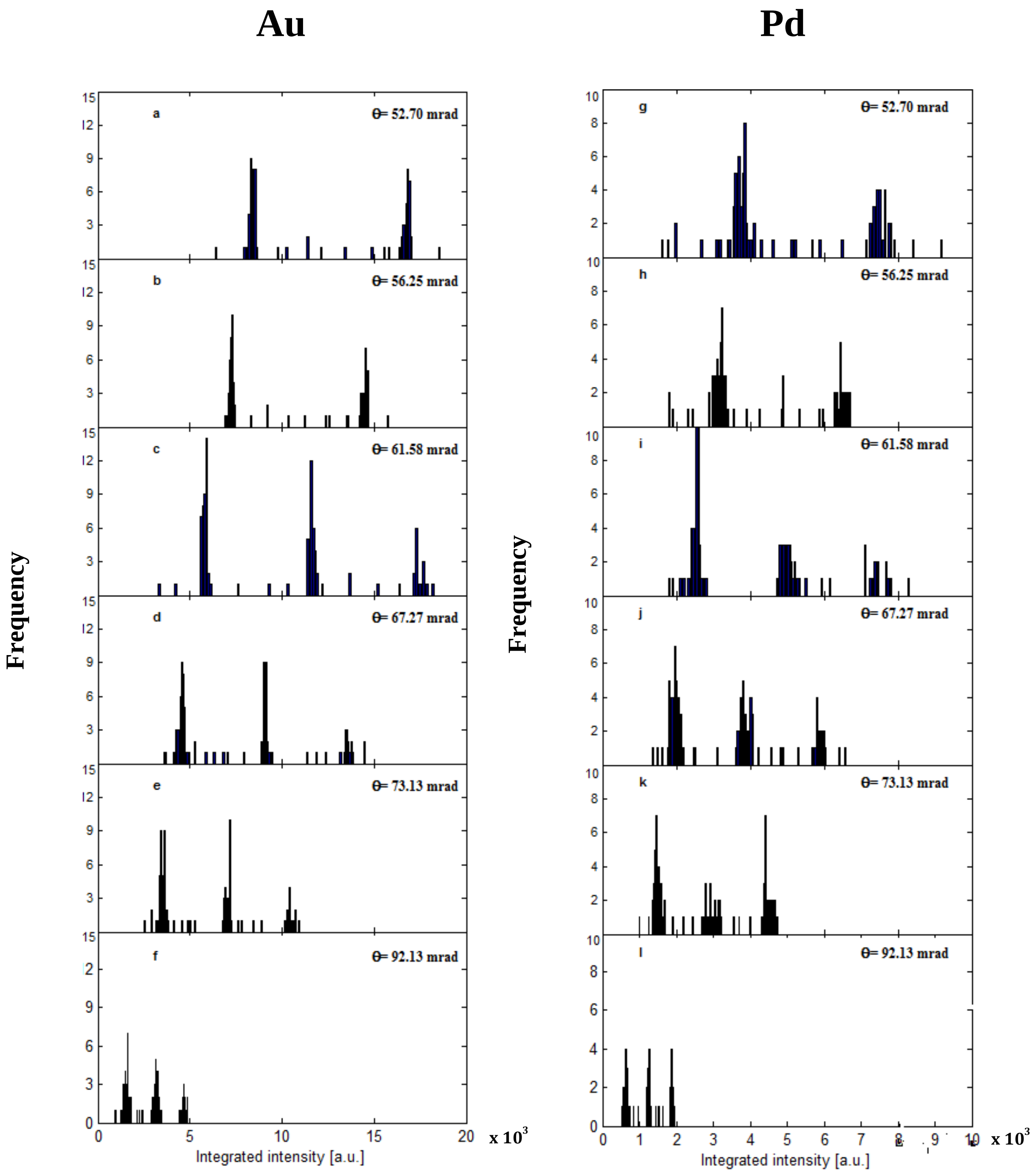

Figure 5.3. HAADF-STEM integrated intensities for Au (a)-(f) and Pd (g)-(l) for various collection angles.

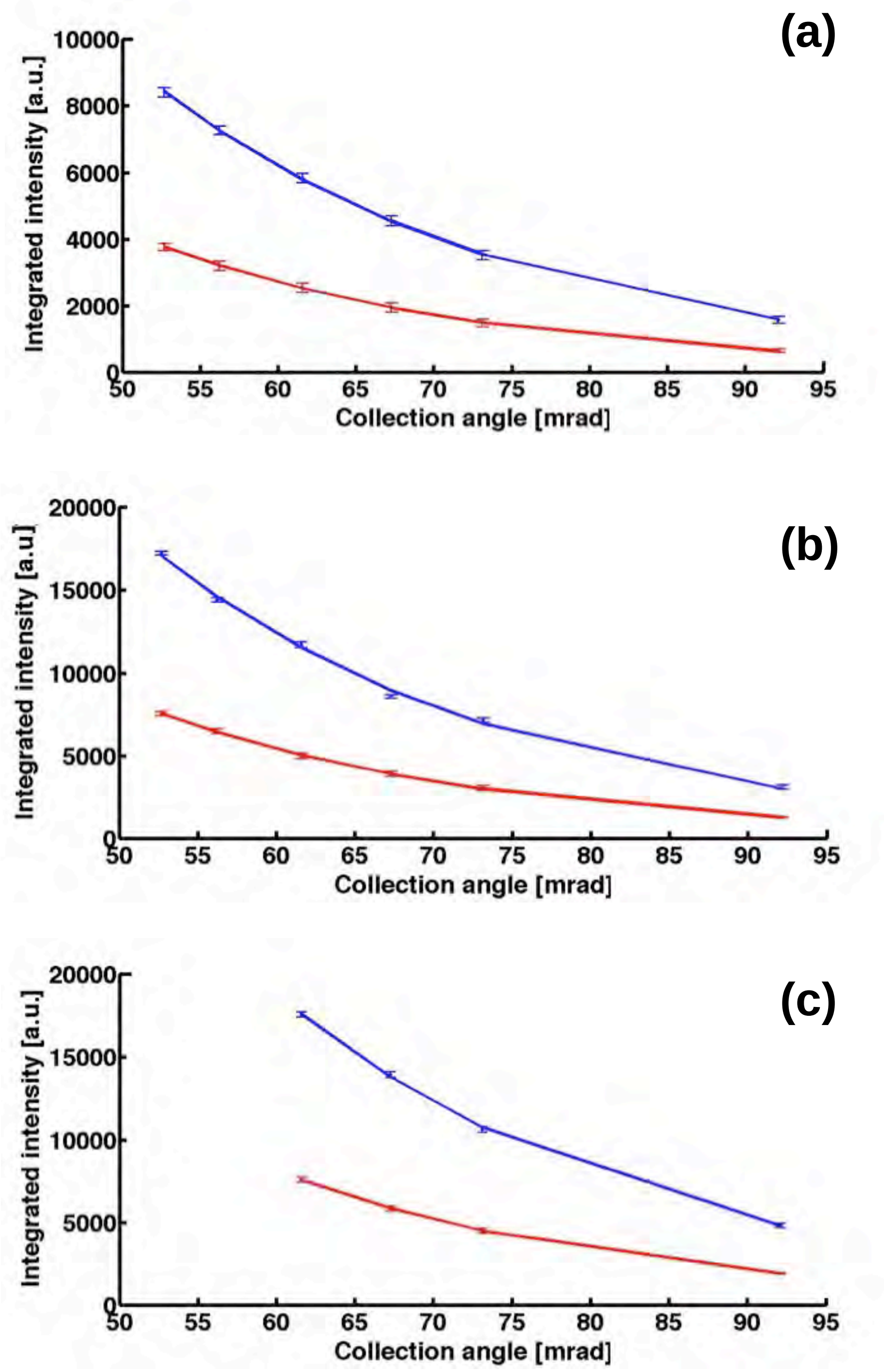

Figure 5.4. HAADF-STEM integrated intensities for monomers (a), dimers (b) and trimers (c) as a function of inner collection angle. Blue lines: Au; Red lines: Pd.

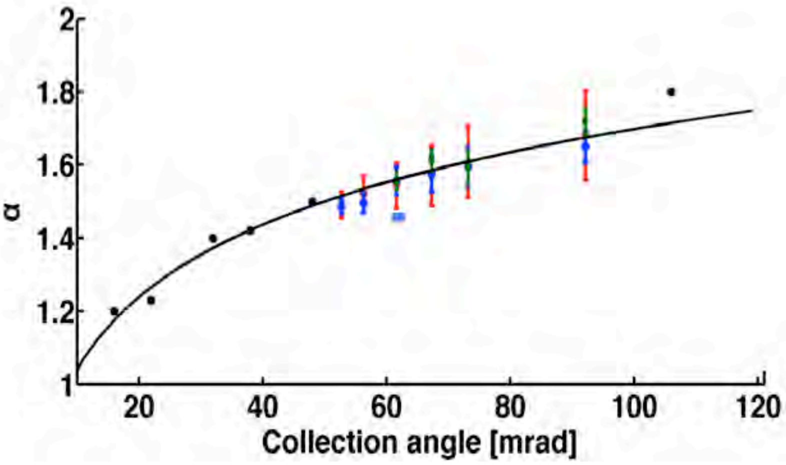

Figure 5.5. Variation of α exponent as a function of inner collection angle (mrad). ● Calculated monomers; ♦ Calculated dimers; ★ Calculated trimers; ● Comparative analysis: experimental data from Ref. [40] for 923-atom size selected Au and Pd clusters; ■ Comparative analysis: 923-atom size selected Au and Pd clusters experimental data from Ref. [39]. Solid line represents best fitting.

There is an obvious intensity contrast between Au and Pd entities, with higher values for Au in comparison with Pd due to the atomic number. As expected, the value of the integrated intensity decreases with increasing inner collection angle, as at large angles the detector collects fewer scattered electrons. This is a well-known effect, whereby at high scattering angles (~100 mrad), the coherent effects of elastic scattering can be neglected, because the scattering is almost entirely thermally diffuse [41, 42]. Assuming the intensity contrast is based on the difference in atomic numbers, where $\frac{I_{Au}}{I_{Pd}} = \left(\frac{Z_{Au}}{Z_{Pd}}\right)^{\alpha}$, then α is derived in this way as a function of collection angle, θ as shown in Figure 5.5.

Here, it is observable that the α exponent is increasing monotonically as a function of collection angles for monomers, dimers and trimers. In Figure 5.5, a comparative analysis of the α exponent in our analysis is made with 923-atom size-selected Au and Pd nanoparticles previously published in Ref. [39] (light blue square). Moreover, in Figure 5.5, a second comparison of the values of the α exponent is made with the data in Ref. [40]. It is however observable that our analysis has been performed on a set of inner collection angles that have not been previously covered in Ref. [40], where α has only been studied for collection angles of 16, 22, 32, 38, 48 and 106 mrad. The solid line in Figure 5.5 shows that the data fit reasonably well with a curve of the type $\alpha = a \cdot \ln\theta + b$, where a and b are the fitting parameters. For our range of angles we have also attempted other fitting equations (see Figures 5.6 for logarithmic fit ($y = a \cdot \ln\theta + b$) and Figure 5.7 for linear fit ($\alpha = a \cdot \theta + b$)), together with the values of the fitting parameters and residual values, for monomers, dimers, trimers and the data from Ref. [40] (see Tables 5.1 and 5.2 respectively).

The linear and logarithmic fits seem to be equally suitable for our data points, judged by the residual value (R^2) up to the second decimal. The values of the fitting coefficients are shown in Tables 5.1 and 5.2 respectively, for each case. The result presented in Figure 5.5 follows well the logarithmic trend calculated in Ref. [43], where it is shown that the value of α depends on the detector's inner and outer collection angle values while the total scattering cross section, characteristic scattering angle, screening radius respectively have been maintained approximately constant [43]. Analogous to the analysis in Ref. [43], the values of α resulted from our analysis is increasing logarithmically towards the value 2, which represents the Coulomb limit. This limit is theoretically attainable when the detector collects only the electrons scattered in the region of the nucleus where its potential is not screened by the electron cloud [43-45]. However, the nucleus is always screened by the electron cloud, resulting in $1.5 \leq \alpha \leq 1.8$ for the studied collection angles. In the analysis regarding the $Au_{24}Pd_1$ clusters, α was taken as having the value 1.52, for an inner collection angle of 61.58 mrad.

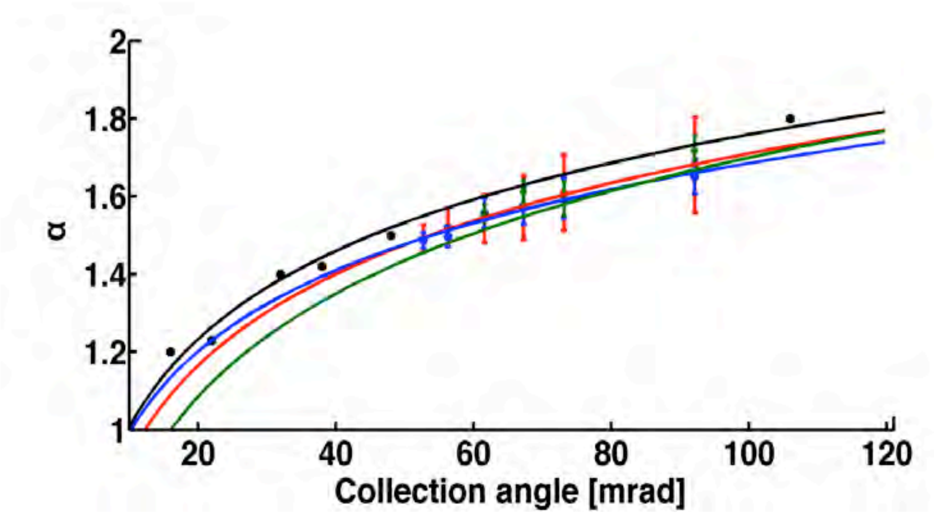

Figure 5.6. Logarithmic fitting ($y = a * \ln(\theta) + b$) for calculated monomers, dimers and trimers. Value of the α exponent vs. inner acceptance angle: ♦ Calculated monomers; ● Calculated dimers; ★ Calculated trimers; ● Comparative analysis with size-selected clusters, adapted from Ref. [40]; (—) Best fitting for monomers – R^2=0.9079; (—) Best fitting for dimers - R^2=0.9017; (—) Best fitting for trimers – R^2=0.9079; (—) Best fitting for adapted data from Ref. [40], R^2=0.9817, where *R* is the fitting residual.

Table 5.1. Values of *a* and *b* coefficients used for fitting equation $y = a * \ln\theta + b$ used in Figure 5.6

Species	**a**	**b**
Monomers	0.3384	0.1514
Dimers	0.2918	0.3372
Trimers	0.3816	-0.0158
Size-selected clusters (Ref. [40])	0.3267	0.9815

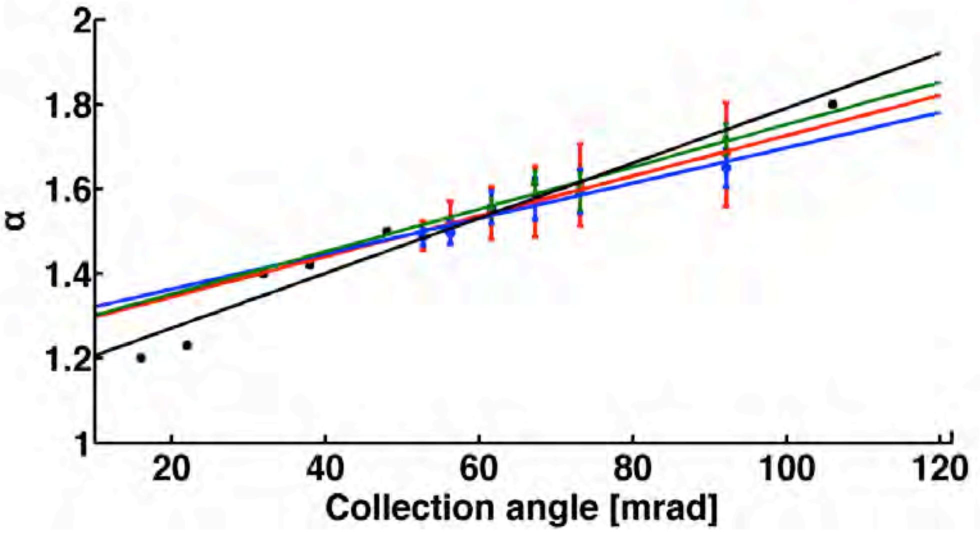

Figure 5.7. Linear fitting ($\alpha = a \cdot \theta + b$) for calculated monomers, dimers and trimers; Comparative analysis with data in [40]. Value of the α exponent as a function of the inner acceptance angle. (♦) Calculated monomers; (●) Calculated dimers; (★) Calculated trimers; (●) Comparative analysis with 923-atom size selected clusters adapted from Ref. [40]; (—) Best fitting monomers – R^2=0.9804; (—) Best fitting dimers - R^2=0.924; (—) Best fitting trimers – R^2=0.9187; (—) Best fitting for data adapted from Ref. [40], R^2=0.9504, where *R* is the fitting residual.

Table 5.2. Values of a and b coefficients used for fitting the equation $y = a * \theta + b$ in Figure 5.7.

Species	**a**	**b**
Monomers	0.00476	1.25
Dimers	0.004172	1.28
Trimers	0.005003	1.252
Size selected clusters (Ref. [40])	0.006495	1.141

5.3. HAADF-STEM characterization of bimetallic $Au_{24}Pd_1$ nanoclusters supported on MWCNTs

The $Au_{24}Pd_1$ nanoparticles have been prepared by Tsukuda's laboratory in Japan using a method described in Ref. [23]. Briefly, the $Au_{24}Pd_1(SR)_{18}$ clusters were used as precursors, whose chemical composition were characterized by mass spectrometry. The thiolate clusters were deposited on MWCNTs and were from the same batch of samples that have been used for catalytic measurements and TEM observations reported in Ref. [23]. The nanoclusters were calcined at a temperature of 450^0C while supported on MWCNTs. The STEM characterization has been made using a JEOL JEM 2100F microscope equipped with a spherical aberration corrected probe (CEOS GmbH).

Figures 5.8 (a) and (b) show two simultaneously acquired high magnification Dark Field (DF) and Bright Field (BF) STEM images of $Au_{24}Pd_1$ clusters supported on MWCNTs. In Figure 5.8 (a), a cluster is visible with strong intensity contrast relative to the carbon nanotubes, as the scattering cross section is dependent on the atomic number, Z (Z_{Au}=79, Z_{Pd}=46, Z_C=6). However, the carbon nanotubes features become more pronounced in the BF image, allowing a measurement of the inter-wall spacing of 3.1 Å, which is in good agreement with previous studies [46]. Other HAADF-STEM images of the $Au_{24}Pd_1$ nanoclusters are shown in Figure 5.9 (a)-(f).

An overview of the sample is shown in Figure 5.10: (a) is a HAADF-STEM image of a selected area typical of this sample and (b) is a histogram of cluster sizes measured by averaging the long and short axis of the 2D projections.

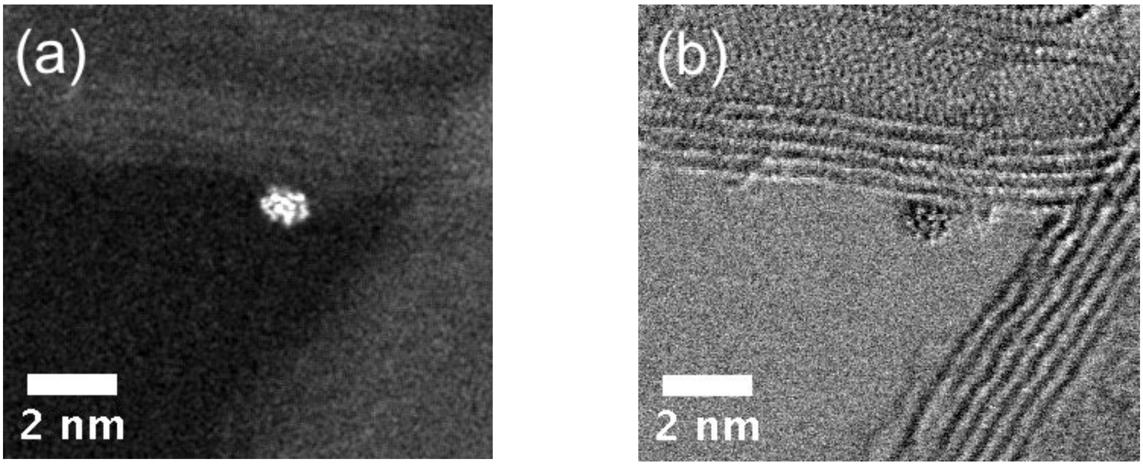

Figure 5.8. (a) Dark Field and (b) bright field images of $Au_{24}Pd_1$ clusters supported on MWCNTs taken simultaneously. The electron dose is 3.32×10^3 electrons/Å^2.

The mean value of the diameter, 1.56±0.25 nm, is slightly larger than the one reported in the paper by Xie et al., 1.2 ±0.2 nm, from TEM analysis [23]. It is well known that Fresnel edge effect in TEM (especially for the un-corrected microscopes) leads to difficulties in cluster size measurement [47]. By taking into account the nearest-neighbour distance of Au (0.288 nm) [48], the 0.36 nm discrepancy observed between the current study using AC-STEM and that of a conventional TEM may be attributed to the underestimation of thickness by about one atomic layer in small clusters by TEM. Nevertheless, both TEM and STEM results agree that a tight size distribution of clusters has been maintained after removal of the thiolate ligands by calcination.

A further confirmation of the cluster size comes from atom counting by utilizing gold atoms as mass standards. Figure 5.11 (a) shows a histogram of the HAADF-STEM intensity integrated over each cluster, in which a well-defined peak at around 1.5x10^5 arbitrary units is apparent. It is known that the HAADF-STEM integrated intensity of a nanoclusters is proportional to the total number of atoms [49, 50].

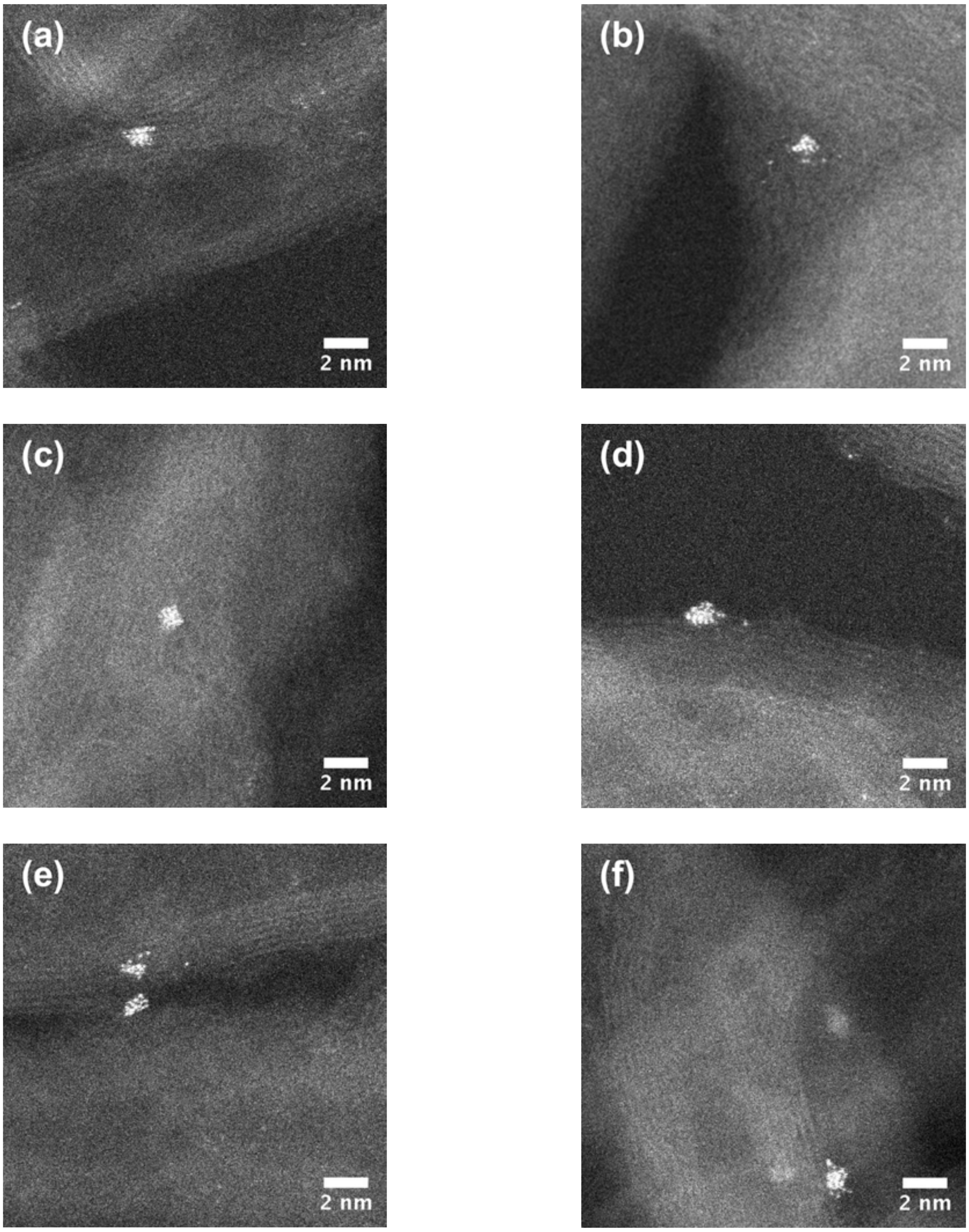
(a)
2 nm
(b)
2 nm
(c)
2 nm
(d)
2 nm
(e)
2 nm
(f)
2 nm

Figure 5.9. (a)-(f) HAADF-STEM images of $Au_{24}Pd_1$ nanoparticles supported on MWCNTs.

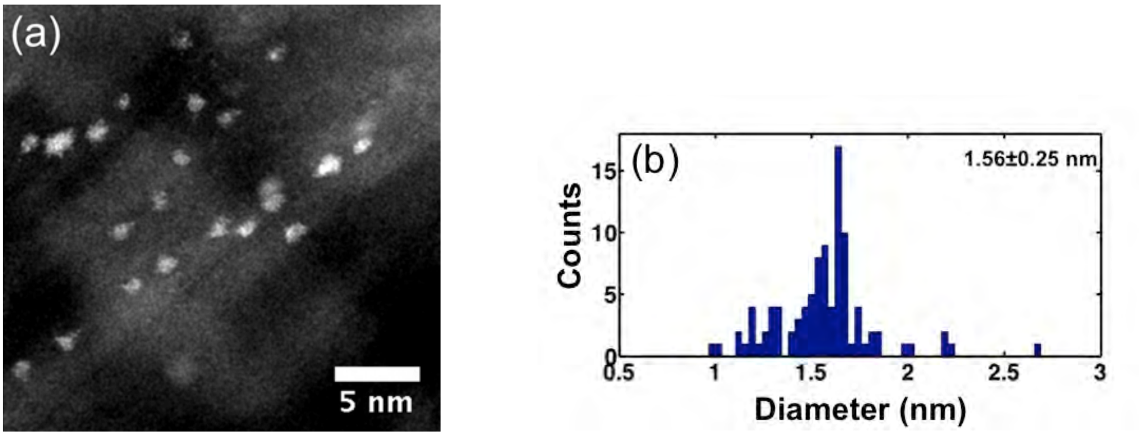

Figure 5.10. (a) HAADF-STEM image showing the $Au_{24}Pd_1$ clusters; (b) Histogram of the cluster size measured by averaging the long and short axes of the 2D projection.

To quantify the cluster size in terms of the number of atoms, we have used single atoms (marked by circles in Figure 5.11 (b) inset) in the immediate vicinity of the $Au_{24}Pd_1$ clusters as a mass standard. To confirm that these are indeed single Au atoms, we have prepared another Au nanoparticle sample via physical vapour deposition (see Figure 5.11 (c)) where some atoms/clusters are visible in the region between Au nanoparticles. A statistical analysis of the integrated intensities for 146 of these isolated entities revealed three discrete peaks with equal separation, with the first peak, located at 5483±71 arbitrary units, a value close to the one obtained in Figure 5.11 (b) using single atoms near $Au_{24}Pd_1$ clusters. We attribute the discrete peaks to the presence of Au monomers, dimers and trimers respectively. By assuming all ligands are removed during the cluster calcination process (due to the small atomic numbers of S, C and H in comparison to Au and Pd, the ligands are invisible in STEM), then, by dividing the integrated intensity of the nanoparticles to the integrated intensity of the Au monomer, we can establish a mean value of $N=25\pm2$ atoms in the $Au_{24}Pd_1$ clusters.

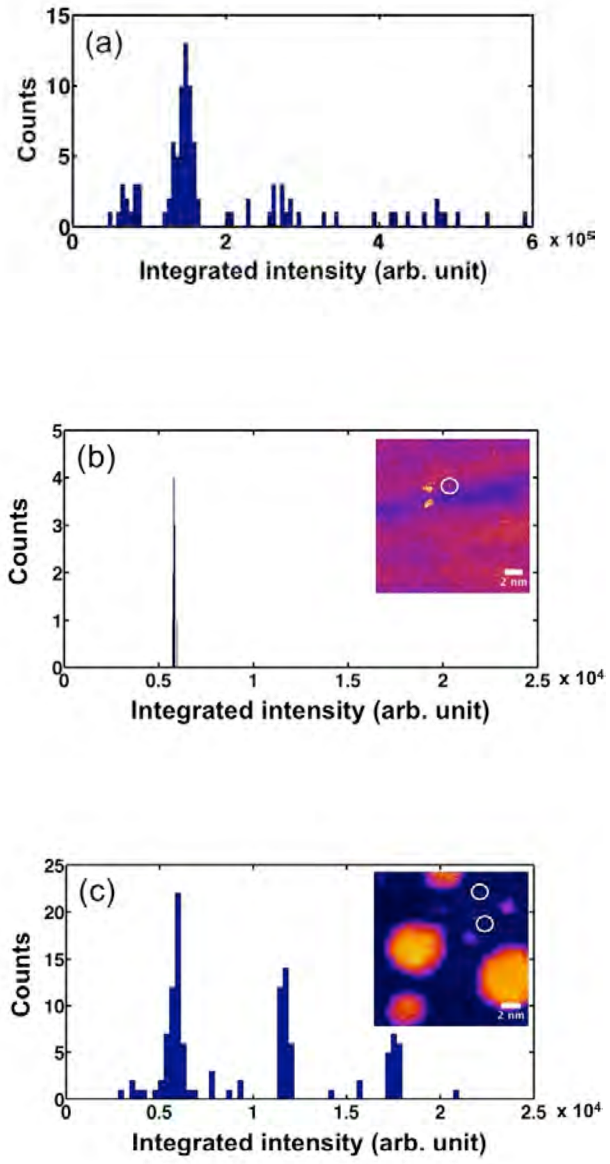

Figure 5.11. (a) Histogram of the HAADF-STEM intensity integrated over each $Au_{24}Pd_1$ cluster after background subtraction; (b) Histogram of the integrated intensity for Au atoms found in the vicinity of $Au_{24}Pd_1$ clusters; an example of the image shown in the inset, where a single atom is encircled; (c) Histogram of the integrated intensity for Au atoms (circled) found in the area between Au nanoparticles on amorphous carbon film prepared via thermal vapour deposition.

A close inspection of the cluster morphologies reveals that not all the clusters are in spherical 2D projection. In Figure 5.12, we plot out the integrated intensity as a function of clusters aspect ratio. It is found that the clusters with the narrow distribution of HAADF integrated intensity around 1.5x10^5 corresponding to size N=25 fall into two groups, with aspect ratio of around 1 and 1.5 respectively (see dotted circles for each group in Figure 5.12).

It should be noted that although, via detailed analysis of the HAADF-STEM images, we have been able to obtain information about the size and shape of the $Au_{24}Pd_1$ clusters and to confirm quantitatively the number of atoms within the clusters, presently *we are not* in a position to identify the location of the single Pd dopant, partly due to the intrinsic instability of small clusters under the 200 kV electron beam. We note that the images used above for the quantitative analysis were recorded at a dose of 3.32×10^3 electrons/Å^2, but they are single passing images. A prolonged e-beam irradiation at this dose did affect the cluster morphology, as in Figure 5.13.

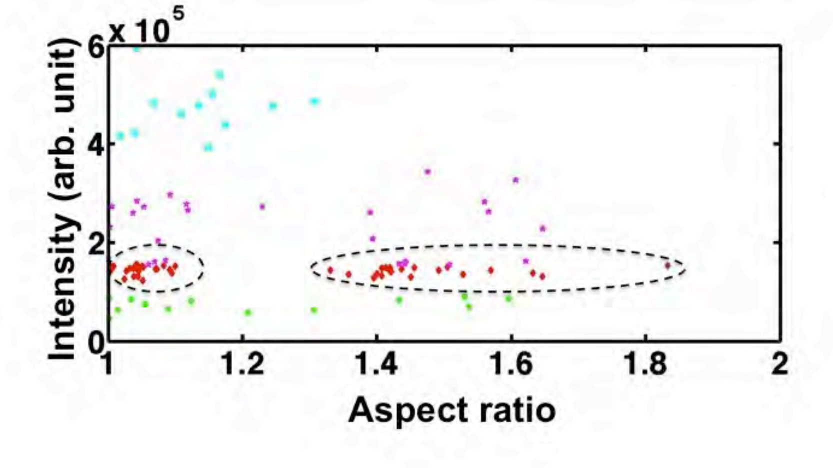

Figure 5.12. A plot of the HAADF-STEM integrated intensity, from Figure 5.11 (a), as a function of the aspect ratio of each cluster measured by the long axis over the short axis.

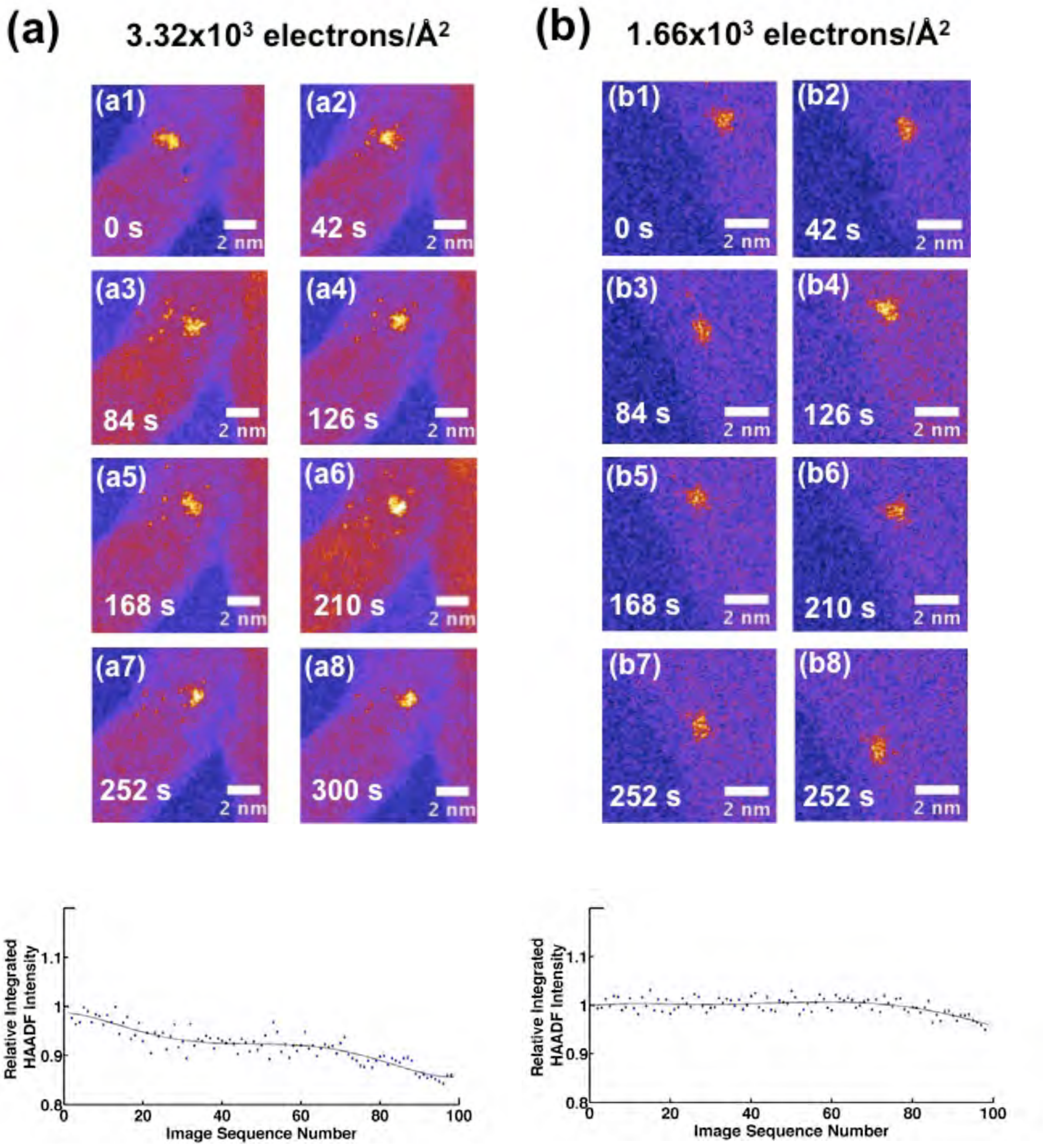

Figure 5.13. (a) Serial acquisition analysis for an electron dose of 3.32×10^3 electrons/Å^2; (b) Serial acquisition analysis for an electron dose of 1.66×10^3 electrons/Å^2. Also shown are the analyses of the variation of the relative HAADF-STEM integrated intensities as a function of image sequence number.

For high electron beam dose, at 3.32×10^3 electrons/Å^2, the cluster has a high degree of fluctuation under the electron beam. Figure 5.13 (a) shows a series of images taken at this dosage. It is observed that the number of atoms present in the immediate vicinity of nanoclusters also increases, due to the momentum transfer between the finely-focused electron beam and the cluster. By plotting the relative HAADF-STEM intensity integrated over the cluster (excluding the single atoms nearby), as a function of image sequence number, it is observed that there is a gradual decrease of the intensity over 100 frames (acquired in 5 minutes). However, when the electron dose was halved, at 1.66×10^3 electrons/Å^2, the cluster fluxionality is suppressed considerably as seen from Figure 5.13 (b). It is also evident that in the latter case the signal to noise ratio is reduced considerably, which make the atomic structure imaging a challenging task. All images presented above are taken using an electron beam current of 129 μA and are first passing images.

5.4. Theoretical analysis of bimetallic $Au_{24}Pd_1$ clusters

In this section, we address the issue of identifying the global minimum (GM) cluster configuration and analysing the potential role of the Pd dopant either as a highly-reactive site or as an indirect reaction promoter. We have first performed a systematic search for the global minimum (GM) configuration of the unsupported cluster at the DFT level using a Basin Hopping/DFT algorithm. Pd to Au charge transfer has then been analysed based on a Löwdin population analysis.

For small clusters, with a number of atoms $N \leq 50$, it is nowdays possible to conduct global optimization searches using energies and forces derived from DFT calculations. For problems of this size, one of the most efficient global optimization methods is the Basin

Hopping algorithm, which couples the Metropolis Monte-Carlo procedure with local minimization [51-53]. The algorithm starts from a random cluster configuration and explores the nanocluster potential energy surface (PES) through moves that randomly modify the geometry of the cluster. When a trial move is made, the new cluster configuration is accepted or rejected with respect to the initial one on the basis of the Metropolis criterion on the energy, after a local minimization is performed, employing a fictitious thermal energy equal to k_BT. In this procedure, the PES of the cluster is modified into a step function, obtained by associating to each point in the configurational space the energy of its near local minimum. BHMC has been coupled with DFT in the so-called BHMC-DFT algorithm, in which the DFT method is used to evaluate the energy and forces (see Ref. [53] for one of its first implementations for gas-phase metal clusters and Ref. [52] for one of its first implementation for supported metal clusters). DFT is particularly suitable for such small cluster systems.

5.4.1. Computational details

Random moves have been chosen as “shake” moves by randomly displacing each atom by ±1.2 Å in the three Cartesian directions. A total of 1000 Monte Carlo optimization steps have been employed, with a thermal energy k_BT=0.02 eV (the low value allows a deeper exploration of certain local structural funnels on the potential energy surface). For the DFT calculations, the Quantum Espresso [54] plane wave self-consistent field code (pwSCF) was chosen, where calculations were performed with PBE [55] exchange-correlation functionals and ultrasoft pseudopotentials. After several test runs, the following parameters were selected for the Basin Hopping procedure: kinetic energy/charge density cut-offs = 12/72 Ry, a cell length of 44 Å using a face centered Bravais cubic cell, gaussian smearing for Brillouin zone = 0.01 Ry (ordinary) and a convergence threshold for self consistency of 10^{-6}. In addition, all calculations were performed using only the Γ-point for the reciprocal space integration. After the most stable structures were identified, 64 lowest energy isomers were re-optimized with kinetic and charge energy cutoffs of 40/320 Ry.

5.4.2. Results and discussions

Using the BHMC-DFT procedure described above, the global minimum isomer of $Au_{24}Pd_1$ has been identified (Figure 5.14 (a)). Other higher-energy isomers are shown in Figure 5.14 (b)-(f). The majority of structures in Figure 5.14 are cage structures, with the interior occupied by a single atom. The addition of one single atom in Figure 5.14 (f) raises the energy by more than 1 eV.

We have noted before that configurations with two core atoms predominate when empirical potentials are used to describe the energetics of the Au-Pd, underlining the need for a more sophisticated, first principles approaches for small clusters. This is shown in Figure 5.15 (a)-(c). For the isomers shown in Figure 5.15, calculations have been made using the Birmingham Cluster Genetic Algorithm (BCGA) [10] coupled with Gupta empirical potentials to model the interatomic interactions. The three sets of parameters, DFT-fit, Exp-fit and Average are described in Ref. [56]. As seen in Figure 5.15, the isomers obtained with the empirical potential tend to have an elongated, poly-icosahedron shape, where Au occupies shell positions and the Pd dopant occupies an off-centered, core position. All the isomers have two inner sites, a motif that has been predicted by the BHMC-DFT as being higher in energy than the putative GM cluster, underlining that the search for global minimum clusters needs more sophisticated, first principle calculations.

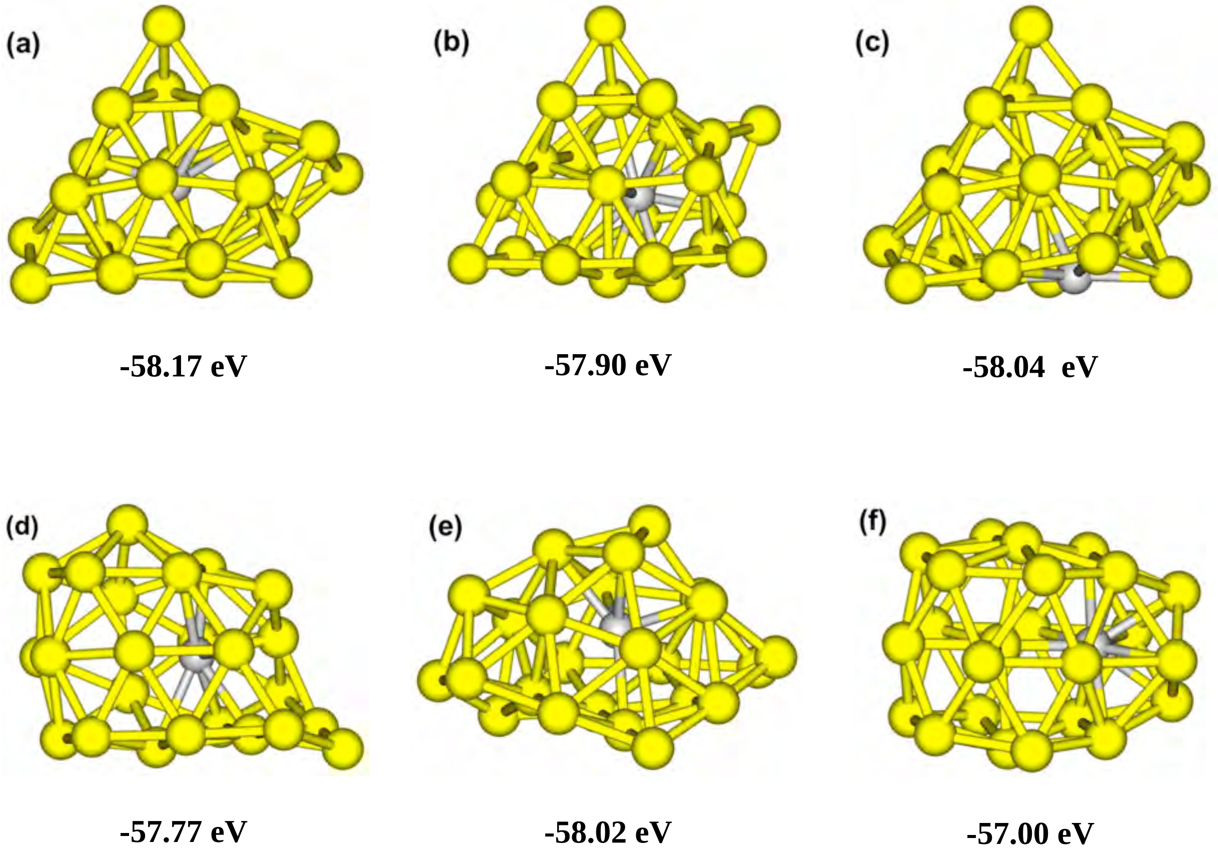

-58.17 eV **-57.90 eV** **-58.04 eV**

-57.77 eV **-58.02 eV** **-57.00 eV**

Figure 5.14. GM cluster obtained using BHMC-DFT approach (a) and other high-energy isomers (b) – (f). The binding energies have also been included.

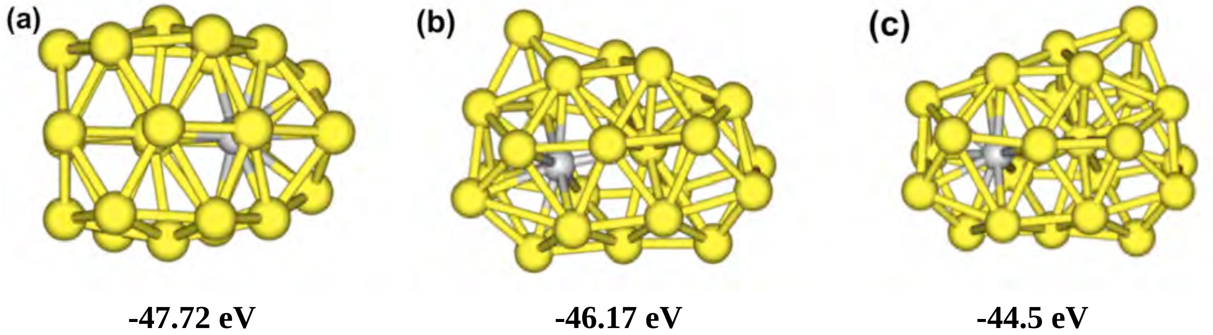

-47.72 eV **-46.17 eV** **-44.5 eV**

Figure 5.15. Isomers obtained with the empirical Gupta potential (a) DFT-fit; (b) Exp-fit; (c) Average parameters. The binding energies have also been included.

The isomers obtained with BHMC-DFT (Figure 5.14) also differ as to whether the Pd dopant atom occupies an interior or surface site: the GM and some lower energy isomers have the Pd dopant located into a core site, but bringing Pd to the surface as in Figure 5.14 (c) only costs 0.2 eV on average. These results are consistent with previous literature suggesting cage structures as the global minima for Au clusters in this size range [57]. Previous work also shows that Au clusters in this size range doped with a single element (Y, Nb, Eu), the dopant occupies a core position [58]. The cage skeleton of the lowest-energy isomer can be characterized as having a tetrahedral pyramid arrangement, which is consistent with the exceptional stability of the pyramid for Au_{20} clusters [53, 59].

However, the cage-skeleton of the high-energy isomers (Figure 5.14 (d)-(e)) exhibits poly-icosahedron geometries that are particularly reminiscent of double-icosahedron motif [60]. These structures bear some similarities to the oblate or elongated polyhedral shapes observed in the experiment (see above) suggesting that the influence of the support on the structure of the clusters may not be important. Finally, it can be noted that all the structures, and especially some of the metastable isomers have low-coordinated Au atoms, which could be important for catalysis.

5.4.3. Charge transfer

The second step of our theoretical studies has been to estimate the charge transfer between Pd and Au. Simple considerations emphasize that the Pauling electronegativity of Pd is 2.2, and of Au is 2.4 [48]. The difference in the electronegativity value leads to an expected charge transfer between the two metal species. The slightly higher electronegativity of Au compared to Pd indicates a certain degree of Pd to Au electron transfer.

The first step has been to generate a pure Au_{25} cluster. This has been achieved by replacing the Pd dopant in the inner site of the cluster by an Au atom, followed by local relaxation at the DFT level. Following the substitution, the Löwdin charge has been calculated. The charge distribution is shown in Figure 5.16 (a) for the Au_{25} cluster. As observed in Figure 5.16 (a), when the inner cluster site is Au, there is an insignificant charge re-distribution (less that 0.11 |e| for the majority of Au atoms on the surface) from the inner Au site to the atoms on the surface, excepting a few atoms on the surface which seem to accept more charge from the central Au atom than the rest (~0.12 |e|), being closer to the inner site.

Löwdin charge analysis has also been made for the case of the GM $Au_{24}Pd_1$ clusters. As shown in Figure 5.16 (b), the charge re-distribution changes. The surrounding Au cage withdraws electron density from the Pd dopant (< 0.1 |e| per atom), excepting a few low-coordinated Au atoms (~ 0.16 |e|). For bimetallic nanoclusters, charge transfer is a consequence of factors such as the cluster geometry and Pauling electronegativity differences between atomic species [61, 62].

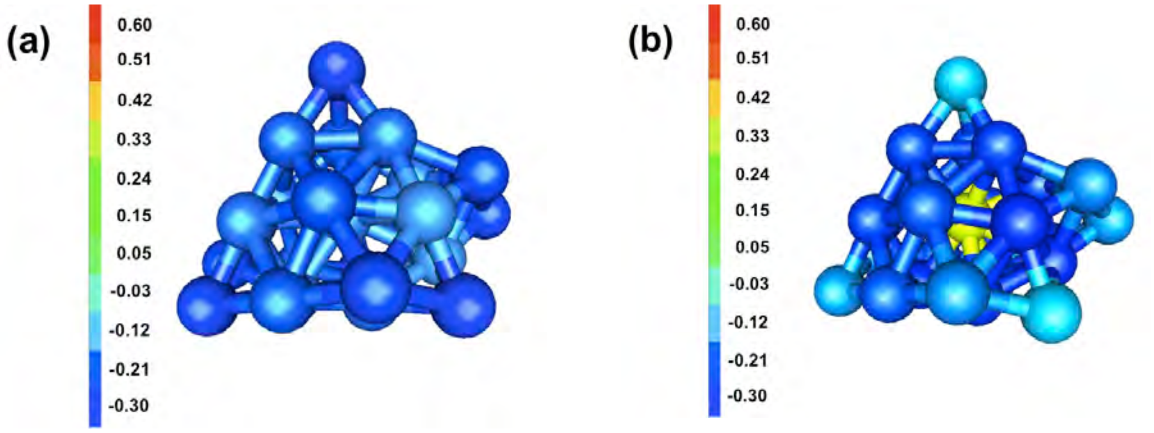

Figure 5.16. Löwdin charge analysis: (a) Au_{25} clusters; (b) $Au_{24}Pd_1$ clusters.

The geometric effect is that there is often a flow of electron density from the cluster core to surface atoms for small clusters [58]. The electronegativity argument is simply that electron density is generally transferred from the less to the more electronegative element, in this case from Pd ($\chi = 2.2$) to Au ($\chi = 2.4$), where χ is the electronegativity.

The combination of geometrical and electronegativity effects can be important in driving the chemical ordering in small bimetallic clusters [58]. Therefore, we conclude that Pd may act as an electron promoter to the surrounding Au atoms, which may explain its role in enhancing the catalytic activity of the gold cluster.

5.5. Conclusions

An analysis of single Pd doped Au_{25} clusters has been performed combining experimental and theoretical techniques. HAADF-STEM has been employed to determine the morphology of clusters supported on MWCNTs, as well as to determine the numbers of atoms in the clusters by using single Au and Pd atoms as mass standards. Based on this analysis, the clusters have been found to possess 25±2 atoms. An analysis of the nanoparticles shape population has proven that two types of projected shapes exist on the sample, namely circular and prolate. The effect of the electron beam on the nanocluster structure and morphology has been determined for high and low electron beam dose. A prominent morphology change and atom loss is observed for high electron beam current, whereas this is less significant for low currents.

At the theoretical level, the low energy structures of free $Au_{24}Pd_1$ clusters are investigated by employing a first principles global optimization method in the form of a Basin Hopping/DFT algorithm, finding a strong tendency of Au cages filled with one single core atom (with the core site being preferentially occupied by Pd). Pyramidal motifs are especially favoured in the cage skeleton, but more complex patterns such as double icosahedra are very close in energy, pointing to a strong fluxional character for this system, and a tendency to oblate shapes, which is consistent with the experiment. A Löwdin population analysis of the total electron density is performed, and a substantial charge transfer from the Pd dopant to the Au cage is observed, suggesting that the Pd dopant acts as an electron promoter to the surrounding Au atoms, which may explain the experimentally observed enhancement of the catalytic activity of Au clusters in this size range upon doping with a single Pd atom.

Bibliography:

---

[1] Brust, M., Walker, M., Bethell, D., Schiffrin, J., Whyman, R., *J. Chem. Soc., Chem. Commun.*, 7, 801, **1994**.

[2] Negishi, Y., Nobusada, K., Tsukuda, T., *J. Am. Chem. Soc.*, 127, 5261, **2005**.

[3] Shichibu, Y., Negishi, Y., Tsunoyama, H., Kanehara, M., Teranishi, T., Tsukuda, T., *Small*, 5, 835, **2007**.

[4] Negishi, Y., Chaki, N. K., Schichibu, Y., Whetten, R., Tsukuda, T., *J. Am. Chem. Soc*., 129, 11322, **2007**.

[5] Link, S., Beeby, A., FitzGerald, S., El-Syaed, M. A., Schaaf, T. G., Whetten, R. L., *Phys. Chem. B*, 106, 3410, **2002**.

[6] Lee, D., Donkers, R. L., Wang, G., Harper, A. S., Murray, R. W., *J. Am. Chem. Soc.*, 126, 6193, **2004**.

[7] Zhu, M., Aikens, C. M., Hendrich, M. P., Gupta, R., Qian, H., Schatz, G. C., Jin, R., *J. Am. Chem. Soc*., 131, 2490, **2009**.

[8] Guo, J. J., Yang, J. X., Die, D., *Commun. Theor. Phys*., 48, 348, **2007**.

[9] Ma, W., Chen, F., *Catal. Lett.*, 143, 84, **2013**.

[10] Johnston, R. L. (ed.), *Nanoalloys: From Theory to Applications*, RSC Publishing, Cambridge, **2008**.

[11] Ferrando, R., Jellinek, J., Johnston, R. L., *Chem. Rev*., 108, 845, **2008**.

[12] Scott, R. W. J., Sivadinarayana, C., Wilson, O. M., Yan, Z., Goodman, D. W., Crooks, R. M., *J. Am. Chem. Soc*., 127, 1380, **2005**.

[13] Enache, D. I., Edwards, J. K., Landon, B., Solsona-Espriu, B., Carley, A. F., Herzing, A. A., Watanabe, W., Kiely, C. J., Knight, D. W., Hutchins, G. J., *Science*, 311, 362, **2006**.

---

[14] Schmid, G., *Chem. Rev.*, 92, 1709, **1992**.

[15] Remita, H., Etchberry, A., Belloni, J., *J. Phys. Chem. B.*, 107, 31, **2003**.

[16] Herzing, A. A., Kiely, C. J., Carley, A. F., Landon, P., Hutchins, G. J., *Science*, 321, 1331, **2008**.

[17] Heaven, M. W., Dass, A., White, P. S., Holt, K. M., Muray, R. W., *J. Am. Chem. Soc*. 130, 3754, **2008**.

[18] Fields-Zinna, C. A., Crowe, M. C., Dass, A., Weaver, J. E. F., Murray, R. W., *Langmuir*, 25, 7704, **2009**.

[19] Kacprzak, K. A., Lehtovaara, L., Akola, J., Lopez-Acevedo, O., Hakkinen, H., *Phys. Chem. Chem. Phys.*, 11, 7123, **2009**.

[20] Jiang, D. E., Dai, S., *Inorg. Chem*., 48, 2720, **2009**.

[21] Walter, M., Moseler, M., *J. Phys. Chem. C.*, 113, 15834, **2009**.

[22] Jellinek, J. (ed.), *Theory of atomic and molecular clusters*, Springer, Berlin, **1999**.

[23] Xie, S., Tsunoyama, H., Kurashige, W., Negishi, Y., Tsukuda, T., *ACS Catal.*, 2, 1519, **2012**.

[24] Yuan, D. W., Gong, X. G., Wu, R., *Phys. Rev. B.*, 75, 085428, **2007**.

[25] Pittaway, F., Paz-Borbon, L. O., Johnston, R. L., Arslan, H., Ferrando, R., Mottet, C., Barcaro, G., Fortunelli, A., *J. Phys. Chem. C.*, 113, 9141, **2009**.

[26] Ferrer, D., Blom, D. A., Allard, L. F., Mejia-Rosales, S., Perez-Tijerina, S., Jose-Yacaman, M. J., *J. Mater. Chem*., 18, 2442, **2008**.

[27] Krivanek, O. L., Chisholm, M F., Nicolosi, V., Pennycook, T. J., Corbin, G. J., Dellby, N., Murfitt, M., Own, C. S., Szilagyi, Z. S., Oxley, M. P., Pantelides, S. T., Pennycook, S. J., *Nature*, 464, 571, **2010**.

[28] Hilliard, S., Silcox, J., *Ultramicroscopy*, 58, 6, **2005**.

[29] Treacy, M. M., Gibson, J. M., *J. Microsc*., 180, 2, **1995**.

[30] Pennycook, S. J., Rafferty, B., Nellist, P. D., *Microsc. And Microanal*., 6, 343, **2000**.

[31] Dwyer, C., Etherige, J., *Ultramicroscopy*, 96, 343, **2003**.

[32] Ernie, R. (ed.), *Aberration Corrected Imaging in Transmission Electron Microscopy*, Imperial College Press, London, **2010**.

[33] Voyles, P. M., Grazul, J. L., Muller, D. A., *Ultramicrscopy*, 96, 251, **2003**.

[34] Takeguchi, M., McMcartney, M. R., Smith, D. J., *Appl. Phys. Lett.*, 84, 2103, **2004**.

[35] Lakner, H., Mendorf, C., Bollig, B., Prost, W., Tegude, F. J., *Mater. Sci. and Eng*., B44, 52, **1997**.

[36] Di Vece, M., Bals, S., Verbeeck, J., Lievens, P., Van Tendeloo, G., *Phys. Rev. B*, 80, 125420, **2009**.

[37] Allen, J. A., Hemesath, E., Perea, D. E., Lensch-Flak, J. L., Li, Z. Y., Yin, F., Gass, M. H., Wang, P., Bleloch, A. L., Palmer, R. E., Lauhon, L. J., *Nature Nanotechnol*., 3, 168, **2008**.

[38] Liu, C. P., Twesten, R. G., Gibson, J. M., *Ultramicroscopy*, 87, 79, **2011**.

[39] Wang, Z. W., Palmer, R. E., *J. Phys. Conf. Ser*., 371, 1, **2012**.

[40] Wang, Z. W., Li, Z. Y., Park, S. J., Abdela, A., Tang, D., Palmer, R. E., *Physical Review B*, 84, 073408, **2011**.

[41] Nellist, P. D., Pennycook, S. J. (eds.), *Scanning Transmission Electron Microscopy: Imaging and Analysis*, Springer, Berlin, **2011**.

[42] Howie, A., *J. Microsc*., 117, 11, **1979**.

[43] Hartel, P., Rose, H., Dinges, C., *Ultramicroscopy*, 63, 93, **1996**.

[44] Jesson, D. E., Pennycook, S. J., *Proc. Roy. Soc.*, A449, 273, **1993**.

[45] Walther, T., *J. Microsc*., 221, 137, **2006**.

---

[46] Xie, X., Gan, T., Sun, D., Wu, K. in *Fullerenes, Nanotubes and Carbon Nanostructures*, Taylor&Francis, New Jersey, **2008**.

[47] Watt, I. M., *The principles and practice of electron microscopy*, 2nd edition, Cambridge Univ. Press, Cambridge, **1997**.

[48] Kittel, C., *Introduction to solid state physics*, 6th edition, John Wiley&Sons, New York, **1986**.

[49] Young, N., Li, Z. Y., Chen. Y., Palomba, S., Palmer, R. E., Bleloch, A. L., Curley, B. C., Johnston, R. L., Jiang, J., Yuan, J., *Nature*, 451, 46, **2008**.

[50] Li, Z. Y., Young, N. P., Di Vece, M., Palomba, S., Palmer, R. E., Bleloch, A. L., Curley, B. C., Johnston, R. L., Jiang, J., Yuan, J., *Nature*, 451, 46, **2008**.

[51] Wales, D., Scheraga, H. A., *Science*, 285, 1368, **1999**.

[52] Barcaro, G., Apra, E., Fortunelli, A., *Chem. Eur. J.*, 13, 6408, **2007**.

[53] Apra, E., Ferrando, R., Fortunelli, A., *Phys. Rev. B.*, 73, 205414, **2006**.

[54] Giannozzi, P., Baroni, S., Bonini, N., Calandra, M., Car, R., Cavazzoni, C., Ceresoli, D., Chiarotti, G. L., Cococcioni, M., Dabo, I., Corso, A. D., De Gironcoli, D., Fabris, S., Fratesi, G., Gebauer, R., Gerstmann, U., Gougoussis, C., Kokalj, A., Lazzeri, M. L., Marzari, N., Mauri, F., Mazzarello, R., Paolini, S., Pasquarello, A., Paulatto, L., Sbraccia, C., Scandolo, S., Sclauzero, G., Seitsonen, A. P., Smogunov, A., Umari, P., Wentzcovich, R. M., *J. Phys.: Condens. Matter.*, 21, 395502, **2009**.

[55] Perdew, J. P., Burke, K., Ernzerhof, M., *Phys. Rev. Lett.*, 77, 3865, **1996**.

[56] Ismail, R., Johnston, R. L., *Phys. Chem. Chem. Phys.*, 12, 8607, **2010**.

[57] Johannson, M. P., Sundholm, Vaara, J., *Angew. Chem. Int. Ed.*, 43, 2678, **2004**.

---

[58] Veldeman, N., Janssens, E., Hansen, K., DeHaek, J., Silverans, R. E., Lievens, P., *Faraday Discuss*., 138, 147, **2008**.

[59] Li, J., Li, X., Zhai, H. J., Wang, L. S., *Science*, 299, 864, **2003**.

[60] Farges, D. H., De Feraudy, M. F., Raoult, B., Torchet, G., *Surf. Sci*, 156, 370, **1985**.

[61] Jellinek, J. (ed), *Theory of atomic and molecular clusters*, Springer, Berlin, **1999**.

[62] Chen, F., Johnston, R. L., *Acta Materialia*, 56, 2374, **2008**.

Chapter VI

Structures of bimetallic AuPd nanoparticles prepared by physical vapour deposition

6.1. Overview

Bimetallic AuPd nanoparticles have received special attention in recent years, especially due to their important applications such as in nanocatalysis [1], fuel cells [2] or optics [3]. Various morphologies have been obtained for AuPd nanoparticles depending on the deposition methods employed, ranging from mixed structures [4] to $Pd_{core}Au_{shell}$ [5], $Pd_{shell}Au_{core}$ [6] or even three-layer AuPd nanoparticles [7]. Simple thermodynamic considerations, based on concepts such as surface energy (E_{surf}), cohesive energy (E_{coh}), atomic radius (r_a) and electronegativity (χ) can offer important insights into the preferred segregation sites in AuPd nanoalloys. Table 6.1 lists these parameters for Au and Pd.

Table 6.1. Parameters influencing segregation in bimetallic AuPd nanoparticles. From Ref. [8].

Element	**E_{coh} (eV/atom)**	**E_{surf} (meVÅ^{-2})**	**r_a (Å)**	χ
Pd	3.89	131	1.38	2.2
Au	3.81	96.8	1.44	2.4

Based on the values listed in Table 6.1, it is observable that thermodynamic considerations favour segregation of Au to the surface in AuPd nanoparticles. This is because of: (i) larger cohesive energy of Pd (influences the maximization of Pd-Pd bonds) (ii) smaller surface energy of Au (iii) smaller atomic radius of Pd (atoms with smaller radius help minimize the bulk elastic strain) (iv) higher electronegativity of Au in comparison with Pd (as shown in Ref. [8], the element with lower electronegativity tends to donate electrons).

Figure 6.1 shows the bulk AuPd phase diagram where three long ordered phases are present: $L1_2$ (Au_3Pd), $L1_0$ (AuPd) and $L1_2$ ($AuPd_3$) [9, 10]. In literature, ordered crystallographic phases have been identified upon annealing at 773 K [11] in thin AuPd films with <001> orientation. They are: $L1_2$ phase around composition Au_3Pd, $L1_2$ phase around composition $AuPd_3$ and $L1_0$ phase around composition AuPd [12-14].

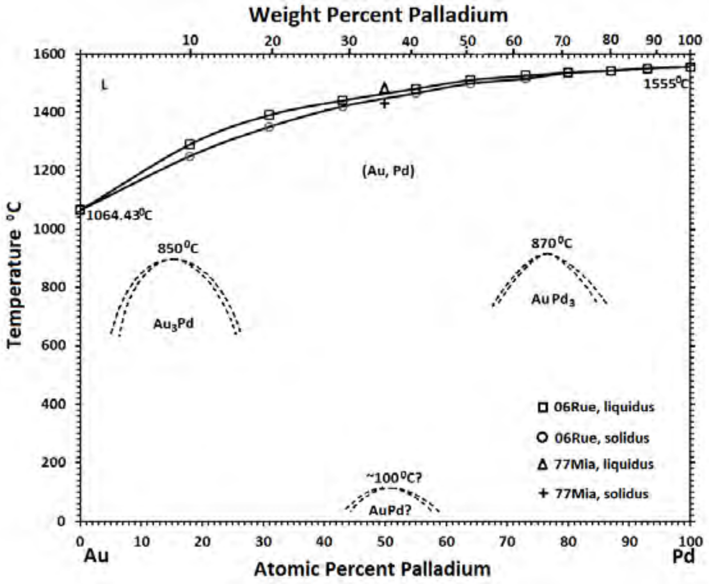

Figure 6.1. The AuPd phase diagram. Adapted from Ref. [9].

Theoretically, both molecular dynamics (MD) based simulations and Density Functional Theory (DFT) calculations have predicted the existence of equilibrium configurations in nanoparticles in which Pd occupies core positions and Au occupies surface positions [15-17]. It has been shown previously that, at low temperature, configurations like $Au_{core}Pd_{shell}$ are possible, but once the temperature is increased, Au tends to migrate towards the nanoparticle's surface [15-17]. Other theoretical predictions of cluster structure and segregation (chemical ordering) based on the use of empirical potentials (EPs) and DFT calculations have also been employed for the study of AuPd nanoparticles [18, 19]. At empirical level it has been found that, for small size bimetallic AuPd clusters (34 or 38-atom clusters [18]), various segregation patterns such as core-shell, ball and cup, spherical cap, mixed (ordered, random) can be obtained by finely tuning the parameters of the empirical potentials. We have shown in Chapter V that, by performing direct searches at the DFT level using Basin Hopping Monte Carlo (BHMC) algorithms, the equilibrium structure of the 25-atom AuPd system is where the Pd dopant is located in the nanoclusters core. For larger sizes (98-atom AuPd nanoclusters), calculations performed at both empirical and DFT levels (see Chapter IV and Ref. [20]) predict again that $Pd_{core}Au_{shell}$ configurations are the most stable cluster structures in comparison with other mixed configurations.

Although the $Pd_{core}Au_{shell}$ structure tends to be a stable configuration at 0 K for free/unsupported clusters, this trend may be strongly influenced by factors such as substrate, temperature, pressure, gas molecular adsorption during or post-production. Kinetic effects may also dramatically influence the morphology of nanoclusters. Theoretically, MD simulations have shown that core-shell inversion can take place for AuPd nanoclusters at a temperature of 500 K [21].

In this chapter we demonstrate the application of physical vapour deposition (PVD) for the production of bimetallic nanoparticles. This relatively easy-to-implement method offers feasibility and a high degree of control over the morphology of bimetallic nanoparticles post deposition, using thermal treatment methods. The goal of this study is to investigate the processes that take place in evaporated AuPd nanoparticles upon annealing. Here, we show that, for a fixed annealing temperature and variable annealing time, the nanoparticles change their morphology and chemical ordering. The analysis has involved the use of HAADF-STEM and electron diffraction methods. In order to demonstrate the presence of Au and Pd, the Energy Dispersive X-ray (EDX) Spectroscopy was employed for the elemental mapping of bimetallic AuPd nanoparticles deposited by PVD.

6.2. Preparation of bimetallic AuPd nanoparticles via physical vapour deposition

The evaporated AuPd nanoparticles have been deposited using an Edwards 306 Turbo Evaporation system (Figure 6.2), operating at a base pressure of 10^{-7}mbar. The nanoparticles have been deposited onto carbon film coated TEM commercial copper grids (Agar Inc.). The deposition time for Au and Pd has been for 3 seconds each. In order to avoid the formation of intermetallic compounds between Pd and the boat during the deposition procedure, we have used a ceramic-coated tungsten boat (Kurt Lesker Inc.). During the deposition of nanoparticles, an increase in the pressure up to ~10^{-5} mbar has been recorded. The following procedure is adopted to obtain AuPd bimetallic nanoparticles: Pd nanoparticles are first deposited onto an amorphous carbon substrate and we then let the pressure in the chamber re-stabilize to its initial value.

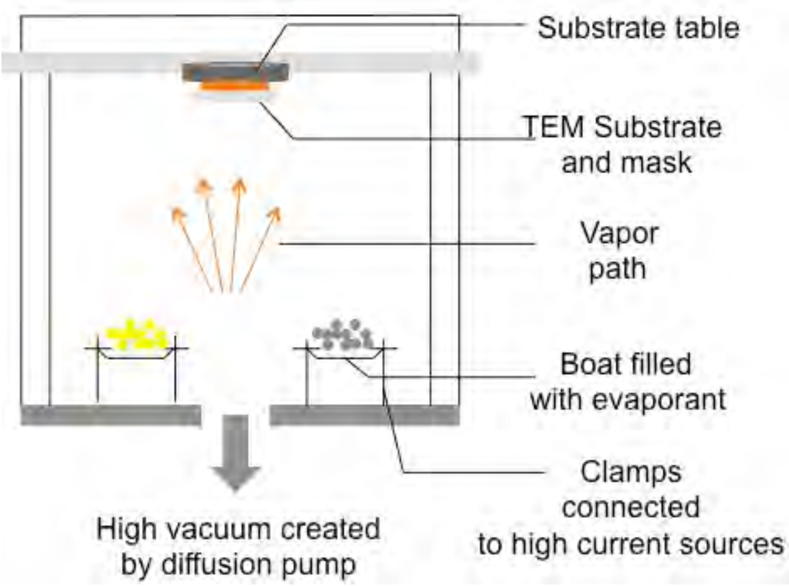
Substrate table
TEM Substrate and mask
Vapor path
Boat filled with evaporant
Clamps connected to high current sources
High vacuum created by diffusion pump

Figure 6.2. Schematic representation of the Edwards 306 Turbo evaporation system used for the production of AuPd nanoparticles.

Following this, Au is deposited, after which we let the pressure to re-stabilize again. The as-deposited samples are annealed, post deposition, for periods of 60 minutes, 120 minutes and 180 minutes at a temperature of 500 K, *in situ*. After the annealing, each sample is then let to cool down to room temperature and stored in a low vacuum desiccator in order to avoid oxidation. The choice of annealing temperature, 500 K, has been made following the study published in Ref. [15], where it has been shown that a core-shell inversion can take place for AuPd nanoclusters at this temperature.

6.3. As-deposited AuPd sample

Figures 6.3 (a) shows a low-magnification HAADF-STEM image of the as-deposited AuPd sample. As seen here, the nanoparticles appear to be deposited uniformly over the substrate. We have performed a statistical analysis of the diameter distribution, as shown in Figure 6.3 (b), and the mean value of the diameters is 1.70±0.34 nm, as evident from the histogram of the size distribution. A high magnification HAADF-STEM image of an as-deposited nanoparticle is shown in Figure 6.3 (c), together with its fft pattern in Figure 6.3 (d). The nanoparticle is in the <110> orientation and we can observe only the presence of the main spots in the fft pattern. We have calculated the mean value of the lattice spacing (noted herein with *a*), to be 0.24±0.03 nm. To analyse the lattice spacing values further, we have calibrated it against pure Au and Pd nanoparticles.

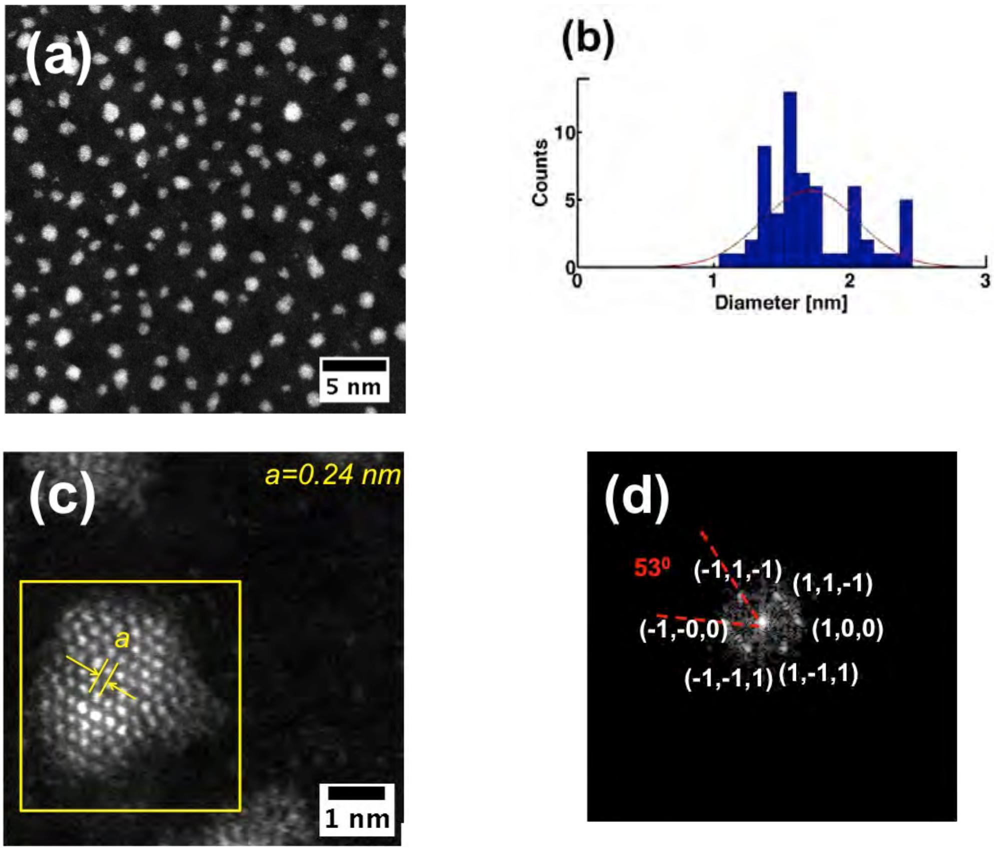

Figure 6.3. (a) Low magnification HAADF-STEM images of as-deposited nanoparticles; (b) Statistical size distribution – mean value of diameters: 1.70±0.34 nm; (c) High magnification HAADF-STEM image of an as-deposited nanoparticle; (d) FFT pattern of the nanoparticle marked with yellow frame in (c).

Figure 6.4 (a) and (c) show two representative high magnification HAADF-STEM images of evaporated Au and Pd nanoparticles supported on amorphous carbon substrate in <110> orientation. The experimental lattice spacing values has been determined by performing a line profile on the selected atomic column (see yellow lines in Figure 6.4 (a) and (c)). Our analysis has shown that the experimentally determined lattice spacing value for Au nanoparticles is 0.28±0.03 nm (Figure 6.4 (b)).

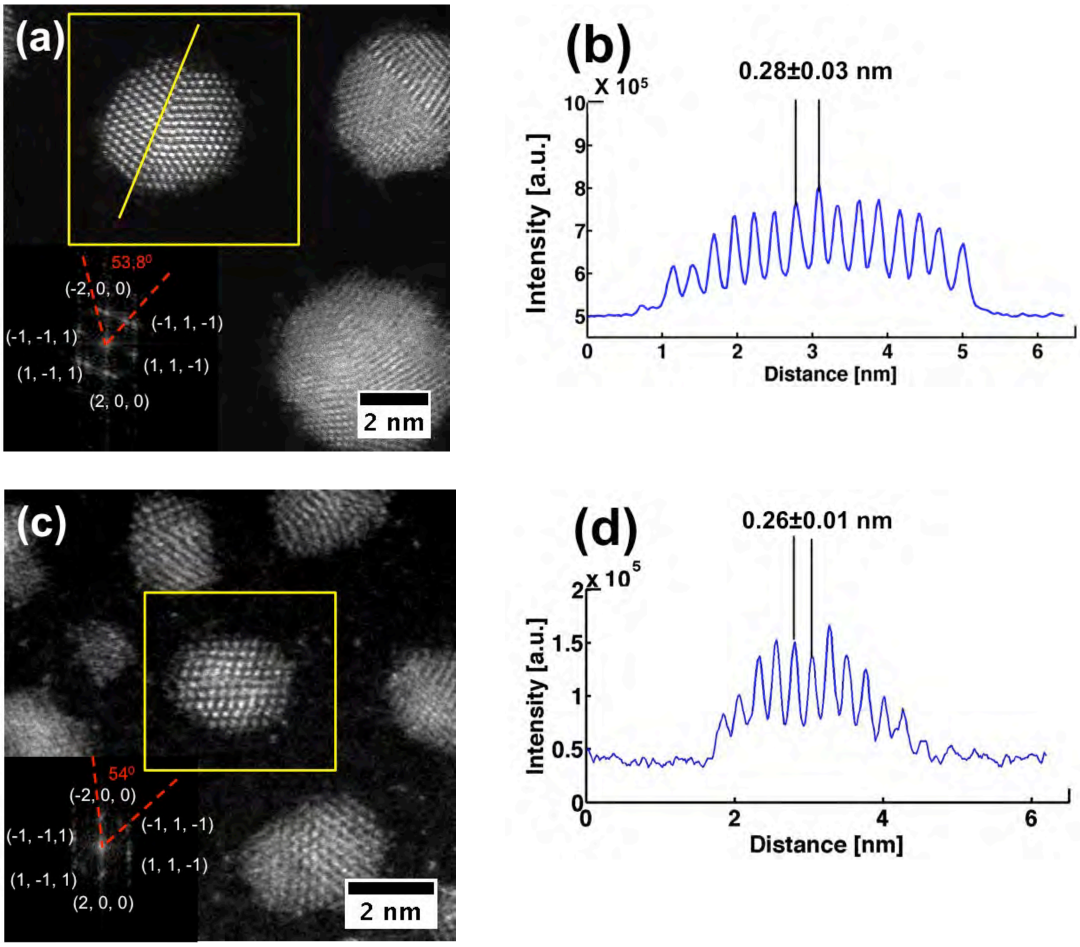

Figure 6.4. (a) HAADF-STEM image of evaporated Au nanoparticles deposited on amorphous carbon substrate; (b) Lattice spacing analysis performed on the line profile in (a); (c) HAADF-STEM image of evaporated Pd nanoparticles deposited on amorphous carbon substrate; (d) Lattice spacing analysis performed on the line profile in (c). Insets are showing the fft patterns of the nanoparticles in marked with yellow frame.

Table 6.2. Theoretical values of lattice spacing of Au and Pd in <110> and <100> orientation. From Ref. [22].

Metal	**<110>**	**<100>**
Au	0.28 nm	0.20 nm
Pd	0.27 nm	0.19 nm

The experimentally determined value for the case of evaporated Pd nanoparticles is 0.26±0.01 nm (Figure 6.4 (d)). These values are close to the theoretical values of Au and Pd bulk lattice spacing in <110> orientation (see Table 6.2). These calibration values will be further used as a reference for the lattice spacing measurement of AuPd nanoparticles.

6.4. AuPd samples upon annealing

6.4.1. Formation of ordered $L1_2$ crystallographic phases

For the evaporated AuPd nanoparticles deposited onto amorphous carbon substrate, the purpose has been to determine the effect of annealing temperature and time over nanoparticles morphology. Therefore, following the deposition process, the microgrid has been annealed *in situ*, at a temperature of 500 K for 60 minutes, 120 minutes and 180 minutes respectively.

Figure 6.5 (a) and (c) shows two typical images of AuPd nanoparticles annealed for 60 minutes and 120 minutes respectively at 500 K. Here we observe a variation of contrast across the nanoparticle.

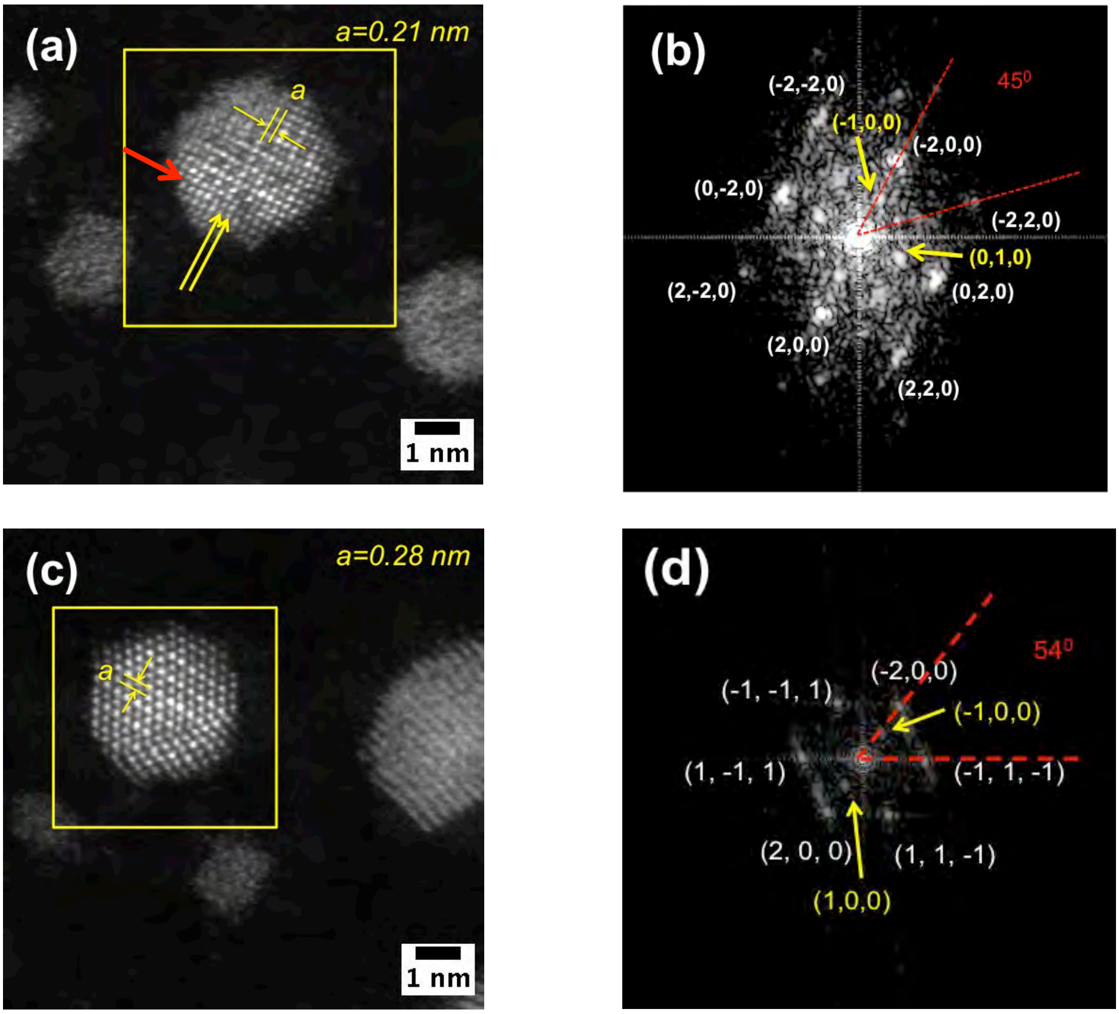
(a)
a=0.21 nm
a
1 nm
(b)
(-2,-2,0)
(-1,0,0)
(-2,0,0)
45^0
(0,-2,0)
(-2,2,0)
(0,1,0)
(2,-2,0)
(0,2,0)
(2,0,0)
(2,2,0)
(c)
a=0.28 nm
a
1 nm
(d)
54^0
(-2,0,0)
(-1, -1, 1)
(-1,0,0)
(1, -1, 1)
(-1, 1, -1)
(2, 0, 0)
(1, 1, -1)
(1,0,0)

Figure 6.5. HAADF-STEM images of two evaporated mixed AuPd nanoparticles annealed for (a) 60 and (c) 120 minutes at 500 K; (b) FFT pattern of the nanoparticle marked with square frame in (a), revealing main and secondary spots, indication of superlattice formation; (d) FFT pattern of the nanoparticle marked with square frame in (c).

The contrast in the HAADF-STEM images is influenced by the changes in composition governed by the difference in atomic numbers of the constituent elements ($Z_{Au}=79$, $Z_{Pd}=46$) [19]. The HAADF-STEM intensity is proportional to the atomic number Z by the law $I \sim Z^{1.52}$ for a collection angle of 61.58 mrad, as calibrated in Chapter V. An AuPd nanoparticle annealed for 60 minutes at 500 K is shown in Figure 6.5 (a), together with its fft pattern (Figure 6.5 (b)). The nanoparticle is in the <100> orientation towards the electron beam. It appears to have a well-ordered mixed pattern, where pure Au columns alternate with Au+Pd columns in two-dimensional projection, as marked by the yellow arrow pointers.

The measurement of the lattice spacing of the nanoparticle in Figure 6.5 (a) revealed a value of 0.21±0.02 nm, a value averaged over several atomic columns. This value is more close to the theoretical bulk <100> lattice spacing of Au (see Table 6.2). Examining Figure 6.5 (a) in more detail, it is observed that the ordering of the alternating Au and Au+Pd columns in two dimensional projection is not maintained over the entire nanoparticle, indicated by the fact that towards the edge of the nanoparticle, Au-rich regions can also be identified, as marked by the red arrow pointer.

Mixed AuPd nanoparticles have also been identified after 120 minutes of annealing at 500 K, as shown in the HAADF-STEM image in Figure 6.5 (c), where a nanoparticle in <110> orientation towards the electron beam is observed. A measurement of the lattice spacing has indicated a value of 0.28±0.01 nm, a value more close to the theoretical lattice spacing of Au in <110> orientation (see Table 6.2).

The corresponding fft patterns for the mixed evaporated AuPd nanoparticles in <100> and <110> orientation are shown in Figure 6.5 (b) and (d) respectively. A closer inspection of the diffraction patterns reveals the existence of primary and secondary spots in both cases. The presence of secondary spots in the patterns is an indication of an ordered crystallographic phase between Au and Pd [9]. This is explained by the AuPd phase diagram (see Figure 6.1 and Ref. [15]) in the introduction section, where there are three reported ordered phases: $L1_2$ (Au_3Pd), $L1_0$ (AuPd) and $L1_1$ ($AuPd_3$). The stacking sequence associated with the $L1_2$ crystallographic phase is shown in Figure 6.6. (a) for a crystal in <100> orientation and for the general case of an fcc unit lattice in Figure 6.6 (b).

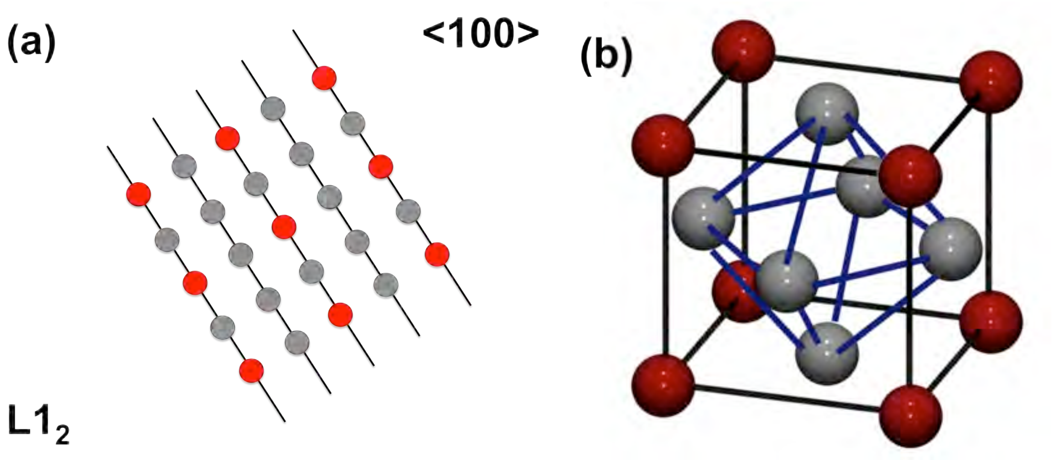

Figure 6.6. Schematic representation of the (a) $L1_2$ and ordered crystallographic phases in <100> orientation. Red circles: Palladium atoms; Grey circles: Au atoms; (b) General representation of the $L1_2$ ordered phase. Taken from Ref. [9]).

By comparing the stacking sequences in Figures 6.5 (a), (c) with Figures 6.6 (a) and (b) and by associating the corresponding fft patterns, we propose that the AuPd nanoparticles annealed for 60 and 120 minutes at 500 K form an $L1_2$ ordered phase. According to Ref. [9], the ordered $L1_2$ crystallographic phase is a derivative of the fcc lattice.

As mentioned in Ref. [9], an $L1_2$ structure is an ordered A_3B alloy (in our case Au_3Pd), involving the ordering of A on the face centres of the fcc lattice and B on the cube vertices on a crystal unit. However, it should be mentioned that the presence of $L1_2$ ordered phases can only be identified for the cases of nanoparticles annealed at 500 K, not as deposited.

For the AuPd system, in the literature, long range crystallographic phases have been reported for the case of chemically-synthesized AuPd nanoparticles [23]. In Ref. [23], High-Resolution Transmission Electron Microscope (HRTEM) has been employed for the study of the bimetallic AuPd system, and ordering has been explained on the basis of the diffusion phenomenon of Au and Pd atoms, forming an ideal stacking sequence of Au and Pd atomic columns. Other literature reports indicate the existence of Au-Pd alloy phases upon heat treatment at 773 K [11, 24, 25]. Other long range ordered structures have been identified for the case of bimetallic AuPd thin films, in <100> orientation. They are $L1_2$ type around the composition Au_3Pd, $L1_1$ type around the composition $AuPd_3$ and $L1_0$ type around the composition AuPd, as reported in Refs. [12-14].

6.4.2. Segregation effects

Annealing the sample at a temperature of 500 K for 120 and further, at 180 minutes, has also led to other nanoparticle morphologies, namely layered and core-shell.

Two representative HAADF-STEM images of these types of clusters are shown in Figure 6.7 (a), a layered nanoparticle, and Figure 6.7 (c), a core-shell nanoparticle annealed for 120 minutes at 500 K. The nanoparticle shown in Figure 6.7 (a) is in <110> orientation towards the electron beam, with a mean lattice spacing value of 0.29±0.01 nm, averaged over several atomic columns. This value is more close to the theoretical value of nearest neighbour distance for Au in <110> orientation, as shown in Table 6.2. The fft pattern of the layered AuPd nanoparticle is shown in Figure 6.7 (b) but, as observed here, the double diffraction spots are missing. This could be an indication that the superlattice is *not* formed for this case, upon annealing at 500 K. However, this is not the case for the core-shell nanoparticle shown in Figure 6.7 (c), and its corresponding fft pattern in Figure 6.7 (d), where double reflection spots are visible, an indication that the superlattice formation has taken place. The core-shell nanoparticle in Figure 6.7 (c) is in <100> orientation towards the electron beam, with a mean lattice spacing of 0.20±0.03 nm, averaged over several atomic columns.

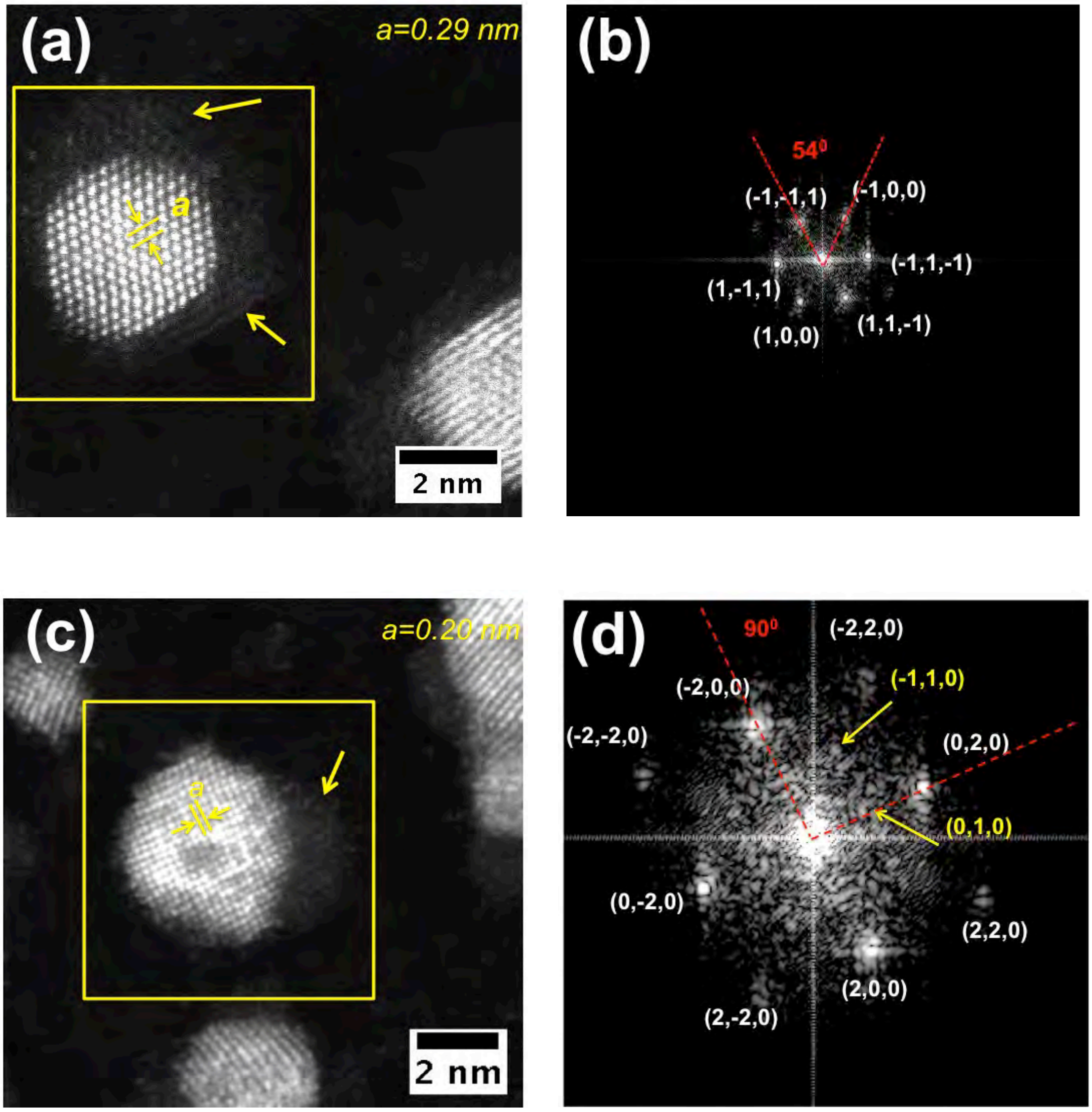
(a)
a=0.29 nm
a
2 nm
(b)
54⁰
(-1,-1,1)
(-1,0,0)
(-1,1,-1)
(1,-1,1)
(1,0,0)
(1,1,-1)
(c)
a=0.20 nm
a
2 nm
(d)
90⁰
(-2,2,0)
(-2,0,0)
(-1,1,0)
(-2,-2,0)
(0,2,0)
(0,1,0)
(0,-2,0)
(2,2,0)
(2,0,0)
(2,-2,0)

Figure 6.7. (a) HAADF-STEM image of a layered evaporated AuPd nanoparticle annealed at 500 K for 120 minutes; (b) FFT pattern of the nanoparticle marked with yellow square in (a); (c) HAADF-STEM image of a core-shell AuPd nanoparticle annealed at 500 K for 120 minutes; (d) FFT pattern of the nanoparticle marked with yellow square in (c). Yellow arrow pointers indicate the presence of PdO incompletely surrounding the nanoparticle.

This value is again more close to the value of the theoretical value of the nearest-neighbour distance for Au in <100> orientation (see Table 6.2).

Moreover, examining Figures 6.7 (a) and (c), it is observable that a fine layer surrounds the nanoparticles, forming a clear interface with the Au-rich regions of the nanoparticles, as marked by the yellow arrow pointers. When annealing at 500 K for 120 and 180 minutes, the diffused layer did not surround the nanoparticles completely, without exception. We associate this layer to PdO.

The reason behind this conclusion will be discussed below as well as in section 6.4.3, where thermodynamic considerations and Energy Dispersive X-ray Spectroscopy elemental mapping will be discussed in order to understand oxidation effects.

Similar nanoparticles morphologies (i.e. layered and core-shell) have also been observed when annealing for 180 minutes at 500 K, as shown in Figure 6.8 (a) and (c).

Figure 6.8 (a) shows a layered AuPd nanoparticle in <110> orientation towards the electron beam. The lattice spacing value, averaged over several atomic columns, is 0.29±0.02 nm. The value is again closer to the bulk nearest neighbour distance for Au (see Table 6.2) and also resembles what was seen in the case of layered AuPd nanoparticles annealed at 500 K for 120 minutes.

The nanoparticle has an external diffused PdO layer, incompletely surrounding the nanoparticle on the upper and lower part. The lattice spacing of the PdO layer will be discussed in detail below, in section 6.4.3. The fft pattern is shown for this case in Figure 6.8 (b), where the superlattice formation is indicated by the presence of double diffraction spots. The morphology of the core-shell AuPd nanoparticle annealed for 180 minutes at 500 K is shown in Figure 6.8 (c). The nanoparticle consists in a diffused external PdO layer, an intermediate Au-rich shell and an off-centred Pd-rich core.

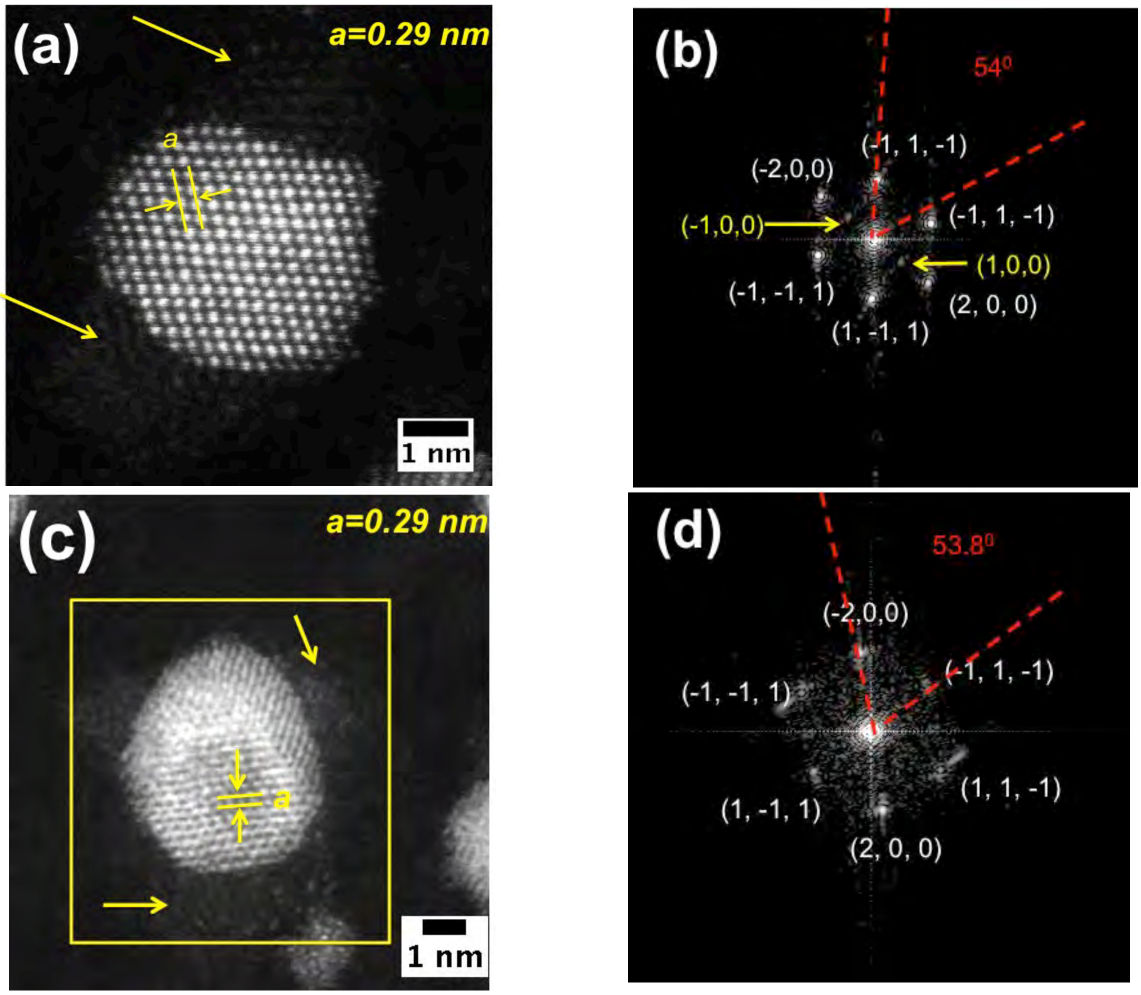
(a)
a=0.29 nm
a
1 nm
(b)
54°
(-1, 1, -1)
(-2,0,0)
(-1,0,0)
(-1, 1, -1)
(1,0,0)
(-1, -1, 1)
(2, 0, 0)
(1, -1, 1)
(c)
a=0.29 nm
a
1 nm
(d)
53.8°
(-2,0,0)
(-1, -1, 1)
(-1, 1, -1)
(1, 1, -1)
(1, -1, 1)
(2, 0, 0)

Figure 6.8. (a) HAADF-STEM image of a layered evaporated AuPd nanoparticle annealed at 500 K for 180 minutes; (b) FFT pattern of the nanoparticle in (a); (c) HAADF-STEM image of a core-shell AuPd nanoparticle annealed at 500 K for 180 minutes; (d) FFT pattern of the nanoparticle marked with yellow square in (c). Yellow arrow pointers indicate the presence of PdO surrounding incompletely the nanoparticle.

However, if we examine the fft pattern in Figure 6.8 (d), it is observable that, unlike the layered nanoparticle annealed for 180 minutes at 500 K, the pattern does not show the presence of double diffraction spots. This is again an indication that, upon annealing the superlattice did not form. This may be due to insufficient temperature driven re-arrangement of Au and Pd to form an $L1_2$ superlattice [23].

It should however be noted that mixed morphologies have not been encountered for the case of nanoparticles annealed at 500 K for 180 minutes. Therefore, for the case of 180 minutes of annealing at 500 K, the predominant morphologies of nanoparticles are layered and core-shell. The disappearance of the mixed nanoparticles could be explained by the possibility that they may be trapped into a thermodynamically metastable state. Further annealing at 500 K for 180 minutes has resulted in the formation of layered or core-shell morphologies [26].

As observed in the case presented above, the HAADF-STEM analysis of the AuPd nanoparticles, regardless of the annealing temperature and time, has revealed the presence of a contrast, which has been interpreted as a consequence of the difference in atomic numbers of Au and Pd. EDX has been employed for the confirmation of elemental distribution of the sample and is useful method for elemental mapping of bimetallic nanoparticles [27, 28].

The elemental mapping of AuPd nanoparticles are shown in Figure 6.9 and 6.10, for the cases of mixed and core-shell types of nanoparticles respectively, both obtained following the annealing procedure at 500 K for 120 minutes. Each map was acquired for a period of 30 minutes. The distribution maps are acquired by detecting the Au Lα and Pd Lα X-rays, whereas the distribution map of O is acquired by detecting the Kα X-rays. For each case, the electron diffraction pattern is also included. For the selected Region of Interest (ROI), the EDX mapping has shown that, the Pd, Au and O are present.

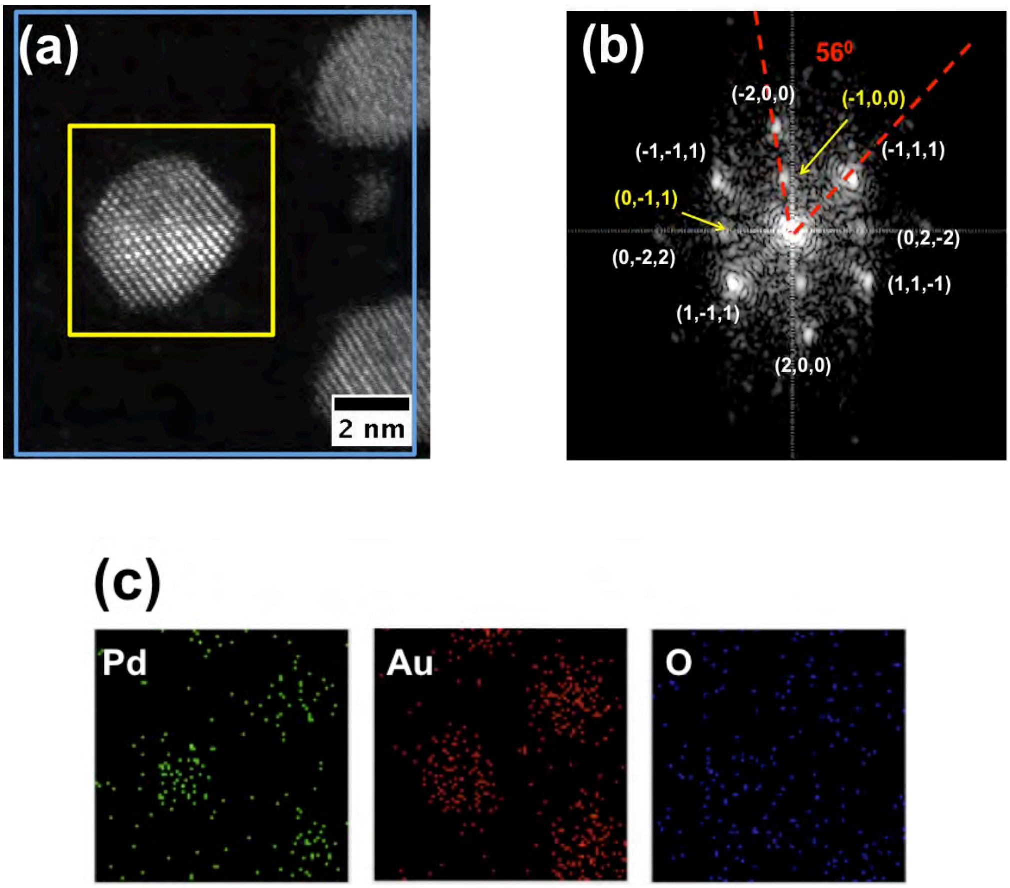

Figure 6.9. (a) HAADF-STEM image of a mixed AuPd nanoparticle annealed for 120 minutes at 500 K; Yellow frame represents the ROI for which the fft pattern was considered; Blue frame represents the ROI where the EDX mapping was performed; (b) FFT pattern for the nanoparticle in (a); (c) Mapping of Pd, Au and O respectively.

The signal indicating the presence of Au, Pd and O is predominantly localized to the region where the nanoparticles are located in Figures 6.9 and 6.10. The presence of the O signal is an indication that the nanoparticles are affected by the oxidation process, due to the presence of Pd and its high affinity towards oxidation.

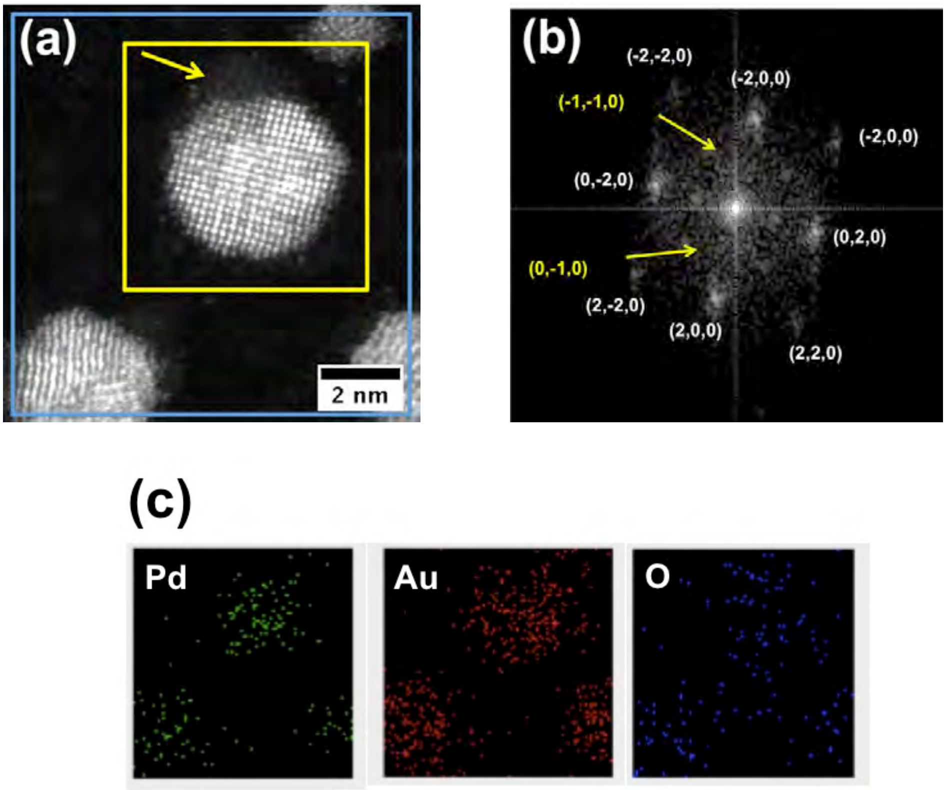

Figure 6.10. (a) HAADF-STEM image for core-shell AuPd nanoparticle annealed for 120 minutes at 500 K; Yellow frame represents the ROI for which the fft pattern was taken; Blue frame represents the ROI where the EDX mapping was performed; the yellow arrow pointer indicates the presence of a diffused PdO layer on the corner of the nanoparticle; (b) FFT pattern for the nanoparticle in (a); (c) Mapping of Au, Pd and O, respectively.

We should however mention that, due to the relative small dimensions of the studied AuPd nanoparticles, the use of the EDX for the determination of nanoparticles composition is not suitable, this method of analysis not being an atomically-resolved one. Nevertheless, the information obtained using EDX are complementing the analysis performed sing HAADF-STEM, confirming the presence of both metals in our evaporated AuPd nanoparticles.

6.4.3. Oxidation effects

For the nanoparticles annealed at 500 K for long periods of time like 120 and 180 minutes, we have observed experimentally that a thin layer surrounded the nanoparticles incompletely and we have attributed it to the presence of PdO in section 6.4.2. A low magnification HAADF-STEM image of AuPd nanoparticles inter-connected by the PdO layer is shown in Figure 6.11. A closer inspection of the lattice spacing of Pd revealed a value of 0.30±0.01 nm, averaged over several atomic columns. This value is larger than the theoretical value of the nearest neighbour distance of Pd in <110> orientation (see Table 6.2). Possible causes for the dilation of the Pd lattice is the incorporation of either oxygen [29] or carbon [30] into the lattice.

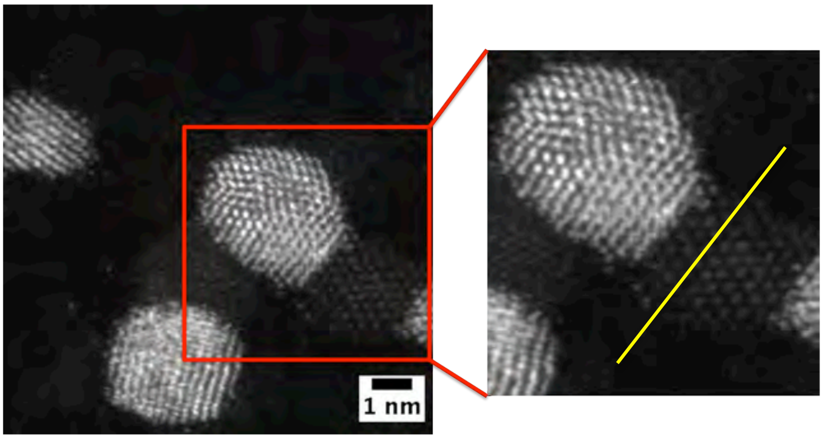

Figure 6.11. Left: HAADF-STEM image of PdO layer interconnecting three nanoparticles. Right: a magnified image of the region marked by the red square, revealing the well-ordered structure of the PdO layer diffused on the carbon substrate following the annealing of AuPd NP for 120 minutes, *in situ*, at 500 K. Yellow line indicates the line profile used in Figure 6.12 (c) for the estimation of PdO layer thickness.

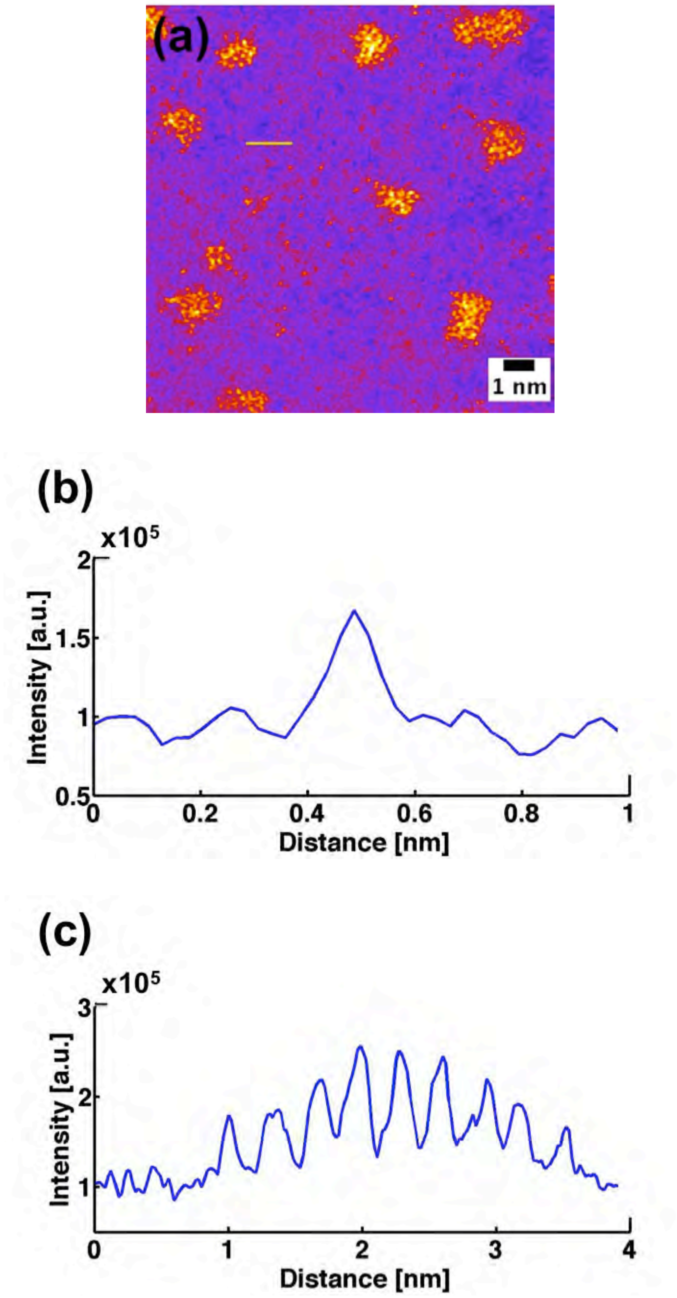

Figure 6.12. (a) HAADF-STEM image of pure evaporated Pd nanoparticles deposited on amorphous carbon. Encircled, in the vicinity of nanoparticles, single atoms can be observed, which have been used for the calibration of the PdO layer thickness. (b) Line profile of a Pd atom marked with yellow line in (a); (c) Line profile of the PdO layer marked with a yellow line in Figure 6.11.

Moreover, we have attempted to perform an estimation of the PdO layer thickness, based on the intensity of a Pd atom, as follows. Evaporated Pd nanoparticles are deposited onto the surface of amorphous carbon substrate.

A low magnification HAADF-STEM image of evaporated Pd is shown in Figure 6.12 (a) where, encircled, in the vicinity of Pd nanoparticles, are single atoms. We have performed a comparative analysis of the intensity of one Pd atom (see yellow line in Figure 6.12 (a) and the plotted line profile in Figure 6.12 (b)) with the intensity of the PdO layer (see yellow line profile in Figure 6.11 and plotted line profile in Figure 6.12 (c)). By comparing the intensity of the line profile for the single Pd atom with the intensity of the line profile of the Pd layer, we have been able to estimate the thickness for *this particular case* to be ~ 2 layers. The thickness of the PdO layer is almost in all cases ≥ 2 layers, since Pd could not in principle form well-ordered layers under this thickness.

The presence of oxygen is confirmed by the EDX elemental mapping in section 6.4.2. Based on thermodynamic considerations, the oxidation of Pd can be understood in terms of Gibbs free energy accompanying the formation of an oxide. The free energies for the formation of PdO is $\left(\Delta_f G\right)^{Pd}$ = - 95.9 kcal/O atom [31] at a temperature of 500 K, whereas that for AuO at the same temperature is positive, $\left(\Delta_f G\right)^{Au}$ = + 10.5 kcal/O atom [32]. Therefore, metallic auric oxide is stable when exposed to oxygen [32], and the metallic Pd oxide formation is thermodynamically favourable.

We have prepared, for comparison, two different samples of evaporated Au and Pd nanoparticles on the surface of amorphous carbon substrate. Post deposition, the samples have been annealed *in situ* for 120 minutes at 500 K. The representative images are shown in Figure 6.13 (a) and (b).

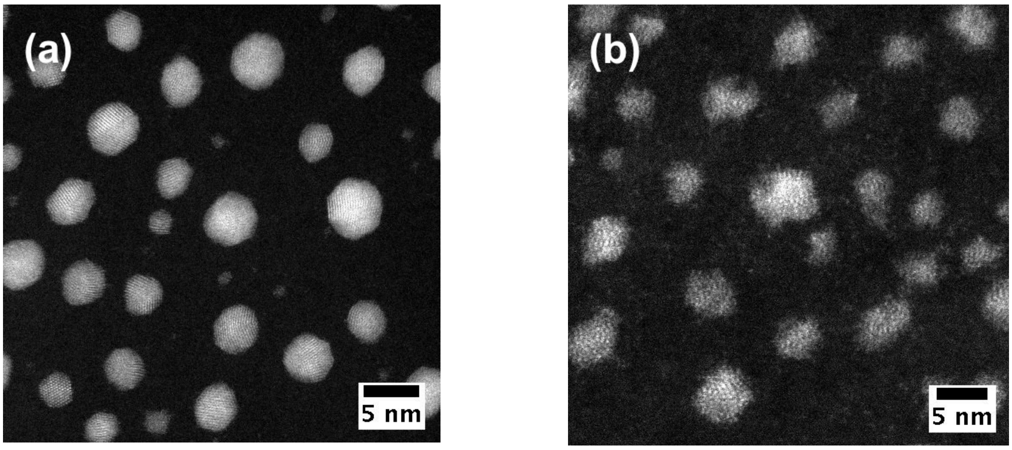

Figure 6.13. (a) HAADF-STEM image of evaporated Au nanoparticles deposited on amorphous carbon and annealed *in situ* for 120 minutes at 500 K; (b) HAADF-STEM image of evaporated Pd nanoparticles supported on amorphous carbon and annealed *in situ* for 120 minutes at 500 K.

Examining Figures 6.13, we can draw the conclusion that a diffused ordered metallic layer following annealing *cannot* be observed for the case of evaporated pure Au and Pd nanoparticles. We assume that the presence of the diffused Pd layer can only occur in the presence of Au. However, this will remain a topic of future investigation. We also assume that the presence of the PdO layer may be induced by diffusion upon annealing in the presence of a residual gas (O_2 or CO) in the deposition chamber [8]. The effect of gas adsorption on the surface of AuPd nanoparticles upon annealing is a subject of future investigation.

However, in the literature, the effect of gas adsorption has been previously studied theoretically. In a paper published by Metiu and Soto-Verdugo [33], the authors have shown that a Pd-enrichment of the surface of Au layer may also be induced by the presence of carbon monoxide (CO). The authors perform a DFT calculation on possible CO attachment sites for a two-layer Au slab in <111> and <100> orientations. The authors have chosen various binding sites for Pd, focusing on dopant placement on both top and sub-surface. As shown in Ref. [33], when the Au slab is in the <111> orientation, if the Pd dopant is placed on the surface, the adsorption energy of the CO molecule is -1.28 eV, whereas when the Pd dopant is place sub-surface, the adsorption energy of the CO molecule is -0.85 eV. A similar effect has been seen for the case of the Au slab in the <100> orientation. The authors in Ref. [33] concluded that the adsorption of the CO molecules is *independent* on the Pd-Pd distance, suggesting that the Pd atoms with CO on them are randomly distributed on the surface of the Au slab. The authors postulate that CO adsorption will induce the Pd enrichment of the surface. This may also consist a possible explanation on why the Pd migration has taken place on the surface of the evaporated and annealed AuPd nanoparticles.

Other literature reports have shown that, experimentally, for other bimetallic systems such as AuCo nanoparticles, the effect of annealing in the presence of oxygen atmosphere has also lead to the diffusion of the Co onto the surface of Au.

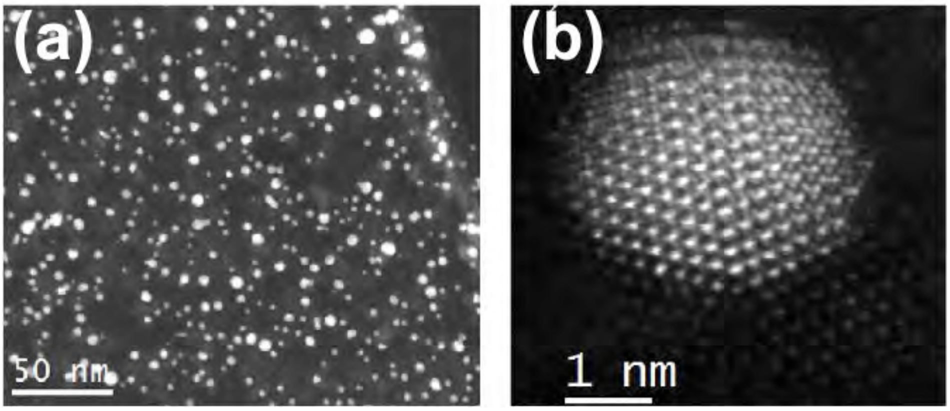

Figure 6.14. (a) HAADF-STEM image of chemically synthesized AuCo nanoparticles deposited on the surface of lacey carbon films. After annealing for 12 hours at 500 K in oxygen atmosphere, a diffused, thin CoO film can be observed. Adapted from Ref. [34].

This has been shown in the paper of Mayoral et al. [34] where, chemically-synthesized AuCo nanoparticles have been deposited on the surface of lacey carbon film (see Figure 6.14 (a) and (b)). The authors have concluded, based on thermodynamic considerations, that the diffusion of Co on the surface of nanoparticles followed by oxidation is a kinetically driven phenomenon, upon annealing at a temperature of 500 K.

6.4.4. Size dependency

Aside from structural and morphological changes, upon annealing at 500 K for 60, 120 and 180 minutes, we have also observed an increase in particle size. Table 6.3 is summarizing the evolution of the diameter distribution as a function of species, for mixed, layered and core-shell nanoparticles. By analyzing the data in Table 6.3, we observe that the diameters of the nanoparticle increase with the annealing time. Moreover, a dependency of the size on the nanoparticle’s morphology has also been observed for various annealing times.

The statistical analysis of the population morphology has shown that 100 % or the nanoparticles have mixed configurations for 60 minutes annealing at 500 K whereas for the case of 120 minutes annealing, a proportion of 29 % of the nanoparticles are mixed, 38 % of the nanoparticles are layered and 33 % of nanoparticles have core-shell morphologies. As discussed in section 6.2.4, the mixed nanoparticles are not present for 180 minutes annealing at 500 K and the population statistics is equally divided between layered and core-shell morphologies. Following the annealing process, the nanoparticle’s density has been established. Nanoparticles growth during annealing generally occurs either via cluster diffusion and coalescence or via atom exchange [35], a process quantifiable by the clusters density on the substrate.

Table 6.3. Diameters evolution for AuPd bimetallic nanoparticles annealed *in situ* at a temperature of 500 K for: (a) 60 minutes; (b)-(d) 120 minutes; (e)-(f) 180 minutes respectively, and the corresponding statistical population analysis.

Type	60 minutes	120 minutes	180 minutes
Mixed	2.53±0.28 nm 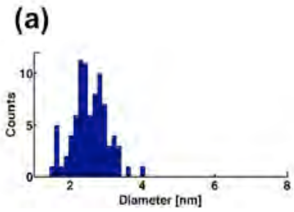	3.43±0.27 nm 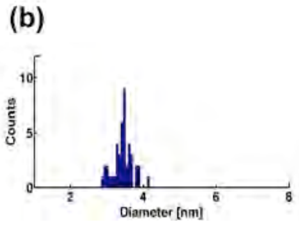	N/A
Layered	N/A	4.69±0.35 nm 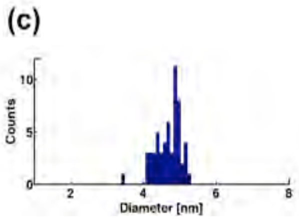	5.96±0.24 nm 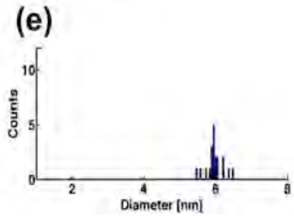
Core shell	N/A	5.56±0.31 nm 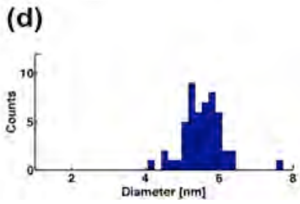	6.71±0.23 nm 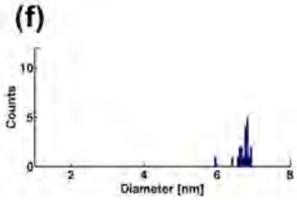
	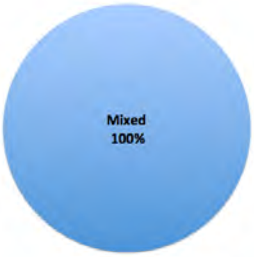	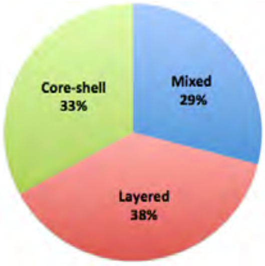	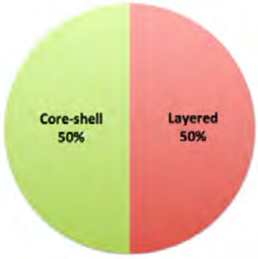

Table 6.4. Density of nanoparticles present on the substrate as a function of annealing temperature and time

Time of annealing	**As deposited**	**60 minutes**	**120 minutes**	**180 minutes**
Density (particles/µm^2)	5.18×10^4	3.95×10^4	1.69×10^4	1.39×10^4

Examining Table 6.4, the density of nanoparticles on the as-deposited sample is 5.18×10^4 particles/µm^2, a value that decreases progressively to a value of 1.39×10^4 particles/µm^2 for the case of annealing for 180 minutes at 500 K. Correlating the value of the density with the evolution of the nanoparticles diameters as a function of annealing time (see Table 6.4), we can conclude that the larger nanoparticles grow via coalescence of smaller nanoparticles [35].

6.8. Conclusions

HAADF-STEM analysis has been employed for the characterization of bimetallic AuPd nanoparticles produced by physical vapour deposition (PVD). The nanoparticles have been deposited on the surface of amorphous carbon and annealed *in situ* at a temperature of 500 K for periods of 60, 120 and 180 minutes. Annealing the sample at 60 minutes has revealed the existence of mixed nanoparticles. Further annealing for 120 minutes at 500 K reveals the existence of three types of nanoparticle morphologies, namely mixed AuPd nanoparticles, layered and core-shell. A further step of annealing, for 180 minutes at 500 K has revealed only layered and core-shell morphologies.

The interpretation has been attributed to the mixed nanoparticles being trapped into a thermodynamic metastable state, for which further annealing has led to the appearance of layered and core-shell morphologies. More interestingly, the nanoparticles fft patterns, following annealing, have reflections attributable to the presence of superlattices, evidence of $L1_2$ ordered crystallographic phases. The strong contrast difference in the HAADF-STEM image has been attributed to the presence of Au and Pd. The elemental mapping based on Energy Dipsersive X-ray (EDX) spectroscopy, has confirmed the presence of Au, Pd and O respectively. This work aimed to offer an insight on the kinetically-driven effects in evaporated AuPd nanoparticles upon annealing at temperature of 500 K for various durations of time.

Bibliography

---

[1] Zhang, H., Watanabe, T., Okumura, T., Haruta, M., Toshima, N., *Nature Materials*, 11, 49, **2012**.

[2] Lee, M. H., Park, Y. S., Park, T. K., Jung, H. U., Chun, K., Woong, D. C., Kim, H. S., *Res. Chem. Intermed*., 34, 787, **2008**.

[3] Kan, K., Cai, W., Li, C., Zhang, L., Hofmeister, H., *J. Phys. D.: Appl. Phys*., 36, 1609, **2003**.

[4] Tran, N. T., Powell, D. R., Dahl, L. F., *Dalton Trans.*, 2, 217, **2004**.

[5] Tiruvalam, R. C., Pritchard, J. C., Dimitratos, N., Lopez-Sanchez, J. A., Edwards, J. K., Carley, A. F., Hutchins, G. J., Kiely, C. J., *Faraday Discuss*., 63, 152, **2011**.

[6] Akita, T., Hiroki, T., Tanaka, S., Kojima, T., Kohayama, M., Iwase, A., Hori, F., *Catal. Today*, 131, 90, **2003**.

[7] Ferrer, D., Torres-Castro, A., Gao, X., Sepulveda-Guzman, S., Ortiz-Mendez, U., Jose-Yacaman, M., *Nano Lett*., 6, 1701, **2007**.

[8] Paz-Borbon, L. O., *Computational Studies of Transition Metal Nanoalloys*, Springer Theses, Berlin, **2011**.

[9] De Graef, M., McHenry, M. E., *Structure of materials*, Cambridge University Press, Cambridge, **2007**.

[10] Okamoto, H., *Phase Diagrams for Binary Alloys*, ASM International, 2nd edition, Novelty, **1985**.

[11] Jana, D., Dandapat, A., De, G., *J. Phys. Chem. C*., 113, 9101, **2009**.

[12] Nagasawa, A. Matsuo, Y., Kakinoki, J., *J. Phys. Soc. Jpn*., 20, 1881, **1965.**

[13] Matsuo, Y., Nagasawa, A., Kakinoki, J., *J. Phys. Soc. Jpn*, 21, 2633, **1966**.

[14] Nagasawa, A., *J. Phys. Soc. Jpn*, 19, 2344, **1964.**

[15] Liu, H. B., Pal, U., Medina, A., Maldonado, C., Ascensio, J. A., *Phys. Rev. B*, 71, 075403, **2005**.

[16] Boscoboinik, J. A., Plaisance, C., Neurock, M., Tysoe, W. T., *Phys. Rev. B.*, 77, 045422, **2008**.

[17] Yuan, D. W., Gong, X. G., Wu, R., Q., *Phys. Rev. B*, 78, 035441, **2008**.

[18] Ismail, R., Johnston, R. L., *Phys. Chem. Chem. Phys.*, 12, 8607, **2010**.

[19] Johnston, R. L., Wilcoxon, J. (eds.), *Metal nanoparticles and nanoalloys*, Elsevier, Oxford, **2012**.

[20] Bruma A., Ismail, R., Paz-Borbon, L. O., Arslan, H., Barcaro, G., Fortunelli, A., Li, Z. Y., Johnston, R. L., *Nanoscale*, 5, 646, **2013**.

[21] Liu, H. B., Pal, U., Medina, A., Maldonado, C., Ascensio, J. A., *Phys. Rev. B.:Condens. Matter. Mater. Phys.*, 71, 075403, **2005**.

[22] Kittlel, C., *Introduction to Solid State Physics*, John Wiley & Sons, 8th edition **,** Hoboken, **2005**.

[23] Ding, Y., Fan, F., Tian, Z., Wang, Z. L., *J. Am. Chem. Soc.*, 132, 12480, **2010**.

[24] Perez-Tijerina, E., Mejia-Rosales, S., inada, H., Jose-Yacaman, M., *J. Phys. Chem. C.*, 114, 6999, **2010**.

[25] Mejia-Rosales, S., Fernandez-Navarro, C., Perez-Tijerina, E., Montejano-Carrizales, J. M., Jose-Yacaman, M., *J. Phys. Chem. B*, 110, 12884, **2006**.

[26] Perez-Tijerina, E., Gracia Pinilla, M., Mejia-Rosales, S., Ortiz-Mendez, U., Torres, A., Jose-Yacaman, M., *Faraday Discuss.*, 138, 353, **2008**.

[27] Mayoral, A., Mejia-Rosales, S., Mariscal, M. M., Perez-Tijerina, E., Jose-Yacaman, M., *Nanoscale*, 2, 2647, **2010**.

---

[28] Deepak, F. L., Casilas-Garcia, G., Esparza, R., Barron, H., Jose-Yacaman, M., *J. Crystal Growth*, 325, 60, **2011**.

[29] Jacobs, J. W., Schryvers, D. S., *J. Catal.*, 103, 436, **1987**.

[30] Lamber, R., Jaeger, N., Schulz-Ekloff, G., *Surf. Sci.*, 15, 227, **1990**.

[31] Rice, M. J., Chakraborty, A. K., Bell, A. T., *J. Phys. Chem. B*, 104, 278, **2000**.

[32] Buehrer, T. F., Roseveare, W. E., *J. Am. Chem. Soc*, 49, 1989, **1927**.

[33] Metiu, H., Soto-Verdugo, V., *Surf. Sci.*, 601, 5332, **2007**.

[34] Mayoral, A., Deepak, F. L., Esparza, R., Casillas, G., Magen, C., Perez-Tijerina, E., Jose-Yacaman, M., *Micron*, 43, 557, **2012**.

[35] Alloyeau, D., Prevot, G., Le Bouar, Y., Oikawa, T., Langlois, C., Loiseau, A., Riccoleau, C., *Phys. Rev. Lett.*, 105, 255901, **2010**.

Conclusions and future work

In this thesis we have presented a combined experimental and theoretical approach for the study of AuPd nanoparticles. From a theoretical point of view, two systems have been studied: the 98-atoms AuPd and $Au_{24}Pd_1$ nanoparticles. From an experimental point of view, two systems have been examined, namely $Au_{24}Pd_1$ nanoclusters supported on Multiwall Carbon Nanotubes (MWCNTs) and evaporated AuPd nanoparticles supported on amorphous carbon.

For the *first system*, the 98-atom AuPd nanoparticles, we have shown that a combined approach based on the use of empirical potentials, the Gupta potential, with DFT calculations, and employing a genetic algorithm (GA) and Basin Hopping Monte Carlo (BHMC) techniques is a powerful tool for the identification of low-energy structural motifs and segregation patterns in bimetallic AuPd clusters. At the empirical level, we have compared three sets of parameters for the Gupta potential, DFT-fit, Exp-fit and Average. It has been found that, the DFT-fit and the Exp-fit potential favour a high degree of mixing between Au and Pd, in comparison to the Average potential who favours $Pd_{core}Au_{shell}$ configurations. At empirical level, the LT has not been found to be a typical structure for the 98-atom AuPd nanoclusters. To generate this structure, a shell optimization program has been used. After the optimization of the chemical ordering, in comparison to other structural motifs, such as FCC-HCP, or Marks Decahedron, the LT structure has been found to be the most stable structure for the Average potential, at the empirical level. However, the energetics has been changed after we have performed DFT relaxation calculations, other structural motifs such as FCC-HCP and Marks Decahedron being the most stable. This observation is consistent with our experimental observations of evaporated AuPd nanoparticles, where morphologies such as FCC are more often encountered, whereas LT structures have not been yet identified for AuPd nanoparticles. Although the DFT studies are limited to a small number of atoms due to computational limitations, they are an important step in understanding the segregation patterns for larger nanoparticles.

For the study of the *second system*, the $Au_{24}Pd_1$ nanoparticles, combined state-of-the-art experimental and theoretical techniques are employed. From an *experimental point of view*, the High Angle Annular Dark Field Scanning Transmission Electron Microscopy (HAADF-STEM) has been employed in order to determine the morphology of the $Au_{24}Pd_1$ nanoparticles supported on Multiwall Carbon Nanotubes (MWCNTs), as well as in order to determine the total number of atoms in the clusters. For the latter purpose, single Au atoms, found in the immediate vicinity of evaporated Au nanoparticles have been used as mass standards. By comparing the integrated HAADF-STEM intensity of $Au_{24}Pd_1$ nanoparticles with the integrated intensities of single Au atoms, a number of 25 ± 2 atoms have been identified. Moreover, the effect of electron beam over the morphology of clusters has also been identified. HAADF-STEM technique allows a series of snapshots to be recorded, offering the unique possibility of observing the transformation between energetically-excited cluster configurations. In order to observe this, a high and low-electron beam current analysis has been employed. A prominent cluster morphology change, as well as atom detachment has been identified for high-electron beam imaging, whereas this tendency has been suppressed for the case of low-electron beam current.

From a *theoretical point of view*, the low-energy structures of free (unsupported) $Au_{24}Pd_1$ have been identified by performing a hybrid BHMC-DFT algorithm. Low-energy isomers have been identified, with a prominent tendency to form Au cages with a single core atom (the latter being Pd rather than Au). It has been observed that pyramidal motifs have been preferred as the cage skeleton, but more complex structures such as double icosahedron have been found to be very close in energy, pointing to a strong fluxional for this system and a tendency for oblate shapes, as identified throughout our experiment. A Löwdin population analysis has been performed in order to identify the charge transfer between the dopant and the cage. A substantial charge transfer has been identified from Pd to the surrounding Au cage, suggesting that the Pd dopant acts as an electron promoter to the surrounding Au atoms, which may explain the experimentally observed enhancement of the catalytic activity of single Pd-doped Au_{25} clusters.

The *third system* has been the experimental investigation of evaporated AuPd nanoparticles supported on amorphous carbon and their structure and morphology change as a function of annealing temperature and time. A fixed temperature (500 K) and a varying duration of time for annealing (60, 120 and 180 minutes respectively) have been chosen for the study of this system. HAADF-STEM analysis has been employed for the experimental characterization of this system. The purpose of this analysis has been to prove that bimetallic nanoparticles can be obtained by physical vapour deposition and, moreover, various morphologies, ranging from mixed to layered and core-shell can be obtained. This analysis is important as nanoparticles morphological transformation upon annealing is of high interest in the domain of nanocatalysis, where multiple reactions can take place on the surface of the same catalyst as a function of the particle morphology.

The analysis of the diffraction patterns has indicated that, upon annealing, $L1_2$ ordered crystallographic phases can be obtained. The HAADF-STEM and electron diffraction analysis have been completed by performing EDX elemental mapping, confirming the existence of Au and Pd.

The calculations of segregation effects and the structural and energetic analysis of bimetallic AuPd nanoparticles presented in this thesis could hopefully be useful in future studies of chemical reactions that take place on the surface of these nanosystems. From a theoretical point of view, studies of chemisorption and reactions of small molecules on supported nanoparticles will be undertaken. In these studies, the interaction between the molecule and the nanoparticle as well as nanoparticle-substrate interaction should be considered at the same time.

For the $Au_{24}Pd_1$ clusters, further investigations regarding the effect of charge transfer between the Pd dopant and the surrounding Au atoms should be better understood, in order to shed light on the nanoparticles activity in oxidation catalysis. The studies of other molecules attachment (e.g. CO) could also be a further step.

Experimentally, for the case of evaporated AuPd systems, further analysis should be made regarding placing the nanosystem on more reactive oxidic substrates (such as MgO or Al_2O_3) and studying the effect of annealing temperature and time on the overall nanoparticle morphology. Such substrates are of importance in catalysis reactions, as significant charge transfer from the oxidic surface to the nanoparticle has also been found to take place.

Appendix 1

Three-dimensional structure of Au nanoparticles supported on amorphous silica and carbon substrates

A.1. Introduction

Gold nanoparticles supported on insulating substrates such as SiO_2 [1] have attracted a lot of research interest in the past few years, due to their important applications in domains such as nanoelectronics [2] or catalysis [3]. Transmission Electron Microscopy (TEM) has been employied to study the influence of the size and structure of Au nanoparticles deposited on or embedded into SiO_2 [4, 5]. However, the information of the growth mode of Au nanoparticles on this substrate has been lacking. In this Annex we address this issue by using the information obtained with the Scanning Transmission Electron Microscope (STEM). It has been demonstrated that the use of quantitative analysis of High Angle Annular Dark Field (HAADF) STEM, coupled with simple geometrical models, can be a powerful analysis technique regarding the study of the shape of carbon supported Au size selected clusters and evaporated Au nanoclusters respectively [6]. The growth mode of Au nanoparticles deposited via physical vapour deposition (PVD) has been well documented in the literature [6, 7]. It is generally accepted that the bonding between Au nanoparticles and the carbon substrate is weak [8] and the shape of Au nanoparticles can be considered as hemispherical. However, this is not the case on silica substrates, as the shape and the thermal stability of Au nanoparticles tends to vary and are highly dependent on how the substrates have been prepared [9]. This present study presents a comparative analysis of the shape of Au nanoparticles deposited via PVD onto amorphous carbon and silica substrates, as well as the effect of annealing temperature on the shape of Au nanoparticles for both cases.

The results presented in this chapter have been published: *Bruma, A., Li, Z. Y., J. Phys. Conf. Ser., 371, 012067, 2012.*

A. 2. Experimental details

Au nanoparticles have been deposited on the surface of amorphous carbon and silica thin film covered commercial TEM grids (Agar Inc.), at a base pressure of 10^{-7} mbar. The substrates have been maintained at a temperature of 300 K and 473 K respectively during the deposition of Au nanoparticles. A JEOL JEM 2100F STEM has been employed for the characterization of evaporated Au nanoparticles, with an inner collection angle of 63 mrad. Throughout the experiment, the emission current has been noted stable. For the quantitative statistical analysis of Au nanoparticles, a number of ~ 150 nanoparticles have been considered for each case.

A. 3. Results and discussions

Figure 1 shows four representative HAADF-STEM images of Au nanoparticles deposited on silica (Figure 1 (a)-(b)) and carbon (Figure 1 (c)-(d)) annealed at 300 K and 473 K respectively. As observed here, the nanoparticles form well-separated islands in both cases. Most Au nanoparticles are well separated, excepting few closely-spaced nanoparticles that tend to be touching. The size distribution of nanoparticles is shown in Figure 1 (e)-(h).

As observed from the nanoparticles size distribution, as the temperature of substrate increases from 300-473 K, the mean value of nanoparticles increases from 3.45 nm to 4.39 nm with a standard deviation of 0.76 nm for Au nanoparticles supported on SiO_2 and from 2.22 nm to 3.18 nm with a standard deviation of 0.5 nm for the case of Au nanoparticles supported on amorphous carbon. As observed here, the higher the temperature the larger the size of nanoparticles, an indication of the fact that the nanoparticles are formed as a result of kinetic limited aggregation. The larger nanoparticles formed on SiO_2 substrate may be associated with a larger diffusion length of Au atoms on SiO_2 than for the case of Au atoms on amorphous carbon. It is also interesting to observe that the standard deviation related to the diameter distribution is independent on the substrate temperature. However, the larger standard deviation of nanoparticles on SiO_2 in comparison to carbon may be an indication of a more random distribution of defects on SiO_2, which act as nucleation centres for Au cluster growth.

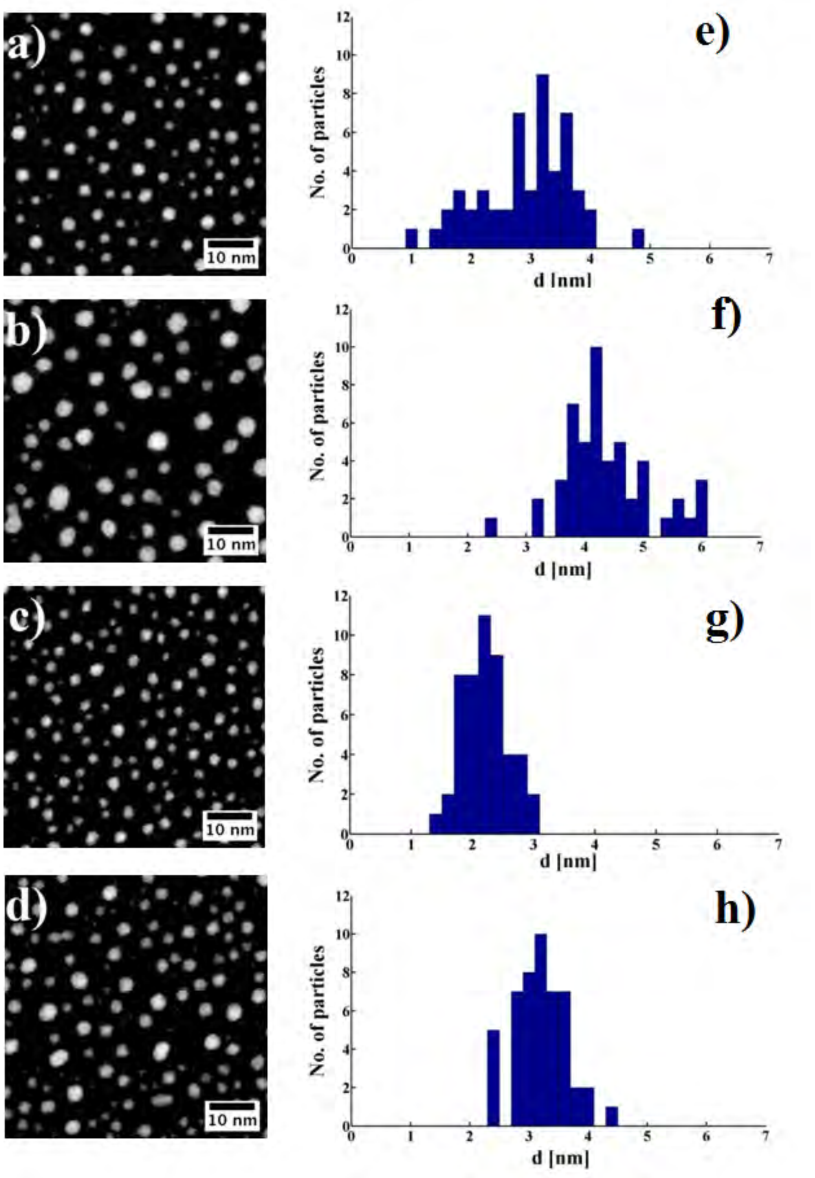

Figure 1. Representative HAADF-STEM images and corresponding size distribution of evaporated Au nanoparticles on SiO_2 at 300 K (a) and 473 K (b) respectively; deposition on a-C at 300 K (c) and 473 K (d) respectively. Histograms of the corresponding diameter distribution are shown in (e)-(h), placed directly besides the representative figures.

The next step has been to perform quantitative analysis for the Au nanoparticles, based on information regarding the integrated HAADF-STEM intensities. HAADF-STEM is an incoherent imaging technique, and, as a consequence, the integrated intensities are proportional to the nanoparticle volume [6,10]. Here, the integrated intensities are determined for each nanoparticle after local background subtraction and the diameters are taken as the average of the long and short axes of the projection for each nanoparticle.

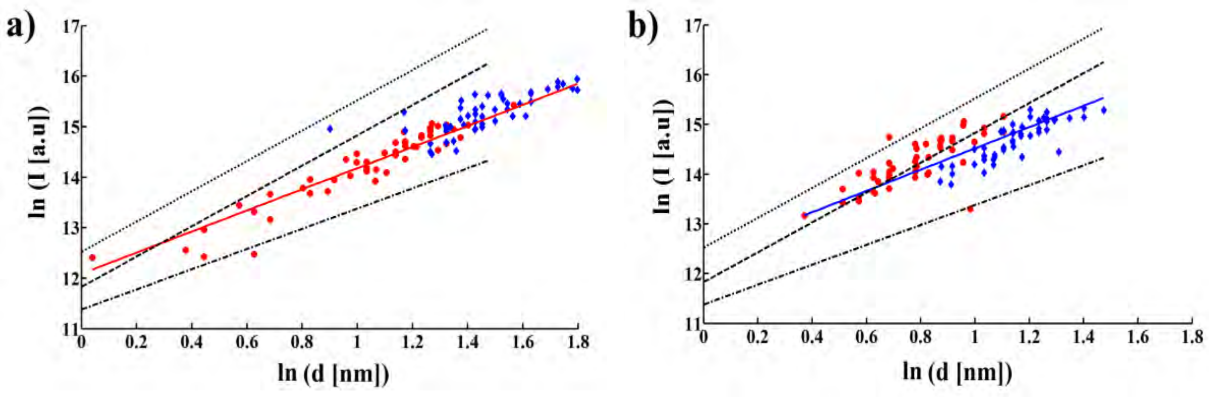

Figure 2. Double logarithmic plot of the evolution of Integrated Intensity as a function of nanoparticles diameters. (a) Deposition on SiO_2 at 300K (•) and 473K (♦). (b) Deposition on a-C at 300K (•) and 473K (♦). The solid lines are the best fit for the data for SiO_2 (R=0.93) and C (R=0.87). The 3D spherical and hemispherical model are shown as dashed lines together with the 2D model (dashed-dot line).

In Figure 2 (a) and (b), we take into consideration simple geometrical models, by assuming that the particles can be modeled by a 3D-sphere or hemisphere, or a 2D circular raftlike disk. Therefore, the HAADF-STEM intensity would be proportional to either d^3 or d^2, where d is the diameter of the nanoparticle.

In Figure 2, double logarithmic plots are shown for SiO_2 (a) and amorphous carbon (b), together with a 2D disk and spherical and hemispherical models respectively. The solid lines show the least square fitting of the data, with a slope of 2.09 in the case of SiO_2 and 2.14 in the case of carbon. Both are clearly shown to deviate from the 3D spherical model, which has been proposed for the colloidal nanoparticles as well as for size selected Au clusters soft landed on the carbon substrate [6]. Both plots suggest that the nanoparticle shapes are more close to hemispherical and other 2D models than to the spherical growth model, an indication that Au nanoparticles are wetting on both substrates. An interesting observation in Figure 2 is that the scaling exponents are unchanged, i.e the growth mode is the same irrespective of the substrate temperature, 300 K or 473 K respectively.

This conclusion again confirms the analysis shown in Figure 1, namely that the growth of nanoparticles is governed by kinetic processes within the proposed temperature range. The almost identical scaling exponents of Au on amorphous SiO_2 and carbon suggests a similar size dependent 3D shape of Au nanoparticles irrespective of the substrate. This is an indication of a similar binding energy for Au/SiO_2 and Au/carbon. It is interesting to compare our results to those of Veith et al. [11], where the enhanced thermal stability of Au nanoparticles of sizes of ~ 2.5 nm deposited onto SiO_2 has been demonstrated up to a temperature of 773 K in an oxygen atmosphere. Here, the authors have attributed the enhanced stability of Au nanoparticles to the substrate defects where protons or surface hydroxyl groups have been removed during the Au deposition using a magnetron sputtering technique. However, the shape of the Au nanoparticles and their dependency on the nature of the support and its temperature is a topic of further investigation.

A.4. Conclusions

In this study, we have shown that a quantitative HAADF-STEM analysis of Au nanoparticles shapes is important for a better understanding of the role of the support temperature and nature on the overall geometry of nanoparticles. Here, we have established a correlation between the integrated HAADF-STEM intensity of each Au nanoparticle and the nanoparticle diameter. A quantitative analysis of the scaling exponent, together with the use of simple geometrical models allows a characterization of the three-dimensional morphology of the nanoparticles. We have established that the growth mode via physical vapour deposition is intermediate between 2D and 3D. By analyzing the dependency of the integrated HAADF-STEM intensity to the diameter of the nanoparticle, we have shown that the scaling exponents are not influenced by the temperature of the substrates. This method could be of particular importance in the domain of industrial catalysis, where the supported nanoparticles have complex shapes with large surface areas.

Bibliography

---

[1] Zhu, K., Hu, J., Richards, R., *Catal. Lett.*, 100, 195, 2005.

[2] Lee, S. J., *Gold Bull.*, 43, 189, 2010

[3] Zhen, X., Veith, G. M., Redekop, E., Lo, C. S., Yablonsky, G. S., Gleaves, J. T., *Ind. Eng. Chem. Res.*, 49, 10428, 2010.

[4] Ruffino, F., Bongiorno, C. Giannazzo, F., Roccaforte, F., Raineri, V., Grimaldi, M. G., *Nanosc. Res. Lett.*, 3, 454, 2008.

[5] Ruffino, F., Grimaldi, M. G., Giannazzo, F., Roccaforte, F., Raineri, V., *Nanosc. Res. Lett.*, 3, 454, 2008.

[6] Young, N. P., Li, Z. Y., Chen, Y., Palomba, S., Di Vece, M., Palmer, R. E., *Phys. Rev. Lett.*, 241603, 2008.

[7] Koga, K., Sugawara, K., *Surf. Sci.*, 529, 23, 2003.

[8] Mason, G. M., *Phys. Rev. B.*, 27, 748, 1983.

[9] Martra, L., Prati, L., Manfredotti, C., Biella, S., Rossi, M., Coluccia, S., *J. Phys. Chem. B.*, 107, 5453, 2003.

[10] Treacy, M. M. J., Rice, S. B., *J. Microsc.*, 156, 211, 1989.

[11] Veith, G. M., Lupini, A. R., Rashkeev, S., Pennycook, S. J., Mullins, D., Schwartz, V., Bridges, C. A., Dudney, N., *J. Catal.*, 262, 92, 2009.

Published papers

1. Bruma, A., Ismail, R., Paz-Borbon, L. O., Arslan, H., Barcaro, G., Fortunelli, A., Li, Z. Y., Johnston, R. L., **DFT studies of the structure and energetics of the 98-atom AuPd clusters**, *Nanoscale*, 5, 646, **2013**.

2. Bruma, A., Li, Z. Y., **Three dimensional structure of Au nanoparticles supported on amorphous carbon and silica substrates**, *J. Phys. Conf. Ser.*, 371, 012067, **2012**.

3. Bruma, A., Negreiros, F., Xie, X., Tsukuda, T., Johnston, R. L., Fortunelli, A., Li, Z. Y., **Direct atomic imaging and density functional theory study of $Au_{24}Pd_1$ cluster catalyst**, *Nanoscale,* 10.1039/C3NR01852K, 2013.